UNIVERSITÉ DU QUÉBEC À TROIS-RIVIÈRES

SYSTÈMES A PILES A COMBUSTIBLE A EMPILEMENTS MULTIPLES : DE LA GESTION DE L'ÉNERGIE DE RÉFÉRENCE AU DIMENSIONNEMENT ET A LA GESTION DE L'ÉNERGIE INTÉGRÉS POUR LES VÉHICULES LOURDS ET LES AÉRONEFS

THÈSE PRÉSENTÉE
COMME EXIGENCE PARTIELLE DU
DOCTORAT EN GÉNIE ÉLECTRIQUE

PAR
HAMID BAKHSHI YAMCHI

MARS 2026

UNIVERSITÉ DU QUÉBEC À TROIS-RIVIÈRES

MULTI-STACK FUEL CELL SYSTEMS: FROM BENCHMARK ENERGY MANAGEMENT TO INTEGRATED SIZING AND ENERGY MANAGEMENT IN HEAVY-DUTY VEHICLES AND AIRCRAFTS

A THESIS PRESENTED
IN PARTIAL FULFILLMENT OF
THE REQUIREMENTS FOR THE DEGREE
DOCTOR OF PHILOSOPHY IN ELECTRICAL ENGINEERING

BY
HAMID BAKHSHI YAMCHI

MARCH 2026

UNIVERSITÉ DU QUÉBEC À TROIS-RIVIÈRES

DOCTORAT EN GÉNIE ÉLECTRIQUE (PH.D.)

Direction de recherche:

Mohsen Kandidayeni Université du Québec à Trois-Rivières	directeur de recherche
Sousso Kelouwani Université du Québec à Trois-Rivières	codirecteur de recherche

Jury d'évaluation:

Mohsen Kandidayeni Université du Québec à Trois-Rivières	directeur de recherche
Sousso Kelouwani Université du Québec à Trois-Rivières	codirecteur de recherche
Mamadou Lamine Doumbia Université du Québec à Trois-Rivières	président du jury
Samir Jemei Université Marie & Louis Pasteur	évaluateur externe
Cao Minh Ta Université Sherbrooke	évaluateur externe

Thèse soutenue le 11 Mai 2026

UNIVERSITÉ DU QUÉBEC À TROIS-RIVIÈRES

DOCTOR OF PHILOSOPHY IN ELECTRICAL ENGINEERING (PH.D.)

Research Supervision:

Mohsen Kandidayeni — research director
Université du Québec à Trois-Rivières

Sousso Kelouwani — research co-director
Université du Québec à Trois-Rivières

Evaluation jury:

Mohsen Kandidayeni — research director
Université du Québec à Trois-Rivières

Sousso Kelouwani — research co-director
Université du Québec à Trois-Rivières

Mamadou Lamine Doumbia — jury president
Université du Québec à Trois-Rivières

Samir Jemei — external evaluator
Université Marie & Louis Pasteur

Cao Minh Ta — external evaluator
Université Sherbrooke

Thesis defended on 11 May 2026

Abstract

Multi-stack fuel cell systems (MFCSs) have emerged to meet high power demands, enhance reliability through redundancy, and improve packaging flexibility beyond what single-stack systems can provide in transportation powertrains, but their added degrees of freedom make coordinated control and hardware selection nontrivial. In such systems, an energy management strategy (EMS) is essential to allocate power among FC stacks and the battery to track load while reducing hydrogen use, limiting component aging, and safeguarding serviceability, whereas integrated sizing–EMS co-design is necessary because component sizes constrain feasible operating regions and durability–cost trade-offs, especially for heavy-duty vehicles and aircrafts where mass, cost, and lifetime are tightly coupled. This thesis advances design-to-operation methods for MFCSs by developing a benchmark offline EMS and two integrated sizing–EMS frameworks tailored to ground and air domains, with explicit attention to cost, weight, degradation, and uncertainty.

First, an offline EMS based on a constrained exploration method allocates power across FC stacks and the battery in a fuel cell hybrid electric vehicle, using three types of filters (to reduce the computational time while scaling to higher number of FC stacks) within a health-conscious multi-objective cost to cut hydrogen consumption and stack degradation. Across an aircraft (NASA X-57 Maxwell with two 50 kW stacks), a tramway (two 125 kW stacks), and a truck (four 75 kW stacks), the proposed method matches or surpasses level-set dynamic programming and sequential quadratic programming in accuracy and computation burden, and it remains tractable where dynamic programming fails, establishing a scalable EMS benchmark for multi-stack platforms.

Second, a degradation-aware integrated sizing–EMS jointly determines FC stack sizes and battery configuration without fixing total FC capacity, embedding the degradation of FC stacks and the battery in both sizing and EMS stages to improve longevity and total cost over mission profile. A hybrid genetic algorithm–model predictive control (GA–MPC) loop explores discrete hardware designs and enforces degradation-aware power allocation, yielding significant total cost reductions in a long-haul truck and experimental validation on a multi-stack testbench.

Third, for aircraft, a multi-objective integrated sizing–EMS targets simultaneous minimization of powertrain total cost and weight under requested-power uncertainty while considering degradation of FC stacks and battery at both sizing and EMS levels. The framework co-optimizes the sizes of multiple FC systems and the battery, minimizing investment cost and weight in the sizing layer via non-dominated sorting genetic algorithm II (NSGA-II), while the EMS layer based on MPC minimizes operational cost from hydrogen use and degradation under the uncertainty of load.

Collectively, these contributions provide a scalable offline EMS benchmark and robust integrated sizing–EMS framework that reduce cost, weight, and degradation in MFCSs including heavy-duty vehicles and aircraft applications.

Résumé

Les systèmes à piles à combustible multi-empilements (SPACMs) ont émergé pour répondre à des demandes de puissance élevées, améliorer la fiabilité grâce à la redondance et accroître la flexibilité d'intégration au-delà de ce que les systèmes à pile unique peuvent offrir dans les groupes motopropulseurs de transport, mais leurs degrés de liberté supplémentaires rendent le contrôle coordonné et la sélection du matériel non triviaux. Dans de tels systèmes, une stratégie de gestion de l'énergie (SGE) est essentielle pour répartir la puissance entre les piles à combustible et la batterie afin de suivre la charge tout en réduisant la consommation d'hydrogène, en limitant le vieillissement des composants et en garantissant la maintenabilité, tandis qu'une co-conception intégrée dimensionnement–SGE est nécessaire car la taille des composants contraint les régions de fonctionnement réalisables et les compromis entre durabilité et coût, en particulier pour les véhicules lourds et l'aéronef où la masse, le coût et la durée de vie sont étroitement liés. Cette thèse fait progresser les méthodes de conception à exploitation pour les SPACM en développant une stratégie SGE de référence hors ligne et deux cadres intégrés dimensionnement–SGE adaptés aux domaines terrestre et aérien, avec une attention explicite portée au coût, au poids, à la dégradation et à l'incertitude.

Premièrement, une SGE hors ligne basée sur une méthode d'exploration contrainte répartit la puissance entre les piles à combustible et la batterie dans un véhicule électrique hybride à pile à combustible, en utilisant trois types de filtres (pour réduire le temps de calcul tout en s'adaptant à un plus grand nombre de piles à combustible) au sein d'un coût multiobjectif tenant compte de l'état de santé pour réduire la consommation d'hydrogène et la dégradation des piles. Pour un avion (NASA X-57 Maxwell avec deux piles de 50 kW), un tramway (deux piles de 125 kW) et un camion (quatre piles de 75 kW), la méthode proposée égale ou dépasse la programmation dynamique par ensemble de niveaux et la programmation quadratique séquentielle en précision et en charge de calcul, et reste exploitable là où la programmation dynamique échoue, établissant une référence SGE évolutive pour les plateformes multi-empilements.

Deuxièmement, une co-conception intégrée dimensionnement–SGE tenant compte de la dégradation détermine conjointement la taille des piles à combustible et la configuration de la batterie sans fixer la capacité totale de la pile, en intégrant la dégradation des piles à combustible et de la batterie à la fois dans les étapes de dimensionnement et d'SGE afin d'améliorer la longévité et le coût total sur le profil de mission. Une boucle hybride algorithme génétique–commande prédictive (GA–MPC) explore les conceptions matérielles discrètes et impose une répartition de puissance tenant compte de la dégradation, entraînant des réductions significatives du coût total dans un camion longue distance et une validation expérimentale sur un banc d'essai multi-empilements.

Troisièmement, pour l'aéronef, une co-conception intégrée dimensionnement–SGE multiobjectif vise la minimisation simultanée du coût total et du poids du groupe motopropulseur sous incertitude de la puissance demandée, tout en tenant compte de la dégradation des piles à combustible et de la batterie à la fois aux niveaux du dimensionnement et de l'SGE. Le cadre co-optimise les tailles de plusieurs systèmes de piles à combustible et de la batterie, en minimisant le coût d'investissement et le poids dans la couche de dimensionnement via l'algorithme génétique à tri non dominé II (NSGA-II), tandis que la couche SGE basée sur la commande prédictive (MPC) minimise le coût opérationnel dû à la consommation d'hydrogène et à la dégradation sous incertitude de la charge.

Collectivement, ces contributions fournissent une référence SGE hors ligne évolutive et un cadre intégré dimensionnement–SGE robuste qui réduisent le coût, le poids et la dégradation dans les SPACM, y compris pour les applications dans les véhicules lourds et l'aéronef.

Acknowledgements

I am thankful to Université du Québec à Trois-Rivières and the Institut de recherche sur l'hydrogène (IRH), a premier center for hydrogen and sustainable energy research, for enabling my Ph.D. studies and professional growth.

My foremost thanks go to my supervisor, Prof. Mohsen Kandidayeni, whose inspiring leadership, expert oversight, and thoughtful critiques were pivotal to my progress. I also greatly appreciate my co-supervisor, Prof. Sousso Kelouwani, for his perceptive input, strategic advice, and access to laboratory resources that strengthened my publications and dissertation. Special recognition to Prof. Loïc Boulon for his ongoing guidance and valuable consultations, which laid the groundwork for my research from the outset. Working with such distinguished scholars has been a true privilege.

I am grateful to my lab teammates for their dedicated collaboration, shared insights, and mutual encouragement that made this challenging journey more rewarding.

Above all, my heartfelt thanks to my beloved family for their unwavering love, understanding, patience, and constant motivation that sustained me through every trial and led to this achievement.

Table of Contents

List of Tables

List of Figures

List of Acronyms

BEV	Battery Electric Vehicle
CO	Carbon Monoxide
CO_2	Carbon Dioxide
CapEx	Capital Expenditures
CEM	Constrained Exploration Method
CSHVR	City Suburban Heavy Vehicle Cycle & Route
DP	Dynamic Programming
ECMS	Equivalent Consumption Minimization Strategy
EMS	Energy Management Strategy
EOL	End-of-Life
ESS	Energy Storage System
FC	Fuel Cell
FC-HEV	Fuel Cell Hybrid Electric Vehicle
FCS	Fuel Cell System
GA–MPC	Genetic Algorithm–Model Predictive Control
HDV	Heavy-Duty Vehicle
HEV	Hybrid Electric Vehicle
H_2O	Water Vapor
HESS	Hybrid Energy Storage System
HF	Hybridization Factor
IAE	International Energy Agency
ISEMS	Integrated Sizing And Energy Management Strategy
LDV	Light-Duty Vehicle
LiB	Lithium-ion Battery
LiC	Lithium-ion Capacitor
MEA	Membrane Electrode Assembly

MFCS	Multi-Stack Fuel Cell Systems
MISEMS	Multi-Objective Integrated Sizing And Energy Management Strategy
MINLP	Mixed-Integer Nonlinear Programming
MPC	Model Predictive Control
NSGA-II	Non-Dominated Sorting Genetic Algorithm II
OpEx	Operational Expenditures
PCA	Principal Component Analysis
PEMFC	Proton Exchange Membrane Fuel Cell
SAF	Sustainable Aviation Fuel
SC	Supercapacitor
SO_4^{2-}	Sulfate ion
SOH	State of Health
SOC	State of Charge
SQP	Sequential Quadratic Programming
VOC	Volatile Organic Compound
WLTC	Worldwide Harmonized Light-Duty Vehicles Test Cycle

Chapter 1 - Introduction

1.1 Motivation

1.1.1 Hydrogen Role in Future Transportation

Our reliance on conventional fossil fuels has triggered serious environmental degradation, accelerated the climate crisis, and rapidly exhausted the planet's finite natural reserves. To address these issues, eco-friendly energy sources, known as renewable energies, are gaining significant attention [1].

Currently, the transportation sector accounts for roughly 25% of global energy consumption, predominantly depending on fossil fuels, which substantially intensifies environmental issues [2]. Aviation plays a critical role in this context, as it represents a notable and steadily increasing source of emissions. According to the International Energy Agency (IEA), in 2022 the sector accounted for approximately 2% of worldwide energy-related CO_2 emissions, with its growth trajectory surpassing that of rail, road, and maritime transport in recent decades. By that year, aviation emissions had rebounded to nearly 80% of pre-pandemic levels, and forecasts suggest that they will surpass 2019 figures by around 2025 and could triple by 2050 if current trends persist [3, 4]. Beyond the release of CO_2, aircraft operations generate additional pollutants that impose substantial indirect effects on the climate system. The combustion of jet fuel produces carbon monoxide (CO), nitrogen oxides (NO_x), water vapor (H_2O), volatile organic compounds (VOCs), sulfate ions (SO_4^{2-}), particulate matter (PM), and soot [5]. The combined influence of CO_2, NO_x, water vapor,

and contrail formation significantly contributes to radiative forcing, thereby intensifying the role of aviation in driving climate change [6].

Over the past few decades, there has been an increasing range of hybrid electric vehicles (HEVs), which combine electric motors with internal combustion engines, as well as fully electric battery electric vehicles (BEVs). These advancements have met the growing demand for sustainable and locally emission-free transportation [7].

BEVs face challenges including shorter driving range compared to HEVs and the need for extensive charging infrastructure. Efforts to improve BEV mileage focus on enhancing gravimetric and volumetric energy density. However, for heavy-duty vehicles (HDVs), current battery technology struggles to meet high power and long-distance travel requirements. Fast charging to minimize trip time and durable components are also key economic factors for HDVs [8].

Hydrogen is expected to play a key role in future energy systems, with its usage by 2050 estimated at 187 MMT under weak policies, meeting 7% of energy needs in a 1.5-degree warming scenario. Strong policies could increase hydrogen use to 696 MMT, covering 24% of final energy demand, requiring over $11 trillion in infrastructure investments. Full adoption across sectors could push demand to 1,370 MMT. These projections and related information are illustrated in Fig. 1-1 [9]. Based on this figure, the transportation sector's share is significant, accounting for 33.1% in the maximum scenario (1584 MMT), 43.2% in the strong policy scenario (301 MMT), and 65.8% in the weak policy scenario (123 MMT).

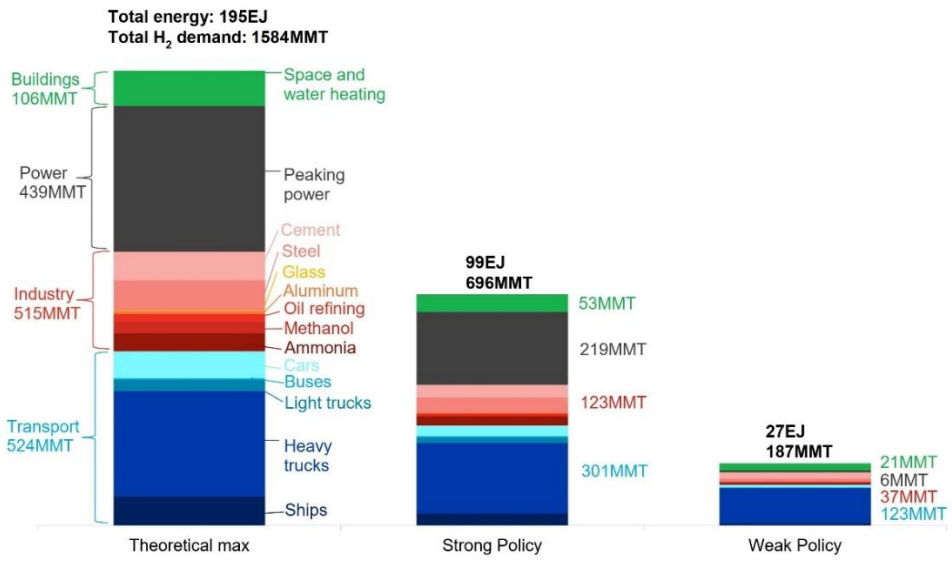

Fig. 1-1. Projected hydrogen demand across various scenarios by 2050 [9].

Implementing fuel cell (FC) system technology as the primary energy source of HDVs could be advantageous due to hydrogen's high gravimetric energy density and the capability for rapid refueling. Despite ongoing challenges such as large-scale hydrogen production, distribution, storage infrastructure, and safe handling within both infrastructure and vehicle fuel systems [10], FC vehicles present a promising solution for high-energy applications [11].

1.1.2 Fuel Cell Hybrid Electric Vehicles

There are several types of commercially available FCs, including proton exchange membrane FCs (PEMFCs), solid oxide FCs, alkaline FCs, and direct methanol FCs. Among these, PEMFC technology has gained widespread use, particularly in vehicular applications [12]. The popularity of PEMFC systems can be attributed to several advantages, including their ability to operate at low temperatures, tolerance of CO_2, and use of atmospheric air as an oxidant. They also exhibit high voltage, current, and power density, work safely at low

pressure, and tolerate differences in reactant pressure. Additionally, PEMFCs are compact, robust, mechanically simple, and made of stable materials, enhancing their reliability [13].

Despite significant advancements in FCs, they have a slow response to power demands, experience voltage fluctuations with load variations, face cold start issues in cold climates, and cannot absorb braking energy. As a result, a standalone FC system is unable to fulfill all FC vehicle requirements. Therefore, integrating a secondary power source, such as a battery or supercapacitor (SC), is essential to handle fast dynamic loads, reduce PEMFC degradation by absorbing power peaks, improve fuel economy, power the vehicle during cold starts, and enable energy recovery. Common hybridization structures for FC hybrid electric vehicles (FC-HEVs) include FC-battery, FC-SC, and FC-battery-SC configurations. Each has its own advantages and disadvantages [14].

The FC-battery structure is widely used in practical FC-HEVs [15, 16]. In this configuration, the PEMFC serves as the primary power source, connected to the load via a unidirectional converter, while the battery, as the secondary source, is directly connected to the DC bus. This setup offers lower powertrain costs and reduced fuel consumption compared to the FC-SC system [14]. The FC-battery-SC configuration, though, offers even lower fuel consumption and can extend battery life, but it has higher costs, mass, and volume due to the need for an additional converter. Among various rechargeable batteries, the lithium-ion batteries (LiBs) are considered a promising secondary source for FC-HEVs due to its high capacity, multiple charge-discharge cycles, and reasonable cost [17].

1.1.3 Heavy Duty Vehicles

Although the development of FCs for light-duty vehicles (LDVs) has spanned over twenty years, substantial attention to their application in HDVs is a more recent phenomenon. This renewed interest is driven by the inherent scalability of FCs in terms of power and energy, which can be enhanced by increasing the size of the FC stack or hydrogen tank with only a limited increase in weight compared to LiBs. Additionally, the commercial deployment of HDVs demands less infrastructure investment since fewer refueling stations are needed, owing to the specific and predictable routes typically used by these vehicles [18]. Also, the HDV sector plays a crucial role in efforts to reduce energy consumption and emissions. Currently, medium- and heavy-duty trucks account for 25% of the total annual vehicle fuel consumption and generate 23% of the total carbon dioxide emissions in the United States [19, 20]. Moreover, the annual mileage of freight trucks is expected to rise by 54% by 2050 [18].

FCs can be utilized in various sectors, including heavy-duty transportation, where they are being integrated into HEVs across both passenger and commercial applications. They are also being evaluated for freight, regional, and switcher locomotives, offering efficiency improvements over conventional engines. In maritime applications, FCs are being considered to meet stringent emission reduction targets, particularly for reducing sulfur and CO2 emissions in marine fuels [21, 22]. Fig. 1-2 illustrates the roadmap for transitioning FC applications from LDVs to medium- and heavy-duty applications, emphasizing the paradigm shift in daily mileage and power output needs.

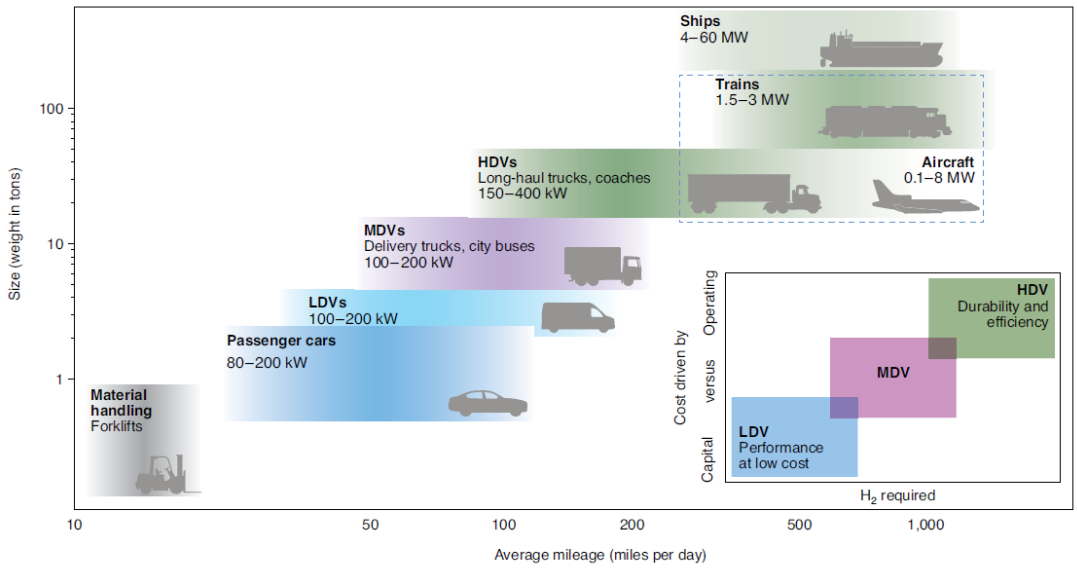

Fig. 1-2. Variety of FC applications in transportation [18].

1.1.4 Multi-stack Structure

The literature frequently discusses the use of high-power single-stack FC systems in the powertrains of FC-HEVs [23-25]. However, HDVs often require power levels that exceed the capacity of a single-stack FC system, making the use of such systems impractical. As a result, researchers are increasingly turning to multi-stack FC systems (MFCSs) that use multiple low-power FCs operating independently. Also, MFCSs offer superior performance in terms of efficiency, and reliability (availability and durability), flexible architecture and overall cost decline compared to single FC systems [26].

An MFCS enhances the overall efficiency of the system, particularly in high-power applications where a single-stack FCS cannot consistently operate within its optimal efficiency range. Unlike a single-stack FC, which has only one ideal operating point, a MFCS allows access to multiple optimal points. Fig. 1-3 illustrates the impact of adopting a multi-stack configuration on the efficiency of FCSs. The blue curve shows the efficiency curve of a single-stack FCS which has one extremum point in which the system has the

maximum efficiency. The red curve shows the efficiency curve of a dual-stack FCS, which enables operation with two local maximum points of efficiency. MFCSs offer greater flexibility in power management, providing multiple options for power distribution to achieve higher efficiency under varying load conditions [27].

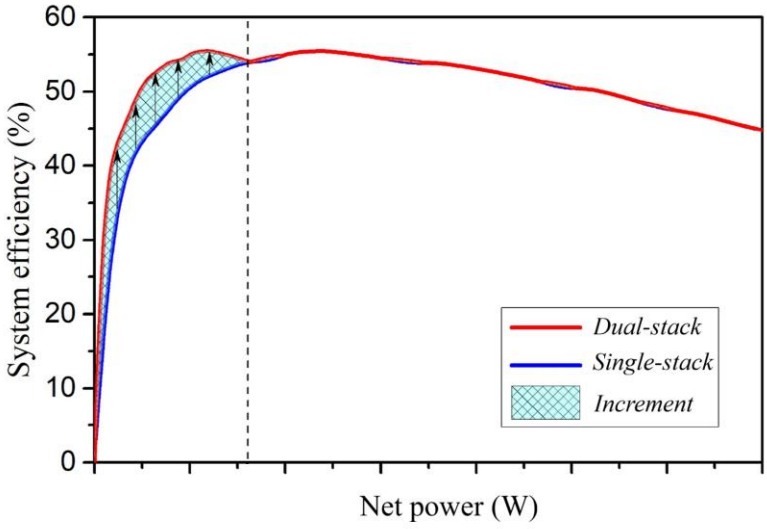

Fig. 1-3. Comparison of efficiencies of a single-stack FCS and a dual-stack FCS [28].

An MFCS can enhance both availability and durability by incorporating a redundancy function within the system, which helps prevent performance degradation through excess operational flexibility without requiring human intervention. This redundancy reduces the risk of performance decline by continuously monitoring the functioning of individual modules. In case of a malfunction, the MFCS can operate in a degraded mode, ensuring continued functionality, which is not possible in single power source systems. Regarding durability, an MFCS ensures that components such as FCs and batteries operate within their optimal efficiency zones to meet power demands. During low-power conditions, only a few modules are active, while the rest remain unused, reducing their degradation and extending the system's overall lifespan. If a malfunction occurs, the system can be reconfigured,

replacing the faulty modules without interrupting operation. The system’s modularity prevents cascading failures and supports continuous operation.

A flexible architectural arrangement is another key advantage of MFCSs, as it introduces an additional degree of freedom that facilitates the design of the vehicle. This arrangement plays a crucial role in enhancing vehicle stability and handling, both of which are heavily influenced by the vehicle's center of gravity, which is related to its mass. The stability during normal and maneuvering operations is significantly affected by the center of gravity's position in longitudinal, lateral, and vertical orientations. By strategically arranging powertrain components, the mass distribution of the vehicle can be optimized. In MFCSs, the use of multiple low-power modules, as opposed to a single high-power source, allows for more effective distribution of mass, leading to improved vehicle stability and safer handling.

Another key benefit of using MFCS is achieving economies of scale and enabling large-scale production in power systems. By adjusting the number of modules, MFCS allows the use of the same basic module across a wide range of power demands. Multiple similar modules produced by a single line can be combined to meet various power requirements, leading to reduced average costs as production increases. While the initial cost of designing and implementing MFCS is higher than a single-source system, the modularity reduces long-term expenses, as replacing a low-power module is cheaper than replacing a high-power one.

1.1.5 Energy Management Strategy

The benefits of MFCSs stem from the system's hardware, which evolves from a single-stack to a multi-stack configuration. This transformation introduces multiple power sources, including FC stacks and a battery, each with unique energy characteristics. As a result, a carefully designed energy management strategy (EMS) becomes essential. The EMS, which serves as the software component of the system, plays a critical role in managing these power sources. Its main objective is to efficiently distribute power to meet demand, while minimizing hydrogen consumption, reducing the degradation of the power sources, and optimizing overall system performance or any other key performance indicators. EMSs are classified into three main categories in the literature: rule-based, optimization-based, and intelligent-based approaches [29].

Rule-based EMSs are particularly noted for their straightforward design, minimal computational requirements, and ease of implementation. However, these strategies depend largely on rules derived from experience, which makes it challenging to guarantee optimal control. Consequently, there has been a notable shift in research toward optimization-based EMSs, which are more capable of achieving optimal performance.

Optimization-based EMSs generally focus on defining an objective function with corresponding constraints, which are then minimized to improve control outcomes [30]. These strategies are divided into two main types: online and offline methods. Considerable research has been dedicated to real-time and online EMSs, exploring various approaches that emphasize immediate or instantaneous optimization. Nevertheless, these methods tend to concentrate on optimizing individual time intervals, which limits their scope to a narrow domain. This raises questions about the overall effectiveness of these strategies in

achieving optimal solutions. Dynamic programming (DP) and Pontryagin's Minimum Principle are the offline methods having the capability of finding global optimal solution.

Intelligent-based methods utilize sophisticated data analysis techniques to derive optimal control policies by learning from both past and current data. Unlike traditional approaches, these methods do not rely on exact system models but require the development of a comprehensive and appropriately sized dataset, a process that is often time-consuming and complicated. Techniques encompassed within this category include reinforcement learning, neural network training, and various classification algorithms [31].

1.1.6 FC Stack Sizing and Allocation, and Battery Sizing

Achieving the advantages of FC-HEVs in terms of optimal performance and efficiency necessitates precise sizing of both the FC and battery. The FC must be appropriately sized to meet the vehicle’s power demands while minimizing weight and cost, and the energy storage system must be sized to provide adequate energy capacity and power delivery capabilities [32]. Insufficient sizing can fail to meet driving requirements, while excessive sizing can lead to unnecessary increases in cost and mass [33]. Consequently, improper sizing and elevating vehicle costs, potentially make the FC-HEV less attractive to consumers. In HDVs, where power demands and durability requirements are particularly high, the need for precise sizing becomes even more critical for accurate cost estimation. Effective cost estimation is essential for evaluating the economic feasibility of these vehicles [34].

In addition to component sizing, the number of FC stacks is also a crucial design factor in MFCSs. Assuming an FCS should supply the power for a load. This system can have 2,

3, 4, or more FC stacks. It is evident that the number of stacks will influence both the initial investment cost and the operational cost of the system. For example, utilizing a greater number of stacks allows the EMS to activate specific FCs according to power demands, potentially lowering degradation rates and reducing hydrogen consumption.

Now, let it be considered that the number of stacks is predetermined to be N to supply load P. If all stacks are equal, the nominal power of each stack should be P/N. However, if the rated power of the FC stacks can be unequal, numerous configurations for supplying the load will arise. In each of these combinations, the investment cost for the system will vary. Furthermore, since the specifications of the stacks differ in each combination, the efficiency, degradation and operational cost for a constant load will also differ across the various combinations. Hence, it is essential to acknowledge that both the number of stacks and their chosen rated power play a critical role in influencing key performance outcomes when designing a MFCS.

1.2 Literature Review

The aim of this literature review is to provide a comprehensive and critical analysis of existing research relevant to the energy management and sizing of multi-stack FC-HEVs. This section synthesizes advancements and challenges in EMSs with a particular focus on their application to MFCSs. Additionally, it examines the methodologies and considerations involved in the sizing of FC stacks and battery systems. By identifying gaps and limitations in current studies, this review establishes the foundation for the novel contributions and integrated frameworks developed in this thesis.

1.2.1 EMS in Multi-Stack FC-HEVs

EMSs for MFCSs are essential for coordinating multiple power sources to meet load demands efficiently. These strategies broadly fall into three categories: rule-based, optimization-based, and intelligent-based methods. Each category offers different trade-offs in complexity, optimality, and adaptability, addressing key goals such as minimizing hydrogen consumption and component degradation while enhancing overall system performance.

1.2.1.1 Rule-based EMS

The widespread adoption of rule-based EMS is mainly due to their uncomplicated structure and low processing needs, making them very easy to put into operation. Two EMSs, equal distribution and daisy chain, were developed and compared based on their characteristics in [35]. Following this comparison, a novel adaptive strategy called the rotary daisy chain was introduced. This adaptive strategy aims to distribute power between the MFCS and battery while considering the unique attributes of each stack's maximum power and maximum efficiency points. The authors of [36] presented a method for optimizing coordination within the MFCS, aimed at reducing overall energy consumption. The MFCS's efficiency distribution function could be obtained using the energy consumption model of the single stack with varying parameters. They validated this approach through experiments on a 100-kW water-cooled stack. In [37], the authors introduced an EMS using recursive least square to reduce the hydrogen consumption and increase system efficiency compared to power average and daisy chain algorithms. One significant drawback of rule-based EMSs is its dependence on experiential knowledge, which often fails to ensure the system operates at its peak theoretical efficiency. Hence, to

attain optimal control, a growing number of researchers have shifted their attention toward investigating optimization-based EMSs.

1.2.1.2 Optimization-based EMS

Generally, optimization-based strategies are built by defining a specific cost function and its related constraints, which the system then tries to minimize to reach better control results [30]. These methods are broadly split into two groups: those that run in real-time and those that calculate solutions ahead of time. A lot of work has gone into developing online strategies that look for the best settings at each individual second of operation. The authors of [38] introduced an online hierarchical approach of EMS, aiming to thoroughly address the interdependence between the power distribution at the top level among various system clusters and the power distribution at the bottom level within each specific system cluster. The authors of [39] have introduced a hierarchical EMS based on sequential quadratic programming (SQP) to determine the share of power of each power source in a hybrid locomotive powertrain including dual-stack FCS and a battery. Their proposed EMS performed better than equivalent consumption minimization strategy (ECMS) in terms of efficiency and hydrogen consumption. In [40], the investigation centered on the development of an ECMS for a FC-HEV, including four FC stacks and a battery pack. The article [41] introduced a novel approach for EMS of aircraft that integrated system cost considerations into the ECMS, utilizing a SQP algorithm. This approach aimed to enhance MFCS efficiency, cut overall system costs, mitigate power fluctuations in the FCS, and safeguard underperforming stacks, thereby extending the system's lifespan. [42] presented an online extremum-seeking EMS for a FC/SC hybrid electric tram. The strategy aimed to identify the FC's optimal efficiency and power points. Results indicated substantial

hydrogen consumption savings of 43.92% and 23.49%, along with improved stack efficiency of 2.61% and 17.31%, respectively, when compared to the state machine control strategy and the ECMS. In [43], a decentralized EMS based on model predictive control (MPC) was proposed for a modular FC powertrain to minimize the cumulative operational cost of the system. However, the online optimization techniques discussed above focus on a localized domain because they optimize for individual time steps. Because of this, whether these techniques can actually reach a truly global best solution is still a subject of active debate. When the goal is to find the global EMS, DP is often seen as the most powerful tool available. Compared to Pontryagin's Minimum Principle method, DP provides better flexibility in terms of the nature of constraints, and the feasibility of obtaining and implementing the solution. There are many papers in the energy management of systems including single-stack FC in which DP was used to reach the optimal solution. For instance, the authors of [44] introduced an innovative EMS for a FC hybrid bus, combining DP and fuzzy logic. The results demonstrated significant optimization advantages, especially in scenarios with high energy demands and low initial State of Charge (SOC). This approach led to an impressive 8.97% improvement in fuel economy. [45] introduced an EMS for a FC hybrid tramway, which combined DP and a state machine approach to optimize power distribution between the FC and supercapacitor while considering FC durability and hydrogen consumption. A cost-minimization strategy that encompassed both fuel consumption and the degradation of FC in a tram was introduced in [46]. The article presented a computationally efficient multidimensional DP approach to find the optimal control trajectory of the problem. The proposed strategy decreased FC degradation by a minimum of one-third, leading to an overall reduction in composite operating costs of at least 8.66% when compared to conventional approaches. The FCS of these articles included

one FC stack in its structure. The primary hurdle with DP is that the computational demands grow exponentially as more control variables are included, a problem commonly called the curse of dimensionality. Hence, there are not several papers in MFCSs area using DP as their EMS. The authors of [47, 48] conducted a comparison of their proposed method against DP as a benchmark for validation. However, it is important to note that the DP approach employed in these studies evenly distributed power across all stacks. As an illustration, even in situations where a single FC stack could adequately meet low power demands, all the stacks were actively involved. This applies more degradation to FC stacks and increases the operation cost of the system. Furthermore, most existing DP models do not take component health into account, meaning they operate without any real knowledge of how much the FC stacks have degraded over time.

1.2.1.3 Intelligent-based EMS

The application of intelligent-based EMSs in MFCS is still relatively scarce. In [47], a three-layer EMS was proposed that integrates Q-learning, a model-free reinforcement learning algorithm, to meet power demand while lowering hydrogen consumption and mitigating component degradation costs. An EMS based on independent Q-learning, a multi-agent reinforcement learning framework, was introduced in [49] with the aim of controlling battery SOC and reducing hydrogen usage. Likewise, a decentralized reinforcement learning EMS for FC-HEVs with two parallel FC systems and a battery was presented in [50]. This multi-agent structure improves convergence speed and optimization through modular and interconnected learning processes. However, despite the advantages of being model-free, these EMSs are still in an early development stage.

1.2.2 Sizing in FC-HEVs

FC-HEVs incorporate multiple energy sources, requiring optimal sizing to enhance efficiency, reduce fuel consumption, and extend the lifespan of the hybrid components [51, 52]. The authors of [53] introduced a vehicle powered by a FC-battery configuration, benchmarked against the first generation Toyota Mirai FC vehicle under varying driving conditions. The proposed configuration demonstrated a 10.5% improvement in gradeability performance compared to the Toyota benchmark. Additionally, the cost of the hybrid power source was reduced by 28% through the use of optimal component sizing. In [54], a comprehensive sizing analysis of an FC-battery bus was conducted to determine the optimal hybrid configuration, considering the degradation of both the FC stack and battery over time. It was shown that a small FC stack degraded rapidly, while an FC-dominated configuration shortened stack life due to high transient power demands. In contrast, a battery-dominated system extended stack life and minimized lifetime costs. The findings also revealed that the optimal configuration was highly dependent on specific drive cycle characteristics, emphasizing the importance of matching the hybrid setup to the vehicle's actual operational routes. The decarbonization of rail freight and passenger transport was investigated by [55], focusing on hybrid locomotives utilizing regenerative braking and FC systems. Real-world data from locomotives on seven railway corridors were used to calculate the optimal battery capacities and FC power configurations. It was found that longer, energy-intensive routes required higher FC power, while shorter routes needed only minimal FC power. The results showed higher battery capacity to FC power ratios compared to previous studies, likely due to the use of real locomotive data. In a detailed study of FC-battery hybrid buses in [54], the impact of component sizing on vehicle

performance and cost was examined. The research found that both FC and battery sizes significantly influenced the vehicle's fuel economy, durability, and overall lifetime cost. Smaller FC stacks, while cost-effective under low power demand cycles, led to rapid degradation and higher fuel consumption in high-demand scenarios. Conversely, FC-dominant configurations, although extending the range, suffered from increased degradation and higher initial costs. The optimal configuration identified was a battery-dominated system with a moderately-sized FC, which balanced longevity and cost-effectiveness. This configuration demonstrated advantages across different driving cycles, highlighting the necessity of matching component sizing to specific operational requirements in order to minimize the vehicle's lifetime cost. The methodology in [56] focused on sizing FC electrified propulsion systems for heavy-duty trucks with the goal of minimizing the total cost of ownership. It evaluated retail prices, hydrogen, and electricity costs across present and future scenarios, comparing FC and battery electric powertrains. While current cost factors favored battery electric trucks, the methodology demonstrated the economic viability of FC electrified powertrains in 10- and 30-year projections due to anticipated cost reductions. Future research aimed to refine EMSs and enhance the computational efficiency of the methodology.

In aircraft, precise sizing becomes even more crucial, as stringent weight constraints significantly magnify the consequences of sizing choices. Numerous studies have investigated PEMFC and battery sizing in hybrid-electric aircraft, with the central objective of satisfying operational needs such as range, endurance, and payload capacity while simultaneously lowering emissions. Study [57] emphasized maximizing endurance while maintaining competitive range in a regional aircraft, whereas [58] focused on reducing

emissions without compromising range and climb performance relative to conventional propulsion. Research in [59] and [25] targeted fulfilling range and endurance requirements alongside substantial emission reductions. A techno-economic framework was developed in [60] to explore cost-performance trade-offs, evaluating performance in terms of range and payload capacity. Similarly, [61] applied a possibility-based optimization method that considered uncertainties in propulsion, structural, and aerodynamic parameters, identifying stall speed, maximum speed, and maximum takeoff weight as the most restrictive constraints. Across these works, hydrogen storage was identified as the primary contributor to additional weight, while other subsystems received less attention, and weight was reported only as a calculated outcome rather than being explicitly optimized. Furthermore, all above-mentioned investigations, in both ground and aviation sections, have been limited to single-stack FC layouts, leaving the potential advantages of multi-stack configurations unaddressed.

Research on MFCS sizing has mainly focused on ground vehicles, concentrating on stack allocation or a limited set of predefined configurations. These efforts have not addressed the simultaneous optimization of individual stack sizes together with battery system. For example, the work in [62] examined modular FC setups with differential control, reporting reductions in total ownership costs and emissions by up to 23%, but this was limited to three dual-stack configurations. Similarly, [63] and [64] conducted stack allocation analyses with a fixed overall FCS size, utilizing bi-level and multi-objective optimization techniques to improve system efficiency, extend stack longevity, and cut costs, demonstrating clear performance advantages over equal-sized stack arrangements. The study in [65] found that increasing the number of stacks from two to three and then to

four led to operational cost savings of 6.33% and 14.87%, respectively. Despite these promising findings on optimized stack allocation, none of the existing research has addressed the comprehensive sizing of multiple stacks alongside battery in an integrated manner. Also, to date, there is a noticeable absence of investigations focused on MFCS sizing within the aircraft industry.

1.2.3 Integrated Sizing and EMS in FCHEVs

Some studies indicated that optimal sizing and EMS should be developed simultaneously [66]. When these strategies are handled separately, the performance of hybrid sources deteriorates, leading to increased costs for energy storage systems [67]. A recent study in [68] explored an innovative method for optimizing component sizes and power distribution in vehicles to enhance the lifespan of the FC stack and improve fuel economy. Using experimental data from the Toyota Mirai and MATLAB-SIMULINK for modeling, the study established optimal values for the FC stack at 96 kW, the battery at 3.05 kWh, and the electric motor. This approach led to a fuel consumption improvement of 10% to 21% under various driving conditions. Additionally, the strategy reduced the vehicle's initial cost by $1,328 and cut annual operational costs by $691. The study demonstrated that while the new strategy enhances overall FC efficiency and durability, it also requires careful consideration of cost-performance trade-offs, particularly in managing FC efficiency at different SOCs. The authors of [69] focused on the modeling, sizing, and EMS of FC-HEVs, aiming to reduce operational costs and improve drivability. A tunnel DP method was employed to optimize power distribution between the battery and FC, while a Pareto front analysis determined the optimal sizes of FC and battery for various driving cycles. The research highlighted the advantages of a lithium titanate battery, superior in

power capacity and safety. Compared to a commercial vehicle, the proposed model demonstrated enhanced efficiency, lower hydrogen consumption, and superior performance in meeting drivability constraints. The proposed method in [70] investigated the effects of FC and battery sizes on the performance, fuel consumption, degradation, and overall running cost of FCHEVs. The study found that while larger FCs could reduce fuel consumption by operating closer to peak efficiency, they also increased costs and degradation due to start/stop cycling. It was suggested that slightly downsizing the FC, alongside an optimally controlled EMS, might achieve a better balance between running costs and efficiency. Although the research focused on a low-power vehicle, the findings are relevant to other vehicle types, highlighting the need to carefully consider the trade-offs between efficiency, cost, and degradation in FC design. In [71], the power distribution and component sizing for FC-battery hybrid excavators were investigated using dynamic programming to develop an operational strategy. The study found that increasing the number of cells of the FC reduced hydrogen fuel consumption and improved the battery SOC. However, maintaining SOC became challenging with more than 60 cells due to decreased maximum battery power. The optimal configuration was determined to be 50-55 cells, with FC power between 11-13 kW and battery power between 2-4 kW. This research demonstrated the potential for FCs to replace traditional diesel or gas engines and emphasized the importance of precise power source sizing to enhance efficiency in hybrid vehicles. In [72], the authors explored the optimization of power distribution and design for a FC-HEV with a battery-SC hybrid energy storage system (HESS) using an interactive adaptive-weight genetic algorithm. The objective was to enhance the vehicle's driving range, extend the lifespan of the FC stack and battery, and reduce hydrogen consumption and HESS size. The EMS utilized fuzzy logic controllers to manage power distribution

between the FCS and HESS components. The optimized FC-HEV achieved a driving range of 444 km and a hydrogen consumption of 0.9009 kg/100 km under standardized cycles, showing robustness in real-world conditions with improved energy efficiency and power source lifespan. The cost-benefit analysis demonstrated a significant reduction in the cost-to-autonomy ratio by up to 63.59% compared to other electrified vehicle powertrain configurations. A cost-effective approach for designing and operating FC-HEVs through chance-constrained optimization was introduced in [73]. This method aimed to reduce both component and operational costs while taking into account fuel FC degradation and the cycle life of the energy buffer. The optimization was divided into two sub-problems and addressed using sequential convex programming, which allowed for the downsizing of crucial components such as the FC, and energy buffer. A case study explored three energy buffer technologies (SC, LiB, and lithium-ion capacitors (LiC)) across four trucking applications: urban delivery, regional delivery, construction, and long-haul. LiB was found to be the most cost-effective option, while LiC allowed for an increase in payload capacity by 374 kg to 736 kg in long-haul applications compared to LiB and SC. Notably, all of these studies in integrated sizing and EMS, have focused exclusively on ground vehicle applications and do not consider multi-stack configurations, leaving a significant research gap in the exploration of integrated MFCS sizing and EMSs.

1.3 Problem Statement and Conceptual Framework

The challenges addressed in this thesis encompass two issues: first, the absence of a reliable offline benchmark EMS specifically designed for MFCS, and second, the lack of scalable, integrated methodologies that simultaneously optimize component sizing and

EMS for MFCS powertrains spanning ground and aircraft applications while addressing investment cost, operational cost and durability, and, in aircraft contexts, propulsion weight considerations. This research contributes to the state-of-the-art through three developments: a scalable offline benchmark EMS for MFCSs, a constrained exploration method (CEM) that serves as a computationally tractable reference standard; an HDV-focused integrated sizing and EMS framework, termed Integrated Sizing and Energy Management Strategy (ISEMS), that unifies component sizing with operational control; and an aircraft-specific multi-objective integrated sizing and EMS framework, designated Multi-objective Integrated Sizing and Energy Management Strategy (MISEMS), that optimizes both cost and weight while considering power-demand uncertainty. Fig. 1-4 summarizes the scope of this thesis, linking the target applications to the MFCS and to the three core contributions: CEM, ISEMS, and MISEMS.

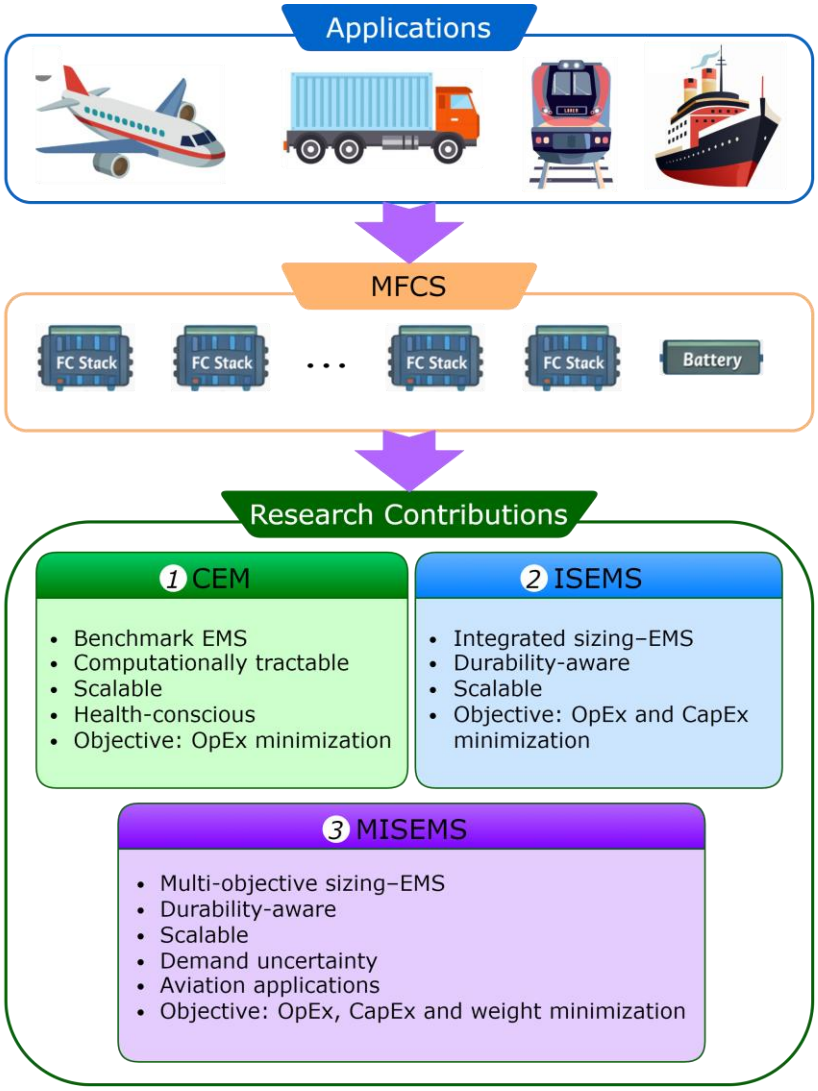

Fig. 1-4. Overview of applications and main research contributions.

1.4 Aims and Objectives

1.4.1 Constrained Exploration Method

There is a clear gap in practical, general offline benchmark EMSs for MFCS that can serve as a common reference across rule-based, online, and learning-based strategies over different multi-stack designs. While DP is the default offline gold standard in single-stack systems, its direct application to MFCS becomes computationally intractable because the

grid size grows exponentially with added stacks and variables, which forces coarse discretization and other simplifications that reduce its value as a true benchmark in multi-stack settings. In practice, such DP-based MFCS tests often spread power evenly at light loads triggering frequent FC stacks switching. Also, this type of DP in the literature has not considered state of health (SOH) of FC stacks, yielding activation patterns that overuse weaker stacks and inflate hydrogen consumption and degradation.

Addressing this gap calls for scalable, health-aware offline benchmarks that keep full constraint handling and explicit SOH weighting while avoiding the curse of dimensionality; CEM is proposed to achieve this by pruning infeasible or low-value regions of the search space, remaining tractable, and still yielding activation patterns consistent with MFCS durability-aware operation. The proposed CEM provides a new, health-conscious reference standard for MFCSs, significantly lowering both running burden and the time required for numerical analysis. The effectiveness of the proposed method is validated through tests conducted on three HDVs as case studies: an aircraft, a tramway, and a truck.

1.4.2 Integrated Sizing and Energy Management Strategy

Conventional MFCS design flows separate sizing from EMS or predefine total FC capacity before allocation, which obscures key trade-offs across stack count, heterogeneous ratings, and battery size, and how these choices shape operating cost, investment cost, and durability in practice; most integrated sizing–EMS studies focus on single-stack systems, leaving a gap for MFCS approaches that co-optimize discrete stack selection, unequal ratings, and battery configuration together with EMS-coupled evaluation. The aim of ISEMS is to fill this gap by establishing an integrated, degradation-aware framework that jointly determines MFCS modularity, heterogeneous stack ratings, and battery sizing while

evaluating total cost (including investment and operational costs) and durability implications under realistic mission constraints, without fixing total FC capacity in advance. Specifically, ISEMS determines the FC stack and battery sizes to minimize total cost while balancing degradation; quantifies how the number of stacks and unequal ratings influence the total cost of the MFCS; and clarifies the role of battery SOC limits in shaping different costs, so that modularity choice, stack rating selection, and battery sizing become primary sizing decisions rather than downstream allocation steps.

1.4.3 Multi-objective Integrated Sizing and Energy Management Strategy

Aircraft industry introduces distinct requirements: much prior work relies on single-stack designs, does not co-optimize propulsion weight with cost, and does not integrate MFCS sizing with EMS, leaving potential multi-stack benefits underutilized in a high-power sector. Moreover, weight is often reported rather than optimized, and ignoring mission uncertainty risks either oversizing or latent shortfalls, motivating a robust, multi-objective, EMS-in-the-loop design for aircraft MFCS.

The aims of MISEMS are to establish a framework for MFCSs that jointly targets reductions in total cost and total weight of propulsion in aircraft, to explicitly account for durability via SOH considerations in both sizing and EMS objectives, and to ensure robustness of sizing decisions by considering uncertainty in mission power demand. MISEMS further aims to treat the number of stacks and their ratings as primary sizing choices rather than fixed inputs, enabling assessment of how modularity and heterogeneity shape cost–weight trade-offs in aircraft contexts.

1.5 Contribution of the Research

1.5.1 Constrained Exploration Method

The contributions of the thesis in benchmark EMS in MFCS configurations are as follows:

- A scalable offline EMS is developed to optimally distribute power among multiple FC stacks in HDVs. The dimensionality growth of DP is mitigated by redefining the state space. Thanks to this structure, the EMS is applicable to MFCSs, including aircraft, tramway, and truck configurations, where classical level-set DP either becomes intractable or fails to converge.
- Health awareness is incorporated directly in the objective via an SOH-based penalty that increases the marginal cost of dispatching more degraded stacks, whereby power allocation is steered toward durability while satisfying load and FCSs constraints; through this health-conscious formulation, continuous accounting for each stack's condition is ensured and lower SOH units are protected without sacrificing feasibility under transient demand.
- Time efficiency is obtained by three coordinated filters that confine exploration to only feasible and reachable space while maintaining solution optimality, namely a battery-power filter, an SOC-range filter, and an SOC filter. These filters substantially reduce computation time while retaining benchmark accuracy for multi-stack cases.

1.5.2 Integrated Sizing and Energy Management Strategy

The contributions of the ISEMS are summarized as follows, highlighting integrated sizing and control decisions, SOH-aware durability, and cost optimization driven by stack architecture across MFCS configurations.

- An optimization-based framework is proposed to simultaneously address sizing and EMS in MFCSs, with both operational and investment costs minimized as joint objectives; operational cost aggregates hydrogen use and degradation of FC stacks and the battery over the mission, while investment cost covers FC stacks, converters, and battery, scaled to mission-level via a degradation-weighted normalization that penalizes designs with shorter lifetime, thereby aligning short-horizon EMS behavior with long-horizon sizing decisions.
- The sizing and allocation of FC stacks are managed within a unified framework, eliminating the common practice of fixing total FC capacity in advance and thereby enabling advantageous heterogeneous selections while avoiding the suboptimal allocations that arise from predetermined stack sizes.
- The battery size and FC configuration are jointly determined with SOH constraints incorporated for both EMS and sizing; SOH-aware penalty within the EMS elevates the marginal cost of dispatching degraded stacks, while this penalty in the sizing level leads to producing designs that are not only cost-efficient but also durable across repeated missions.
- Optimal FCS sizes are established for different numbers of FC stacks, and the influence of stack quantity on investment and operational costs is systematically

analyzed; this analysis reveals where adding more stacks no longer lowers total cost, clarifying the modularity levels that achieve the minimum.

1.5.3 Multi-objective Integrated Sizing and Energy Management Strategy

The contributions of the MISEMS are summarized as follows:

- A multi-objective framework is developed for coordinating the sizing and EMS of multiple FCSs and a battery in aircraft applications, explicitly targeting reductions in both powertrain cost and weight; the objectives combine investment expenses for FC stacks, converters, hydrogen storage, and the battery with operational costs based on hydrogen consumption and component degradation, while the weight metric aggregates all propulsion subsystems weights.
- A durable system design is ensured by MISEMS, in which the sizes of the battery and FC stacks are determined together while the SOH of both units is explicitly taken into account; SOH enters both the sizing constraints and the operational cost terms so that configurations that accelerate wear are penalized, steering the selection toward solutions that satisfy end-of-life criteria over repeated missions.
- Uncertainty in the required power profile is included in the optimization process, allowing robust sizing choices to be made so that the system's ability to satisfy the load under demand changes is guaranteed; representative demand scenarios are generated and reduced, and sizing candidates are evaluated across

these scenarios so that selected sizes maintain feasibility and cost performance despite load perturbations.

- Instead of being handled as separate tasks with a fixed total FC capacity, the sizing and allocation of FCSs are managed as a single, combined procedure; the number and rating of individual stacks are chosen together without fixing aggregate power in advance.
- The influence of stack quantity on total cost and weight is analyzed, clarifying trade-offs among investment cost, operational cost, and mass in aircraft multi-stack configurations. The analysis identifies the number of stacks for which reduced degradation lowers the normalized investment cost per mission sufficiently to compensate for the additional mass and capital expense, as well as the numbers of stacks where this compensation does not occur. This approach effectively maps the cost–weight optimum across different stack quantities.

1.6 Methodology

The methodology uses one shared MFCS modeling spine and applies methods appropriate to each study. The architecture is a parallel MFCS on a common DC bus with per-stack unidirectional DC–DC converters and a bidirectional ESS converter, enabling independent stack control, redundancy, and modularity. PEMFC behavior follows a semi-empirical voltage model and a standard power–hydrogen flow relation, while degradation is modeled in a control-oriented way that penalizes start–stop, fast transients, and sustained extremes. Also, the battery uses an internal-resistance model with SOC dynamics.

1.6.1 Constrained Exploration Method

At the first stage of the project, an offline optimal EMS for a multi-stack FC-HEV aimed at reducing both fuel consumption and degradation of FC stacks is introduced. This method is anticipated to serve as a benchmark for evaluating the performance of online EMSs in future studies. To achieve this goal, a CEM is proposed for power allocation among different energy/power sources. Exploration methods often suffer from time-consuming processes and the curse of dimensionality, particularly when the number of control and state variables increases. CEM tackles this issue by defining the stacks' power commands at time k as the state at time k+1, which cuts the discretization size while preserving a global search without coarse approximations. It further narrows the search space using three filters that work together: a battery-power filter derived from the power-balance equation, an SOC-range filter that computes forward and backward reachable SOC under a terminal-SOC equality, and an SOC-interpolation filter that replaces near-grid SOC values with a single representative to prevent interpolation leakage and shorten runtime. The proposed method also utilizes a health-conscious multi-objective cost function intended for minimizing operational costs, including hydrogen consumption and FC degradation, and it always applies an SOH weight so that lower-SOH stacks are penalized during optimization.

Tests across aircraft, tram, and truck cases show that CEM supports smooth stack operation by letting the battery buffer fast changes, avoids turning on too many stacks at light load, and stays tractable even when the number of stacks would break DP. Together, these results make CEM a scalable offline benchmark for testing advanced EMSs on MFCS, closing the need for a benchmark that remains viable as modularity grows.

1.6.2 Integrated Sizing and Energy Management Strategy

ISEMS formulates an integrated mixed-integer optimization in which discrete sizing variables select FC stack models and battery layout, while an inner-loop MPC computes operating costs for each sizing candidate under SOC, power, ramp, and SOH-aware limits. The GA explores candidate configurations of MFCS–battery by encoding per-stack type indices and battery series/parallel counts, and MPC evaluates each candidate's mission performance, providing hydrogen consumption, FC and battery degradation, and constraint feasibility. The GA fitness function is a degradation-aware total cost that scales investment cost to a per-mission basis using the lifetime implied by the most degraded stack and adds operational costs based on monetized hydrogen use, FC degradation, battery degradation, and a hydrogen-equivalent term for terminal SOC difference.

ISEMS searches modularity from one to multiple stacks using both commercial and lab-characterized models. Decision variables include the discrete FC stack types, the number of battery cells in series and parallel, and the EMS control sequence determined online by MPC over a receding horizon. Constraints enforce SOC bounds, battery power limits, stack power bounds, and stack ramp-rate limits, while SOH is used to penalize operation of degraded stacks. The GA population evolves with nested MPC evaluations until convergence, yielding cost-effective designs with balanced SOH trajectories. Validation on a long-haul truck and a lab testbench demonstrates significant total-cost reductions.

In the MPC, the state is battery SOC, the control is the FC power adjustment vector, and the disturbance is the requested power. The cost over the prediction horizon sums

hydrogen usage, FC degradation weighted by SOH, and battery degradation, applying only the first control at each step.

1.6.3 Multi-objective Integrated Sizing and Energy Management Strategy

MISEMS extends the integrated sizing–operation concept to aircraft by considering two objectives: minimizing the total powertrain cost and the total propulsion weight. The framework uses an outer integer NSGA-II for sizing and the same MPC-based EMS for operational evaluation. The decision vector contains discrete FC stack model indices and battery series/parallel counts for a fixed number of stacks, and the inner EMS evaluates operating cost and constraint satisfaction for each candidate. Objectives combine scenario-averaged total cost, which uses degradation-aware scaling of investment plus operating cost, and total system weight, which sums weights of stacks, converters, compressor, cooling system, battery, and hydrogen storage.

MISEMS models power-demand uncertainty with a scenario pipeline: segment-wise bounded multiplicative noise generates scenarios, PCA retains components covering most variance, and K-means selects a small set of representative scenarios for tractable optimization. For each candidate and each representative scenario, the MPC-based EMS computes operating cost under SOC, power, ramp, and SOH limits, and NSGA-II aggregates these results to build robust Pareto fronts. The outcome is a set of MFCS–battery designs that reveal cost–weight trade-offs and demonstrate the impact of modularity and heterogeneous stack selections under load uncertainty, with consistent evaluation of EMS across all scenarios.

Chapter 2 - Benchmark EMS for Multi-Stack FC-HEVs

This chapter develops the Constrained Exploration Method as an offline benchmark EMS for MFCSs. It focuses on the formulation, filtering strategy, and validation on representative case studies.

2.1 Abstract

This paper puts forward an offline optimal energy management strategy (EMS) for a multi-stack fuel cell (FC) hybrid electric vehicle (HEV) aimed at reducing both fuel consumption and degradation of FC stacks. This method is anticipated to serve as a benchmark for evaluating the performance of online EMSs in future studies. To achieve this goal, a constrained exploration method (CEM) is proposed for power allocation among different energy/power sources. Exploration methods often suffer from time-consuming processes and the curse of dimensionality, particularly when the number of control and state variables increases. To address these issues, the proposed CEM incorporates various filters for the effective calculation of battery power, battery state of charge (SOC) range, and SOC interpolation. The proposed method also utilizes a health-conscious multi-objective cost function intended for minimizing operational costs, including hydrogen consumption and degradation. CEM is introduced as a novel scalable, health-conscious and time-efficient EMS benchmark for hybrid multi-stack FC systems, efficiently decreasing operational expenses and notably shortening simulation duration. The effectiveness of the

proposed method is validated through tests conducted on three heavy-duty vehicles as case studies. The first case involves an aircraft, the NASA X-57 Maxwell, fitted with two 50 kW stacks and a battery pack. The validation of the CEM is established by comparing it to level-set DP and sequential quadratic programming (SQP) in terms of accuracy and required calculation time. In the second case study, a tramway containing two 125 kW FC stacks is investigated. The validity of the CEM is approved by level-set DP and SQP algorithms. In the third case study, a truck is considered, equipped with four 75 kW FC stacks and a battery system. Level-set DP fails to do the power distribution in this case owing to the numerous state and control variables, whereas the proposed CEM successfully distributes the power among the power sources. Also, results from a comparison of the CEM and SQP methods demonstrate the superiority of CEM. This case study highlights the potential for scalability of the proposed methodology compared to the conventional DP approach found in the literature.

Keywords: Health-conscious energy management strategy, aeronautic, multi-stack fuel cell system, modular fuel cell system, heavy-duty vehicles, multi-objective optimization.

2.2 Introduction

The use of traditional energy sources is leading to pollution, global warming, and the depletion of natural resources [74]. The transportation industry is responsible for approximately 25% of the world's total energy usage, heavily relying on fossil fuels and significantly contributing to environmental pollution [2]. In recent years, interest in hydrogen has grown to grant renewable energy resources more flexibility to increase global

energy security. It is anticipated that hydrogen will supply 24% of the world's energy demand by 2050, of which 36% will belong to the transportation section [9].

One of the most promising choices in the transportation industry is the fuel cell (FC) hybrid electric vehicle (HEV) that uses hydrogen and is characterized by the absence of local emissions, impressive efficiency, and quick refueling time [29, 75]. An FC-HEV relies on a proton exchange membrane FC (PEMFC), as its main power generator, and a battery and/or supercapacitor, as an energy storage system (ESS) [76]. There are various types of ESS which can be used for this purpose [1]. Even though the development of FCs for light-duty vehicles (LDVs) has been ongoing for over two decades, there has been a recent surge in interest regarding their application in heavy-duty contexts. When it comes to the commercial deployment of heavy-duty vehicles (HDVs), there is a reduced need for infrastructure investment since fewer refueling stations are required, thanks to the existence of specialized and more predictable routes [18].

The utilization of a high-power single-stack FC system in the powertrain of an FC-HEV is prevalent in literature, for instance in [23-25]. However, there are HDVs that require a level of power exceeding what a single-stack FC system can provide, which is around 150 kW. Additionally, this system's operation is vulnerable to malfunctions of both the FC stack and its balance of plant components. Moreover, the relatively slow responsiveness of the auxiliary compressor and reactants, along with fluid management, impose limitations on the maximum rated power achievable by a single-stack PEMFC system [47]. In response to these limitations, some researchers have reoriented their efforts towards implementing multi-stack FC systems (MFCSs) comprising multiple low-power FCs operating autonomously. In summary, an MFCS exhibits strong performance in terms of power level,

space flexibility, and reliability compared to a single FC system [26]. Moreover, designing an MFCS enhances the modularity of the entire system. These advantages arise from the hardware of the system thanks to transforming it from a single-stack structure to a multi-stack one. Having multiple power sources in the system, including FCs and an ESS, each characterized by its own energy features, calls for the deployment of a meticulously designed energy management strategy (EMS), which is the software part of the problem. The EMS's primary duty is to meet the required power demand by efficiently allocating power among various sources, thereby minimizing hydrogen consumption, reducing the degradation of the power sources, and maximizing system reliability.

EMSs are categorized in the available literature into three groups: rule-based, optimization-based, and intelligent-based [77]. Rule-based EMSs are known for their simplicity, low computational demands, and ease of implementation. Two EMSs, equal distribution and daisy chain, were developed and compared based on their characteristics in Ref. [35]. Following this comparison, a novel adaptive strategy called the rotary daisy chain was introduced. This adaptive strategy aims to distribute power between the MFCS and battery while considering the unique attributes of each stack's maximum power and maximum efficiency points. The authors of [36] presented a method for optimizing coordination within the MFCS, aimed at reducing overall energy consumption. The MFCS's efficiency distribution function could be obtained using the energy consumption model of the single stack with varying parameters. They validated this approach through experiments on a 100-kW water-cooled stack. In [37], the authors introduced an EMS using recursive least square to reduce the hydrogen consumption and increase system efficiency compared to power average and daisy chain algorithms. It is essential to note that rule-

based EMSs heavily lean on experiential knowledge for rule creation, making it challenging to guarantee optimal control. Hence, to attain optimal control, a growing number of researchers have shifted their attention toward investigating optimization-based EMSs.

Optimization-based EMSs typically revolve around establishing an objective function along with constraints and then minimizing this function to enhance control objectives [30]. Optimization-based EMSs are categorized into online and offline methods. Extensive research in real-time and online EMSs has focused on various EMS approaches that prioritize instantaneous optimization. [38] introduced an online hierarchical approach of energy management, aiming to thoroughly address the interdependence between the power distribution at the top level among various system clusters and the power distribution at the bottom level within each specific system cluster. The authors of [39] have introduced a hierarchical EMS based on sequential quadratic programming to determine the share of power of each power source in a hybrid locomotive powertrain including dual-stack FCS and a battery. Their proposed EMS performed better than equivalent consumption minimization strategy (ECMS) in terms of efficiency and hydrogen consumption. In Ref. [40], the investigation centered on the development of an ECMS for a FC-HEV, including four FC stacks and a battery pack. The article [41] introduced a novel approach for EMS of aircraft that integrated system cost considerations into the ECMS, utilizing a sequential quadratic programming algorithm. This approach aimed to enhance MFCS efficiency, cut overall system costs, mitigate power fluctuations in the FC system, and safeguard underperforming stacks, thereby extending the system's lifespan. [42] presented an online extremum-seeking EMS for a FC/supercapacitor hybrid electric tram. The strategy aimed to

identify the FC's optimal efficiency and power points. Results indicated substantial hydrogen consumption savings of 43.92% and 23.49%, along with improved stack efficiency of 2.61% and 17.31%, respectively, when compared to the state machine control strategy and the ECMS. In [43], a decentralized EMS based on model predictive control (MPC) was proposed for a modular FC powertrain to minimize the cumulative operational cost of the system. However, the online optimization techniques discussed above focus on a localized domain because they optimize for individual time steps. As a result, the effectiveness of these strategies in finding optimal solution is still open to discussion. Dynamic programming (DP) stands out as the most potent optimization method when it comes to creating a global EMS. Compared to Pontryagin's Minimum Principle method, DP provides better flexibility in terms of the nature of constraints, and the feasibility of obtaining and implementing the solution. There are many papers in the energy management of systems including single-stack FC in which DP was used to reach the optimal solution. For instance, the authors of [44] introduced an innovative EMS for a FC hybrid bus, combining DP and fuzzy logic. The results demonstrated significant optimization advantages, especially in scenarios with high energy demands and low initial State of Charge (SOC). This approach led to an impressive 8.97% improvement in fuel economy. Ref. [45] introduced an EMS for a FC hybrid tramway, which combined DP and a state machine approach to optimize power distribution between the FC and supercapacitor while considering FC durability and hydrogen consumption. A cost-minimization strategy that encompassed both fuel consumption and the degradation of FC in a tram was introduced in [46]. The article presented a computationally efficient multidimensional DP approach to find the optimal control trajectory of the problem. The proposed strategy decreased FC degradation by a minimum of one-third, leading to an overall reduction in composite

operating costs of at least 8.66% when compared to conventional approaches. However, the challenge of the DP is dimension disaster, especially when the number of control variables increases. Hence, there are not several papers in multi-stack FCSs area using DP as their EMS. The authors of [47, 48] conducted a comparison of their proposed method against DP as a benchmark for validation. However, it is important to note that the DP approach employed in these studies evenly distributed power across all stacks. As an illustration, even in situations where a single FC stack could adequately meet low power demands, all the stacks were actively involved. This applies more degradation to FC stacks and increases the operation cost of the system. Another point in all the mentioned DP methods is that they were not health-aware EMSs. These DPs were not aware of actual health state of FC stacks.

The number of articles using intelligent-based EMSs in MFCS, is limited. In [47], a three-layer EMS was introduced by the authors, integrating Q-learning, a model-free reinforcement learning algorithm. This EMS aims to fulfill power demands while simultaneously reducing expenses associated with hydrogen consumption and degradation across all power sources. Ref. [49] suggests an EMS utilizing Independent Q-learning, a multi-agent reinforcement learning algorithm. Its objective is to regulate battery SOC and reduce hydrogen consumption. Despite its advantages, such as being model-free, this type of energy management has not yet reached maturity.

Based on the literature, a lack of awareness regarding health adaptation can lead to a hydrogen consumption increase ranging from approximately 6.5% to 24% in different EMSs [78]. To the best of our knowledge, there is no prior work in the literature that proposes an optimal EMS for a hybrid multi-stack FC system. Hence, this paper puts forward an offline optimal EMS based on constrained exploration method (CEM) to

minimize the operational costs, including hydrogen consumption and FC stack degradation, in HDVs. Furthermore, the proposed CEM takes into account the health condition of FC stacks when bringing them into service during the operation of the system. As previously mentioned, with the increase in the number of variables, such as the output power of FC stacks in this study, DP faces a 'dimensionality disaster,' making it a time-consuming methodology. It is possible to mitigate the time issue by reducing the number of grid points in DP [79]. However, excessive reduction may lead to interpolation issues and decrease the accuracy of the solution. In this paper, the time-related challenge is addressed by implementing various filters, including battery power, SOC range, and SOC filters, within the search space. These filters are applied to exclude infeasible areas during the search process. Also, DP encounters scalability issues and becomes ineffective as the number of FC stacks increases, due to the heightened complexity in managing control and state variables. The CEM serves as a scalable, health-conscious, and time-efficient benchmark EMS for hybrid MFCSs. Its scalability and time efficiency are achieved through the use of different filters to manage the large number of control and state variables as the number of stacks increases. It is health-conscious by considering the health status of each FC stack in the multi-objective objective function. This approach efficiently decreases operational expenses and significantly shortens simulation time compared to conventional benchmark techniques. In light of the above-discussed points, the contributions of this work are as follows:

- A CEM is developed for obtaining the optimal power distribution in HDVs with multiple FC stacks. In contrast to other approaches, the method proposed here is scalable and can be applied to various heavy-duty applications.

- The proposed CEM considers the health condition of FC stacks during the operation.
- Different filters have been designed to make the proposed CEM a more time-efficient methodology.

The organization of the remainder of the paper is as follows: Section 2 discusses the model description, Section 3 presents the proposed EMS, Section 4 provides the results of the simulation, and Section 5 encapsulates the conclusions drawn from the research.

2.3 Modeling

In this section, the configuration of the vehicle powertrain, FC and battery models, is described in detail.

2.3.1 Powertrain Configuration

In this paper, a parallel structure is selected to study because this architectural design offers redundancy and facilitates independent control over each stack. Additionally, this design allows the system to work in a degraded despite the failure of one or some stacks. The importance of redundancy and the ability to operate in a faulty scenario is particularly notable in aircraft-related applications. This structure is based on a semi-active principle, wherein FC stacks are connected to the DC bus using unidirectional DC-DC converters, while the battery pack, as an ESS, is directly linked to the bus [80, 81]. The configuration of a parallel multi-stack FC system is shown in Fig. 2-1. The number of stacks could change in different applications.

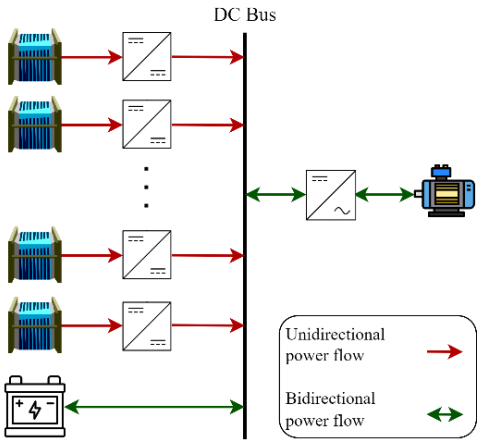

Fig. 2-1. The structure of hybrid multi-stack powertrain.

The power balance of the powertrain system can be demonstrated as (2-1) in which the power generation and consumption should be equal:

$$\frac{P_{Req}}{\eta_{DC-AC}} + P_{Aux} = \eta_{DC-DC} \sum_{i=1}^{M} P_{FC,i} + P_{bat} \tag{2-1}$$

where P_{Req}, P_{Aux}, $P_{FC,i}$ and P_{bat} are the required power of load, power of FC system auxiliary devices, generated power by the i-th stack of FC and battery power, respectively. Also, η_{DC-AC} and η_{DC-DC} indicate the efficiency of DC-AC inverter and DC-DC converter. Index M is the number of FC stacks.

2.3.2 Fuel Cell Model

A semi-empirical model was introduced in [76] that has been successfully employed in multiple publications to describe the performance of the FC stack using experimental data. Based on this model, the output circuit voltage of each cell (V_C) can be calculated as:

$$V_C = E_{Nernst} + V_{act} + V_{ohmic} + V_{con} \tag{2-2}$$

Where E_{Nernst} is the reversible potential of the cell (V), V_{act} is the activation voltage loss (V), V_{ohmic} is the ohmic voltage loss and V_{con} is the voltage loss due to concentration (V). The E_{Nernst} is defined as follows:

$$E_{Nernst} = 1.229 - 0.85 \times 10^{-3}(T_{FC} - 298.15) + 4.3085 \times 10^{-5} T_{FC}\left[\ln\left(P_{H_2}\right) + 0.5 \ln\left(P_{O_2}\right)\right] \quad (2\text{-}3)$$

where T_{FC}, P_{H_2}, P_{O_2} are the temperature of the stack (K), partial pressure of the hydrogen in the anode ($N\ m^{-2}$) and partial pressure of the oxygen in the cathode ($N\ m^{-2}$), respectively. The amount of V_{act} is obtained by (2-4) and (2-5):

$$V_{act} = \xi_1 + \xi_2 T_{FC} + \xi_3 T_{FC} ln\left(C_{O_2}\right) + \xi_4 T_{FC} \ln(I_{FC}) \quad (2\text{-}4)$$

$$C_{O2} = \frac{P_{O2}}{5.08 \times 10^6 \exp(-498/T_{FC})} \quad (2\text{-}5)$$

where ξ_n $(n = 1,2,3,4)$ are empirical parameters, C_{O_2} is the concentration of the oxygen ($mol\ cm^{-3}$), and I_{FC} is the FC current (A). V_{ohmic} is calculated as:

$$V_{ohmic} = -I_{FC} R_{internal} = -I_{FC}(\zeta_1 + \zeta_2 T_{FC} + \zeta_3 I_{FC}) \quad (2\text{-}6)$$

where $R_{internal}$ is the internal resistance of the FC, and $\zeta_n (n = 1,2,3)$ are empirical values. V_{con} can be obtained by:

$$V_{con} = B ln\left(1 - \frac{J_{FC}}{J_{max}}\right) \quad (2\text{-}7)$$

where B is an empirical parameter, J_{FC} is the actual current density of the FC ($A\ cm^{-2}$), and J_{max} is the maximum current density ($A\ cm^{-2}$).

The hydrogen consumption of the FC stack is calculated by (2-8), which is suggested in [82]:

$$\dot{m}_{H_2} = 1.05 \times 10^{-8} \frac{P_{FC}}{V_C} \tag{2-8}$$

where $\dot{m}_{H_2}$ is the hydrogen flow ($kg\ s^{-1}$), and P_{FC} is the power of FC stack (W).

Various operational conditions, such as start-stop procedures, idling current levels, and the rate at which loads change, can change the FC lifespan. According to [82], PEMFC performance can be significantly impacted by the deterioration of the membrane electrode assembly (MEA). This MEA degradation primarily stems from three key factors: gas diffusion layer, membrane layer and catalyst layer degradations. In summary, the primary factors responsible for the performance decline of PEMFC are associated with four operating conditions: start-stop cycling, transient loading, high loading, and low loading. The degradation of the FC is described as the voltage drop in the rated power. In this paper, it is considered that if the voltage reaches to 90% of its rated value, the FC has reached its end of life. The percentage of the degradation is obtained as follows [83]:

$$Deg_{FC} = \left(k_s n_s + k_f n_f + k_l t_l + k_h t_h + k_n t_n\right) \tag{2-9}$$

where k_s is the coefficient of start-stop number, k_f is the coefficient of fast-dynamic loads (power changes more than 30% of FC rated power), k_l is the coefficient of low-power loads (power less than 5% of FC rated power), k_h is the coefficient of high-power loads (power more than 90% of FC rated power) and k_n is the coefficient of natural decay (the time that FC is in service). The value of these parameters can be found in Table 2-1. The parameters k_s, k_f, k_l and k_h are based on the experimental results of [84]. The parameter

k_n is calculated considering a 5,000-hour operational goal and a 10% allowable voltage drop for the FC stacks. Also, n_s, n_f, t_l, t_h and t_n denote the start-stop number, fast-dynamic change number, operation time of low-power loads (s), operation time of high-power loads (s) and operation time of normal loads (s).

Table 2-1. Coefficients related to FC degradation.

Coefficient	Value
k_s	0.00196 (% $cycle^{-1}$)
k_f	0.0000593 (% $cycle^{-1}$)
k_l	0.00126 (% h^{-1})
k_h	0.00147 (% h^{-1})
k_n	0.02 (% h^{-1})

It should be noted that the goal of this work is not to present the most accurate degradation model; any other degradation model can be substituted for the current one. The primary aim of this study is to demonstrate the proposed method's ability to identify the health condition of FC stacks and distribute power among them in a manner that minimizes the degradation cost for the FCS.

2.3.3 Battery Model

This paper utilizes a lithium-ion battery as an energy storage system (ESS) to handle peak-load demands and capture energy during braking. To model the battery, an internal resistance-based approach is employed. The battery model's equivalent circuit is presented in Fig. 2-2.

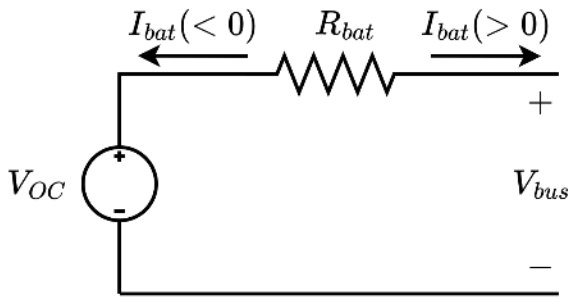

Fig. 2-2. The equivalent circuit of battery model.

It is essential to note that when the battery discharges, the battery current (I_{bat}) is positive, while during charging, it is negative. Equations (2-10) to (2-13) provide insights into the battery's behavior [48]:

$$V_{bus}(t) = V_{OC}(t) - I_b(t)R_b(t) \tag{2-10}$$

$$P_{bat}(t) = V_{bus}(t)I_{bat}(t) \tag{2-11}$$

$$I_{bat}(t) = \frac{V_{OC}(t) - \sqrt{V_{OC}(t)^2 - 4R_{bat}(t)P_{bat}(t)}}{2R_{bat}(t)} \tag{2-12}$$

$$SOC(t) = SOC(t_0) - \eta_{bat}\frac{\int_{t_0}^{t} I_{bat}\, dt}{Q_{bat}} \tag{2-13}$$

where V_{OC}, R_{bat}, P_{bat}, η_{bat}, Q_{bat} are the open-circuit voltage (V), internal resistance (Ω), output power (W), Coulomb efficiency and the capacity of the battery ($A\,h$), respectively. Also, V_{bus} is the voltage of the DC bus (V). It should be noted that η_{bat} is assumed to be 1 for battery discharge and 0.98 for battery charging.

2.4 EMS Design Based on CEM

In this section, the EMS which is developed based on CEM is described. Fig. 2-3 shows the steps of the CEM-based EMS including initialization, forward calculation, and backward calculation.

In the initialization step, the input data, including the required power and vehicle specifications, are provided to the algorithm. Subsequently, the range of generated battery power is calculated based on the battery power filter. Then, the reachable range of SOC by the battery is obtained using the SOC-range filter. At the end of this step, the system status at the initial state ($k = 0$) is given to the algorithm.

During the forward calculation step, initially, grids for state and control variables are created, considering various constraints on the powers of the FC stacks, power change rates of FC stacks, accessible SOC, and battery power. Thereafter, the objective function is computed to transition these grids from the previous stage. Subsequently, the SOC filter is applied to the grids using the calculated objective function to reduce the number of possibilities.

Following this, if the algorithm is in the terminal stage, the process of extracting the optimal trajectory will commence; otherwise, the forward calculation for the next stage will be continued.

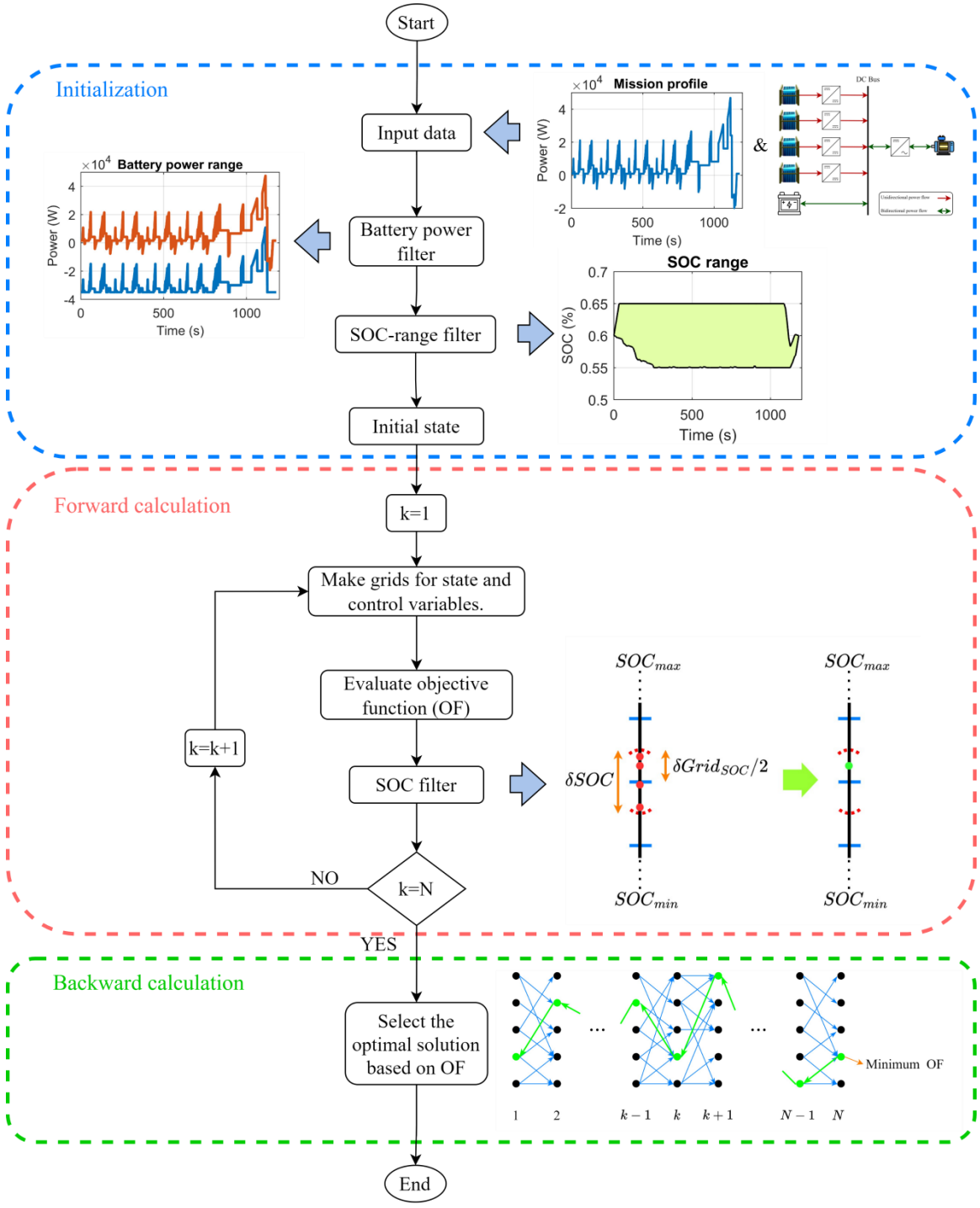

Fig. 2-3. The scheme of CEM-based EMS.

The process of solving a multistage problem is divided into four parts: stage partition, establishment of state variable and control variable, definition of transition cost equations,

and applying the constraints of the problem, which will be discussed in the following subsections.

2.4.1 State Space Model of CEM

In this section, the equations of the state space, objective function and constraints required to build CEM are brought.

2.4.1.1 State space equation

In this paper, the interval of stages is assumed one second. Hence, the number of stages equals to the number of seconds of the mission profile ($k\epsilon[1,n]$). In most of FC-HEVs in which the CEM was used as an EMS, only the SOC of the battery was considered as a state variable. In these articles, the output power of the FC was defined as only a control variable and was not considered as a state variable to prevent the dimension disaster of the solving process. This leads to frequent start-stops of FC and its degradation. Moreover, the change rate of the FC power is not satisfied in this situation. The state variables of the proposed EMS are as (2-14):

$$X(k) = [x_1(k), \dots, x_M(k), x_{M+1}(k)]^T = [P_{FC,1}(k), \dots, P_{FC,M}(k), SOC(k)]^T \qquad (2\text{-}14)$$

where $P_{FC,i}$ is the output power of the i-th FC stack, M is the number of FC stacks and the SOC is the state of the charge of the battery. Hence, the number of the state variables is $M+1$.

The command for the output powers of the FC stacks is considered the control variable, which is shown by (2-15):

$$U(k) = [u_1(k), \dots, u_M(k)]^T \quad (2\text{-}15)$$

The transition equation of the output power of the *i*-th FC stack as the state variable is shown in (2-16) .

$$x_i(k+1) = u_i(k) \quad ; \quad i = (1, \dots, M) \quad (2\text{-}16)$$

Considering (2-14) - (2-16), control variables can be stated as (2-17):

$$U(k) = [u_1(k), \dots, u_M(k)]^T = [P_{FC,1}(k+1), \dots, P_{FC,M}(k+1)]^T \quad (2\text{-}17)$$

In fact, the power generated by the *i*-th stack in the next stage is equal to the command given in the current stage. By defining the state and control variables in this way, the decision making in each stage (k-th stage) only depends on the state and control variables of that stage and there is no relationship with the previous stage ($(k-1)$-th stage) variables, which reduces the computer memory capacity required. The change rate of *i*-th FC stack power ($\Delta u_{FC,i}(k)$) can be expressed as (2-18).

$$\Delta u_i(k) = u_i(k) - u_i(k-1) \quad ; \quad i = (1, \dots, M) \quad (2\text{-}18)$$

Considering (2-16), (2-18) can be written as (2-19):

$$\Delta u_i(k) = u_i(k) - x_i(k) \quad ; \quad i = (1, \dots, M) \quad (2\text{-}19)$$

The transition equation of the x_{M+1} (SOC of the battery) can be achieved by (2-12) and (2-13) as following:

$$
\begin{aligned}
x_{M+1}(k+1) &= x_{M+1}(k) - \eta_{bat}\frac{I(k)\Delta T}{Q_{bat}} \\
&= x_{M+1}(k) \\
&\quad - \eta_{bat}\frac{\frac{V_{OC}(k) - \sqrt{V_{OC}(k)^2 - 4R_{bat}(k)P_{bat}(k))}}{2R_{bat}(k)}\Delta T}{Q_{bat}}
\end{aligned}
\tag{2-20}
$$

where ΔT is the time step of the problem (s).

After selecting the state and control variables, the algorithm will aim to find the optimal solution, determined by the minimum value of the objective function.

By considering the feature mentioned in (2-16), the CEM has more computational efficiency compared to conventional benchmark algorithms such as level-set DP. In level-set DP, for an FCS including *M* stacks, there are M control variables and M state variables, which are related to the power of FC stacks. Another state variable is the SOC of the battery. Hence, if each variable has G grids, the level of discretization of level-set DP will be G^{2M+1}. In the CEM, for M stacks, there will be M control variables for the power of FC stacks. Based on (2-16), state variables for FC stacks in each stage correspond to the control variables in the previous stage. Hence, the CEM does not need to define new state variables and can use the control variables of the previous stages as the current state variables. Based on these explanations, the level of discretization for G grids of variables will be G^{M+1} in CEM. This makes CEM faster than level-set DP in solving the problem. Also, this type of state space definition makes the CEM a scalable benchmark approach. For systems with more FC stacks, when the number of state and control variables increases, level-set DP is unable to solve the problem, whereas the CEM can perform energy

management for these types of systems because of the tremendous reduction of variables and discretization level. This matter will be shown in the case study 3 in the results section.

2.4.1.2 Objective function

The recent trend in PEMFC system development has moved from LDVs to HDVs, which demand higher system availability and longer lifespans. This shift also leads to increased power demand and hydrogen consumption, transitioning the focus from capital expenditures (CapEx) to operational expenditures (OpEx). To lower OpEx, it is crucial to reduce hydrogen consumption and degradation costs [85]. As a result, both industry and academia are increasingly focusing on multi-objective functions that consider these factors for FC-HEVs. In this work, the operational cost including the hydrogen consumption and degradation costs, has been selected as the objective function. However, it should be noted that the proposed EMS based on CEM is not only limited to this kind of cost function and could be used for solving other cost functions depending on the need of the project. The proposed method is based on the principle of optimality, similar to DP, and is not sensitive to the choice of the cost function. The objective function considered for this paper contains two main terms. The first term is related to the cost of consumed hydrogen as the fuel. The second one contains the cost of degradation of the FC stacks. The objective function can be seen in (2-21) to (2-24):

$$J = \sum_{k=0}^{N} (\omega_{H_2} C_{H_2}(k) + \omega_{Deg} C_{Deg}(k)) \tag{2-21}$$

$$C_{H_2}(k) = \sum_{i=1}^{M} c_{H_2} \dot{m}_{H_2,i}(k) \quad ; \quad \forall k \tag{2-22}$$

$$C_{Deg}(k) = \frac{1}{Deg_{allowed}} \sum_{i=1}^{M} (c_{FC} P_{FC,i,\max}) \left(\frac{1}{SOH_i(k)}\right) (k_s n_{s,i}(k) + k_f n_{f,i}(k) + k_l t_{l,i}(k) + k_h t_{h,i}(k) + k_n t_{n,i}(k)) \quad ; \quad \forall k \tag{2-23}$$

$$SOH_i(k) = 1 - \sum_{p=1}^{k-1} Deg_i(p) \quad ; \quad \forall k \tag{2-24}$$

Equation (2-21) represents the objective function of the energy management problem discussed in this paper. This function is a weighted sum of the hydrogen cost and the degradation cost of the fuel cell (FC) stacks over a mission profile consisting of *N* stages. The cost of the consumed hydrogen for the FCS in the *k*-th stage ($C_{H_2}(k)$) is given by (2-22). This cost is the sum of the product of the hydrogen price ($c_{H_2} = 4\$\, kg^{-1}$) and the hydrogen flow rate for each FC stack ($\dot{m}_{H_2,i}$), across all *M* stacks. In (2-23), $C_{Deg}(k)$ denotes the degradation cost of the FC stacks at the *k*-th stage. The price of the *i*-th FC stack can be obtained by the product of the cost per kilowatt (kW) of the FC stack ($c_{FC} = 93\ \$\ kW^{-1}$ [86]) and the rated power of the *i*-th stack ($P_{FC,i,\max}$). In the objective function, $C_{H_2}(k)$ and $C_{Deg}(k)$ are converted to monetary values based on established references such as [86], ensuring a standardized approach devoid of personal bias. Given that hydrogen consumption and the degradation of fuel cell stacks are equally prioritized in this study, equal weights of one have been assigned to both components ($\omega_{H_2} = \omega_{Deg} = 1$). This choice reflects their equal importance in minimizing the overall operational cost. However, these weights are adjustable and can be modified in other studies to reflect different priorities. The parameter $Deg_{allowed}$ represents the maximum allowable percentage of degradation for FC stacks to remain operational. If degradation exceeds this threshold, the FC stack is considered to be out of service. $SOH_i(k)$ used in (2-23) is the state of health

(SOH) of *i*-th FC stack before the start of the *k*-th stage, which can be calculated as (2-24). Hence, by considering $\frac{1}{SOH_i(k)}$ as a weight in (2-23), the algorithm will be aware of the SOH of the stacks during the operation time. This weight applies a higher cost to the objective function if the FC stacks with more degradation are used. $n_{s,i}$, $n_{f,i}$, $t_{l,i}$, $t_{h,i}$ and $t_{n,i}$ are the concepts introduced in (2-9), and subscript *i* refers to the *i*-th FC stack.

2.4.1.3 Constraints

To solve the energy management problem, some constraints should be considered for state and control variables. These constraints can be found in (2-25) to (2-29) [48]:

$$SOC_{min} \leq SOC(k) \leq SOC_{max} \quad ; \quad \forall k \tag{2-25}$$

$$P_{bat,min} \leq P_{bat}(k) \leq P_{bat,max} \quad ; \quad \forall k \tag{2-26}$$

$$P_{FC,i,min} \leq P_{FC,i}(k) \leq P_{FC,i,max} \quad ; \quad \forall k \tag{2-27}$$

$$P_{FC,i,min} \leq u_{FC,i}(k) \leq P_{FC,i,max} \quad ; \quad \forall k \tag{2-28}$$

$$\Delta P_{FC,i,min} \leq u_{FC,i}(k+1) - u_{FC,i}(k) \leq \Delta P_{FC,i,max} \quad ; \quad \forall k \tag{2-29}$$

where the subscripts min and max stand for the minimum and maximum allowable values for each state and control variables. It is worth mentioning that (2-29) limits the change rate of the output power of the *i*-th FC stack.

2.4.2 Steps of the CEM

Based on Fig. 2-3, the CEM consists of three main steps: initialization, forward calculation, and backward calculation. These steps are explained in the following sections.

2.4.2.1 Initialization

At the beginning of this step, the algorithm receives the required power of the load and the FCS data including the FC stacks, battery and auxiliary system data. Typically, many invalid grid points exist in the state grid due to the specifications of the FCS. To address this, a boundary range for the state variables is specified in advance using the battery power filter and SOC-range filter. By applying these filters at the beginning of the algorithm, infeasible solutions that conflict with the specifics of the FCS are eliminated from the search space, thereby accelerating the CEM process.

It should be emphasized that the acceleration achieved by the proposed CEM does not arise from simplifying the physical models or relaxing the operational constraints. Instead, it results from a structured reduction of the search space by excluding infeasible, unreachable, or redundant states through the battery-power, SOC-range, and SOC-interpolation filters. Therefore, the computational gain is obtained while preserving the formulation of the optimization problem and its physical consistency.

2.4.2.1.1 Battery power filter

This filter is designed based on the power balance equation. Considering (2-1), the power of the battery is obtained by (2-30):

$$P_{bat} = \frac{P_{Req}}{\eta_{DC-AC}} + P_{Aux} - \eta_{DC-DC} \sum_{i=1}^{M} P_{FC,i} \tag{2-30}$$

Since P_{Aux} is the power consumed by the auxiliary devices of the FC system and a portion of the generated power by the FC stacks, it can be written as $\sum_{i=1}^{M} \alpha_i P_{FC,i}$ in which α_i is less than 1. Hence, (2-30) can be transformed to (2-31):

$$P_{bat} = \frac{P_{Req}}{\eta_{DC-AC}} - \eta_{DC-DC} \sum_{i=1}^{M} P_{FC,i}(1 - \frac{\alpha_i}{\eta_{DC-DC}}) \quad (2\text{-}31)$$

At each stage (time), the value of P_{Req} is known. Therefore, the minimum power of the battery (the maximum power by which the battery is charged) will be attained when the net power of the FC system reaches its maximum value. On the contrary, the maximum power of the battery (the maximum power by which the battery is discharged) is obtained when the net power of the FC system is the minimum one. By calculating the lowest and highest power levels of the battery for each stage, the range of battery power provided in the datasheet can be narrowed down, and the calculation time of solving the problem will decrease. Based on these explanations, the minimum and maximum power of the battery in the presence of the FC stacks after applying battery power filter is obtained as (2-32) and (2-33):

$$\hat{P}_{bat,max} = \min \{P_{bat,max}, \frac{P_{Req}}{\eta_{DC-AC}} - \eta_{DC-DC} \sum_{i=1}^{M} P_{FC,i,min}(1 - \frac{\alpha_i}{\eta_{DC-DC}}) \quad (2\text{-}32)$$

$$\hat{P}_{bat,min} = \max \{P_{bat,min}, \frac{P_{Req}}{\eta_{DC-AC}} - \eta_{DC-DC} \sum_{i=1}^{M} P_{FC,i,max}(1 - \frac{\alpha_i}{\eta_{DC-DC}}) \quad (2\text{-}33)$$

2.4.2.1.2 SOC-range filter

In theory, the battery SOC should ideally spread equally between its highest and lowest values within a selected discrete interval. However, due to limited power (which is calculated in the battery power filter) and short sampling times, the SOC does not always vary significantly enough to consistently reach the boundary values. Considering a certain

initial SOC, the subsequent SOC can only cover a narrow spectrum in the next stage. As a result, it is unnecessary for the discretization of SOCs to always include the entire range between $[SOC_{min}, SOC_{max}]$. Over time, however, the range of attainable SOC gradually changes until it eventually meets a specified boundary value.

Furthermore, as the initial and final SOC values must be equal, this information can be utilized in the backward calculation to determine the achievable SOC levels. The final reachable area by SOC (green area in Fig. 2-4) will be the common area of forward and backward ones. In Fig. 2-4, $\delta SOC_{f,max}(k)$ is the maximum variation of the SOC which is calculated at stage k for the next stage in the forward direction, and SOC_{opt} is the optimal path of SOC in the operation period.

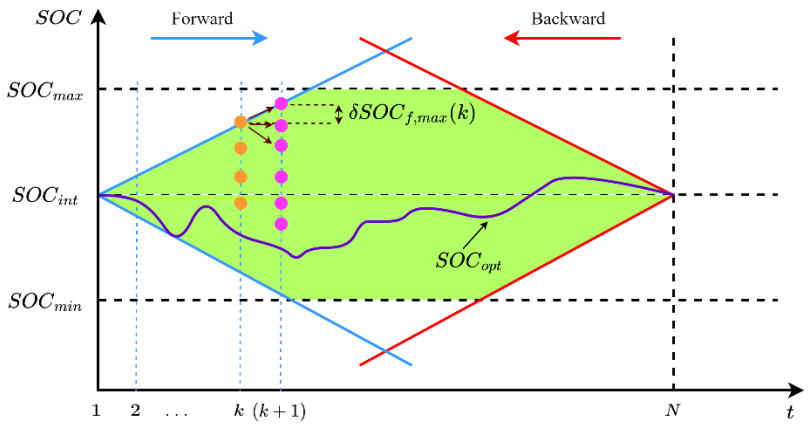

Fig. 2-4. SOC-range filter concept.

Taking (2-20) into account, the upper bound of SOC, denoted as $SOC_{up}(k)$, is determined by substituting $\hat{P}_{bat,min}$ and $\hat{P}_{bat,max}$ for P_{bat} in the forward and backward calculations, respectively. $SOC_{up}(k)$ is obtained by (2-34) - (2-36) [46]:

$$SOC_{up}(k) = \min\{SOC_{f,max}(k), SOC_{b,max}(k)\} \tag{2-34}$$

$$SOC_{f,max}(k) = \left(SOC_{f,max}(k-1) - \eta_{bat}\frac{I(k-1)\Delta T}{Q_{bat}}\right) \quad (2\text{-}35)$$

$$SOC_{b,max}(k) = \left(SOC_{b,max}(k+1) - \eta_{bat}\frac{I(k+1)\Delta T}{Q_{bat}}\right) \quad (2\text{-}36)$$

where $SOC_{f,max}(k)$ and $SOC_{b,max}(k)$ are the maximum SOC levels at stage k in forward and backward calculations, respectively.

Similar to $SOC_{up}(k)$, the lower bound of SOC ($SOC_{lo}(k)$) can be achieved by using $\hat{P}_{bat,min}$ and $\hat{P}_{bat,max}$ instead of P_{bat} in the forward and backward calculations, respectively.

$$SOC_{lo}(k) = \max\{SOC_{f,min}(k), SOC_{b,min}(k)\} \quad (2\text{-}37)$$

$$SOC_{f,min}(k) = \left(SOC_{f,min}(k-1) - \eta_{bat}\frac{I(k-1)\Delta T}{Q_{bat}}\right) \quad (2\text{-}38)$$

$$SOC_{b,min}(k) = \left(SOC_{b,min}(k+1) - \eta_{bat}\frac{I(k+1)\Delta T}{Q_{bat}}\right) \quad (2\text{-}39)$$

where $SOC_{f,min}(k)$ and $SOC_{b,min}(k)$ are the minimum SOC levels at stage k in the forward and backward calculations, respectively.

2.4.2.2 Forward calculation

In the backward calculation of DP, interpolation is necessary when the state variable values do not match the grid points. To avoid the need for interpolation, the forward calculation method is chosen in CEM. To address the interpolation leakage issue in CEM,

the SOC filter (used as a state variable filter) is implemented at each stage of the process, which will be illustrated in the following sections.

2.4.2.2.1 Concept of CEM forward calculation

The principle of optimality, central to DP, states that an optimal solution to a problem contains optimal solutions to its sub-problems [87]. When considering the dynamic problem of the requested power for a vehicle, this problem can be divided into several sub-problems. In this work, each sub-problem is considered over a one-second interval. In the forward calculation of the CEM, which is inspired by the principle outlined in the DP backward calculation [88], the final optimal index J_N^* is defined as shown in (2-40).

$$J_N^* = \min\left(J_{N,1}^*, \dots, J_{N,j}^*, \dots J_{N,P}^*\right) \tag{2-40}$$

where $J_{N,j}^*$ denotes the optimal index corresponding to the *j*-th value of the state variable at the *N*-th step. Clearly, $J_{N,j}^*$ must be determined prior to computing J_N^*. This value can be obtained as (2-41):

$$J_{N,j}^* = \min\left(J_{N,j}\right) = \min\left(J_{N-1,i}^* + T(x_{N-1,i}, x_{N,j})\right) \tag{2-41}$$

where $J_{N-1,i}^*$ is the optimal index related to the *i*-th value of the state variable at the *(N-1)*-th step. $T(x_{N-1,i}, x_{N,j})$ is the cost to go from the *i*-th value of the state variable at the *(N-1)*-th step to *j*-th value of the state variable at the *N*-th step. In the same manner, $J_{N-1,i}^*$ can be obtained as (2-42):

$$J_{N-1,i}^* = \min\left(J_{N-1,i}\right) = \min\left(J_{N-2,p}^* + T(x_{N-2,p}, x_{N-1,i})\right) \tag{2-42}$$

where $J^*_{N-2,p}$ is the optimal index related to the *p*-th value of the state variable at the *(N-2)*-th step. $T(x_{N-2,p}, x_{N-1,i})$ is the cost to go from the *p*-th value of the state variable at the *(N-2)*-th step to *i*-th value of the state variable at the *(N-1)*-th step. If this process continues, the optimal objective function at the first step $J^*_{1,m}$ will be calculated as (2-43):

$$J^*_{1,m} = \min(J_{1,m}) = \min\left(J^*_0 + T(x_0, x_{1,m})\right) = \min\left(J_0 + T(x_0, x_{1,m})\right) \quad (2\text{-}43)$$

where J_0 is the objective function for the initial step. $T(x_0, x_{1,m})$ is the cost to go from the initial step to *m*-th value of the state variable at the first step.

Based on the above explanations, to achieve the optimal solution to the problem, the algorithm should calculate the objective functions in the following order: $J^*_{1,m}, \ldots, J^*_{N-1,i}$, $J^*_{N,j}$.

2.4.2.2.2 SOC filter

During various stages of problem-solving exploration, it may occur that after selecting the control variable values and calculating the corresponding state variables, these calculated values do not align with the predefined grids. This discrepancy is known as the interpolation problem. In the current problem, $P_{FC,i}$ and SOC of the battery are state variables. Since $P_{FC,i}$ in each stage is equal to u_i of the previous stage, there will not be interpolation problem for $P_{FC,i}$. Hence, addressing the interpolation problem solely for the SOC is sufficient.

SOC filter is used to solve this problem. Fig. 2-5 shows the *k*-th stage of exploration assuming three grids for SOC called $SOC_{g-1}(k)$, $SOC_g(k)$ and $SOC_{g+1}(k)$. The red points in Fig. 2-5 (a) represent the calculated SOC values corresponding to different control

variable values. It is observable that no points are allocated for $SOC_g(k)$ and $SOC_{g+1}(k)$. To solve this issue, a range is defined based on the length of the distance between the grid points ($\delta Grid_{SOC}$) and the center of the grid points. All the points that are in this range are called Φ set. For instance, the set related to $SOC_g(k)$ is defined as following [89]:

$$\Phi_g(k) = \left\{SOC(k) \mid SOC_g(k) - \frac{\delta Grid_{SOC}}{2} \leq SOC(k) < SOC_g(k) + \frac{\delta Grid_{SOC}}{2}\right\} \quad (2\text{-}44)$$

From this set, a member that has the minimum objective function is selected to replace the grid points and is used to continue the exploration procedure. These points are shown in green in Fig. 2-5 (b). Using this filter not only solves the interpolation problem but also has the benefit of reducing the number of points. Consequently, this leads to decreased exploration and calculation time.

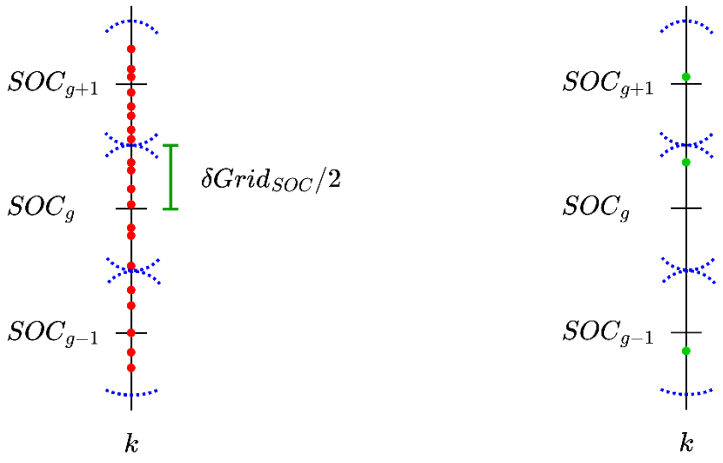

(a) (b)

Fig. 2-5. *K*-th stage of exploration (a) before applying SOC filter (b) after applying SOC filter.

2.4.2.3 Backward calculation

In the backward calculation, the minimum objective function J_N^* is selected as the optimal one and the related variables are stored. The algorithm then steps back to the *(N−1)*-th step, identifying and storing the variables that lead to the previously determined J_N^*. This process repeats for the *(N−2)*-th step, where the algorithm stores the variables that result in the solution at the *(N−1)*-th step, which in turn leads to J_N^*. This iterative procedure continues until the initial step is reached, thereby determining the optimal path. To better understand this procedure, the backward calculation of the Fig. 2-3 can be helpful.

2.5 Results

In this section, the performance of the proposed EMS is validated by simulation. For this purpose, the simulation results for three case studies in heavy-duty transportation section are investigated. The first case study is related to an aircraft equipped with two stacks of FC and a battery. The results of the proposed EMS, which is based on CEM, are compared with those obtained using DP (as a benchmark) and sequential quadratic programming (SQP) (as an online EMS) to validate the accuracy of the proposed approach. The second case study is a tramway containing dual-stack FC and a battery. As for case study 1, the results obtained through CEM are validated through comparison with those yielded by the DP and SQP methods. In the third case study, a truck equipped with four FC stacks and a battery pack is examined. Due to the high number of control and state variables in this scenario, DP is unable to solve the problem. Therefore, the proposed EMS, validated in the first and second case studies, is employed to address this issue, and the results of this application are discussed. The simulations have been executed in MATLAB

R2022b on a system equipped with a twelve-core processor running at 2.4 GHz and supported by 32 GB of RAM.

It should be mentioned that the performance of electrochemical power sources, such as FCs and batteries, is influenced by changes in model parameters due to degradation over time and varying operating conditions including temperature, pressure, and humidity. Degradation is a gradual process, while operating conditions change based on the application. These variations are reflected in the characterization curves of these power sources, such as the polarization curve for FCs and the open circuit voltage vs. SOC and internal resistance vs. SOC for batteries. In this study, characterization curves were derived from manufacturer-provided data and specified operating conditions. The proposed EMS based on CEM approach utilizes these curves to determine the maximum and minimum power values for the FC and the SOC calculations for the battery. If these curves change, they can be easily updated, ensuring the EMS continues to function correctly.

2.5.1 Case study 1

In this case, NASA X-57 Maxwell is selected to investigate the performance of the proposed EMS [90]. The required power of this aircraft, after analyzing 6000 regional flights, is shown in Fig. 2-6:

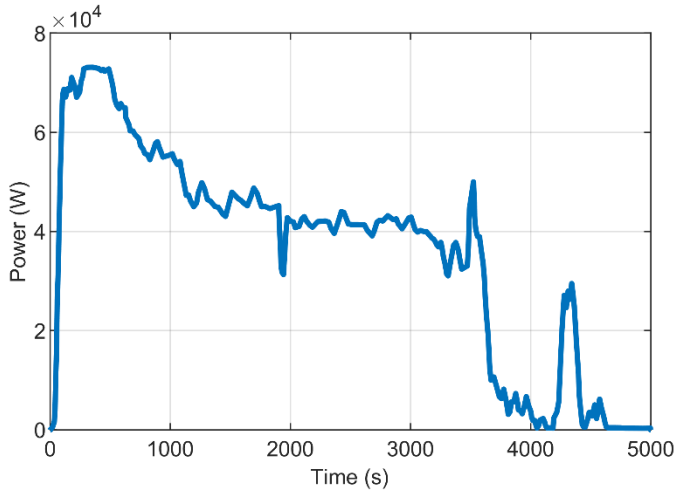

Fig. 2-6. Power demand of NASA X-57 Maxwell aircraft.

To meet this power demand, the aircraft is equipped with two M240 FC stacks manufactured by Axane, each boasting a rated power output of 50 kW. The polarization curve and I-P curve of the FC stack are presented in Fig. 2-7. These curves are obtained under specific conditions: air stoichiometry at 2.5, air relative humidity at 50%, air pressure at 1 barg, a 0.5 barg difference between hydrogen pressure and air pressure, and a temperature of 75 °C [91].

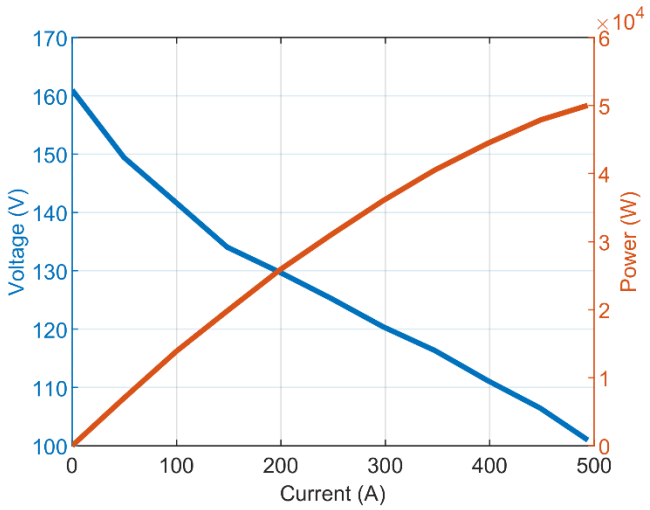

Fig. 2-7. Polarization and I-P curves of M240 FC stacks used in case study 1.

A lithium-ion battery pack is utilized to help the PEMFC stack in providing the required power. The battery specifications are outlined in Table 2-2 [56]. A simulation model utilizing internal resistance is utilized to mimic the behavior of this battery. Fig. 2-8 visually demonstrates the relationship between the battery's SOC, open circuit voltage (V_{OC}), variations in internal resistance during the charging phase ($R_{bat,ch}$), and changes in internal resistance during the discharging phase ($R_{bat,dis}$).

Table 2-2. Battery cell and battery pack specifications used in case study 1.

	Parameter	Symbol	Value
Battery cell	Capacity (Ah)	$Q_{bat,cell}$	41
	Nominal voltage (V)	$V_{OC,cell}$	3.62
	Max. current (A)	$I_{bat,max}$	150
	Min. current (A)	$I_{bat,min}$	-150
Battery pack	Number of cells in series	$n_{bat,s}$	127
	Number of cells in parallel	$n_{bat,p}$	1
	Capacity (kWh)	E_{bat}	18.86
	Initial SOC (%)	SOC_{int}	0.6
	Min. SOC (%)	SOC_{min}	0.5
	Max. SOC (%)	SOC_{max}	0.7

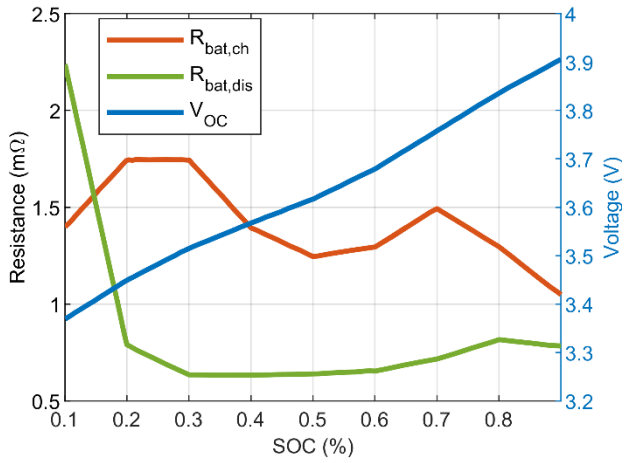

Fig. 2-8. The relationship of SOC with V_{OC} and P_{bat} per cell.

2.5.1.1 Comparison with level-set DP

To validate the proposed EMS based on CEM, its results are compared with those of the level-set DP introduced in [92]. Four simulations, each with different numbers of grid points for control and state variables, are executed using both CEM and level-set DP. In simulations 1 through 4, the number of grid points for FC power (as both state and control variables) is set at 10, 20, 30, and 40, respectively. The conditions and results of these simulations are shown in Table 2-3. Based on this table, it is evident that CEM outperforms the level-set DP method by achieving a solution with a minimized objective function and reduced hydrogen consumption in a shorter simulation time. Furthermore, an evident trend is that as the number of grids increases, there is a reduction in the objective function. However, this comes at the cost of an extended time needed to solve the problem. This illustrates a trade-off between the precision of results and the swiftness of the problem-solving process. Based on the results, the objective function does not have a noticeable reduction after 20 grids (simulation 2) while the simulation time increases significantly. Hence, 20 grids can be a suitable choice in terms of accuracy and speed.

.

Table 2-3. Comparison of conditions and results of level-set DP and CEM in case study 1.

			Level-set DP	**CEM**
Simulation 1	Simulations conditions	SOC grid gap	0.0001	0.0001
		u_i grid gap (W)	5000	5000
		$P_{FC,i}$ grid gap (W)	5000	-
		Discretization level	10^5	10^3
	Simulations results	H_2 consumption (gr)	3396.3	3332.7
		Degradation cost ($)	5.07	4.90
		Simulation time (s)	2898	2109
Simulation 2	Simulations conditions	SOC grid gap	0.0001	0.0001
		u_i grid gap (W)	2500	2500
		$P_{FC,i}$ grid gap (W)	2500	-
		Discretization level	20^5	20^3
	Simulations results	H_2 consumption (gr)	3389.9	3324.7
		Degradation cost ($)	4.47	4.38
		Simulation time (s)	8216	7346
Simulation 3	Simulations conditions	SOC grid gap	0.0001	0.0001
		u_i grid gap (W)	1666.7	1666.7
		$P_{FC,i}$ grid gap (W)	1666.7	-
		Discretization level	30^5	30^3
	Simulations results	H_2 consumption (gr)	3387.3	3325.7
		Degradation cost ($)	4.47	4.37
		Simulation time (s)	52956	14500
Simulation 4	Simulations conditions	SOC grid gap	0.0001	0.0001
		u_i grid gap (W)	1250	1250
		$P_{FC,i}$ grid gap (W)	1250	-
		Discretization level	40^5	40^3
	Simulations results	H_2 consumption (gr)	3383.7	3325.7
		Degradation cost ($)	4.47	4.36
		Simulation time (s)	220210	26667

As the power distributions for FC stacks and the battery in both CEM and level-set DP methods are very similar, this section will only present the distributions obtained by CEM

for Simulation 2. Fig. 2-9 shows the power demand (Fig. 2-9a), FC stacks power (Fig. 2-9b), battery power (Fig. 2-9c), and battery SOC (Fig. 2-9d). According to this figure, the battery effectively supplies and absorbs high-dynamic loads, enabling the smooth operation of the FC stacks. Additionally, the battery is charged beforehand to meet the demand during peak loads at seconds 105, 3515, and 4274.

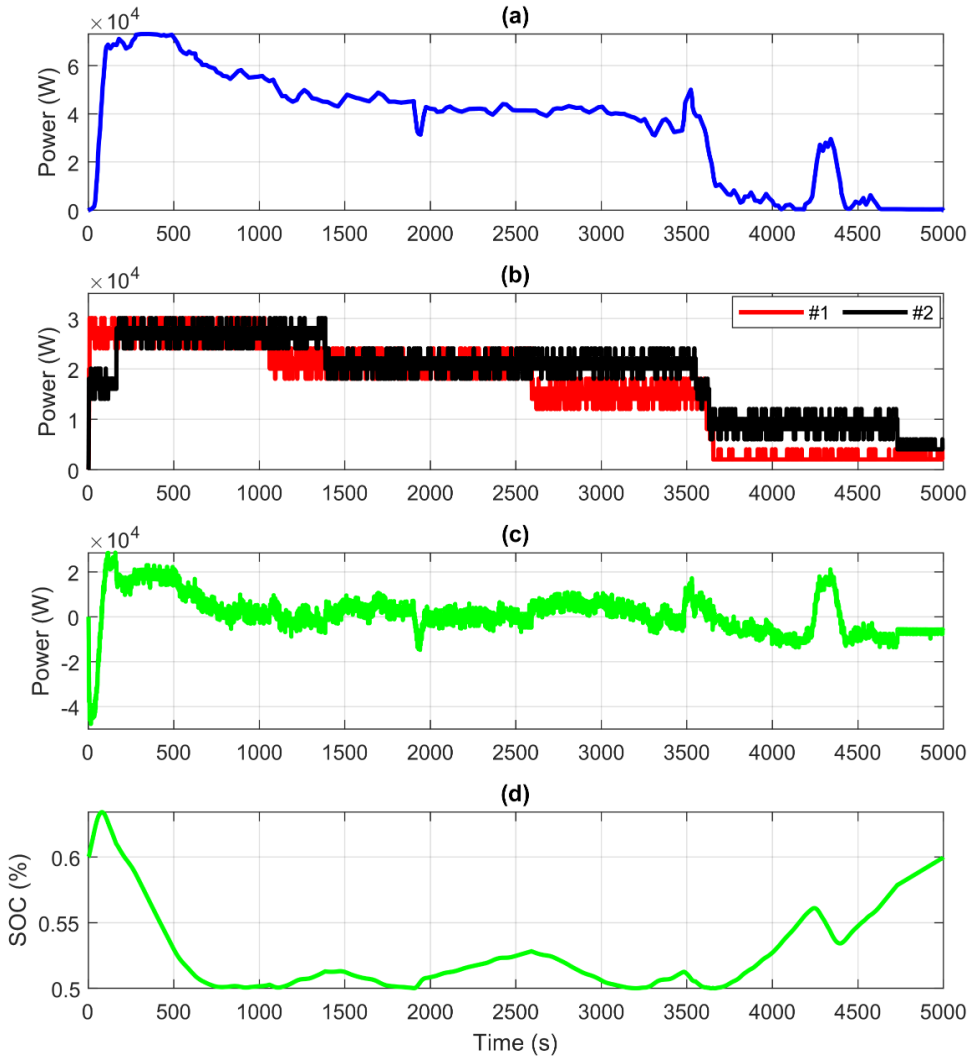

Fig. 2-9. The obtained results in case study 1: a) Power demand, b) FC stacks net power, c) Battery power, and d) Battery SOC.

The distribution of various operational costs of FC stacks including fuel cost and different degradation costs can be found in Fig. 2-10. For each FC stack, the chart on the

left (larger circle) displays the total operating cost, while the chart on the right (smaller circle) illustrates the breakdown of the degradation cost. According to this figure, it is apparent that the operational cost of stack 2 exceeds that of stack 1 due to its higher power generation, as indicated in Fig. 2-9. Also, it can be seen that the degradation costs of stacks are equal.

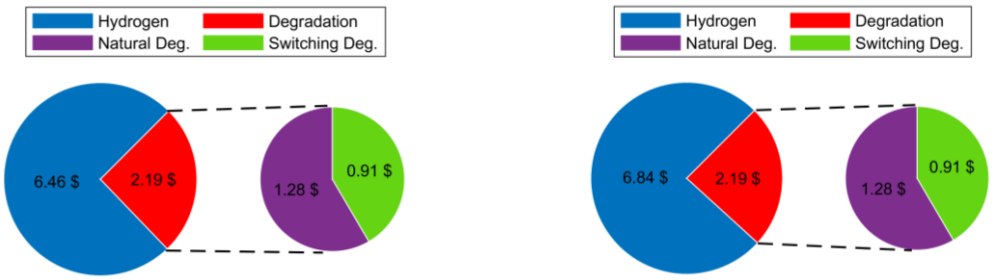

(a) (b)

Fig. 2-10. Operational cost distribution in case study 1: (a) FC stack 1, (b) FC stack 2.

2.5.1.2 Comparison with SQP

In this section, the results obtained by CEM with 20 grids for state and control variables (simulation 2), which was selected in the previous comparison considering accuracy and speed, are compared to the results achieved by the SQP method. Table 2-4 shows the results of case study 1 obtained by the CEM and SQP methods.

Table 2-4. Comparison of the results of SQP and CEM methods in case study 1.

	SQP	**CEM**
H_2 consumption (gr)	3863.1	3324.7
Degradation cost ($)	5.25	4.38
Simulation time (s)	15	7346

According to the above table, using the CEM method reduces hydrogen consumption by 13.9% compared to the SQP method. Additionally, the degradation cost of the CEM method is 16.6% less than that of the SQP method in case study 1. Considering the price of

H2 at 0.004 $/gr, the operational expenses for SQP and CEM stand at $20.70 and $17.68, respectively. Consequently, employing CEM reduces the operational cost by roughly 14.6%. Given that SQP is an online EMS and CEM is an offline one, it is reasonable that the simulation time of the SQP method is significantly less than that of the CEM method.

2.5.2 Case study 2

The second case study involves an FC-battery-powered hybrid system for the Metro-Centro tramway (400 kW) in Seville, Spain. The requested power of this vehicle can be seen in Fig. 2-12a [93].

The FCS includes two commercial FC stacks from PowerCell Group. Each stack generates a nominal power of 125 kW [94]. The polarization curve and the I-P curve of this type of FC stack are shown in Fig. 2-11.

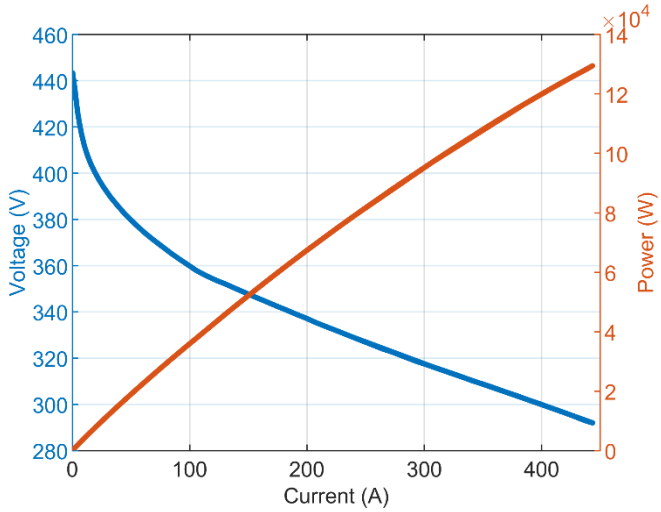

Fig. 2-11. Polarization and I-P curves of FC stacks used in case study 2.

The tramway hybrid system discussed in this case study features a Ni-MH battery. Its characteristic parameters, listed in Table 2-5, are taken from a commercial battery module,

Saft's NHP 10-34 model. This battery is produced for high-power applications, such as hybrid tramways [95].

Table 2-5. Battery cell and battery pack specifications used in case study 2.

	Parameter	Symbol	Value
Battery cell	Capacity (Ah)	$Q_{bat,cell}$	34
	Nominal voltage (V)	$V_{OC,cell}$	12
	Max. current (A)	$I_{bat,max}$	750
	Min. current (A)	$I_{bat,min}$	-750
Battery pack	Number of cells in series	$n_{bat,s}$	58
	Number of cells in parallel	$n_{bat,p}$	1
	Capacity (kWh)	E_{bat}	23.66
	Initial SOC (%)	SOC_{int}	0.6
	Min. SOC (%)	SOC_{min}	0.5
	Max. SOC (%)	SOC_{max}	0.7

2.5.2.1 Comparison with level-set DP

In this case study, similar to case study 1, the proposed EMS is validated by comparing its results with those obtained from the level-set DP. Four simulations are conducted, each varying the number of grid points for control and state variables, using both CEM and level-set DP. In simulations 1 through 4, the number of grid points for FC power was set at 10, 20, 30, and 40, respectively. The conditions and outcomes of these simulations are detailed in Table 2-6. The values of this table indicate that CEM surpasses the level-set DP method by producing lower hydrogen consumption and degradation cost in a shorter simulation time. Additionally, there is a discernible trend where increasing the number of grid points results in lower operational costs. However, this comes at the cost of longer problem-solving times. This demonstrates a trade-off between result precision and

problem-solving speed. However, based on the simulation times of the CEM, the longest one is 209 seconds, and it is an acceptable duration for solving the problem. Therefore, simulation 4 is selected for further discussion.

Since the power distributions for the FC stacks and the battery are nearly identical when using both the CEM and level-set DP methods, this section will focus solely on the distributions derived from CEM for Simulation 4. Fig. 2-12 shows the power demand (Fig. 2-12a), FC stacks power (Fig. 2-12b), battery power (Fig. 2-12c), and battery SOC (Fig. 2-12d). This figure demonstrates that the battery efficiently manages high-dynamic loads by both supplying and absorbing power, which ensures the FC stacks operate smoothly.

Table 2-6. Comparison of conditions and results of level-set DP and CEM in case study 2.

			Level-set DP	**CEM**
Simulation 1	Simulations conditions	SOC grid gap	0.0001	0.0001
		u_i grid gap (W)	12700	12700
		$P_{FC,i}$ grid gap (W)	12700	-
		Discretization level	10^5	10^3
	Simulations results	H_2 consumption (gr)	367.4	345.1
		Degradation cost ($)	5.81	5.54
		Simulation time (s)	17	19
Simulation 2	Simulations conditions	SOC grid gap	0.0001	0.0001
		u_i grid gap (W)	6350	6350
		$P_{FC,i}$ grid gap (W)	6350	-
		Discretization level	20^5	20^3
	Simulations results	H_2 consumption (gr)	341.3	328.5
		Degradation cost ($)	5.42	5.26
		Simulation time (s)	68	57
Simulation 3	Simulations conditions	SOC grid gap	0.0001	0.0001
		u_i grid gap (W)	4233	4233
		$P_{FC,i}$ grid gap (W)	4233	-
		Discretization level	30^5	30^3
	Simulations results	H_2 consumption (gr)	334.5	327.6
		Degradation cost ($)	5.32	5.21
		Simulation time (s)	531	141
Simulation 4	Simulations conditions	SOC grid gap	0.0001	0.0001
		u_i grid gap (W)	3175	3175
		$P_{FC,i}$ grid gap (W)	3175	-
		Discretization level	40^5	40^3
	Simulations results	H_2 consumption (gr)	332.7	327.2
		Degradation cost ($)	5.28	5.19
		Simulation time (s)	2174	209

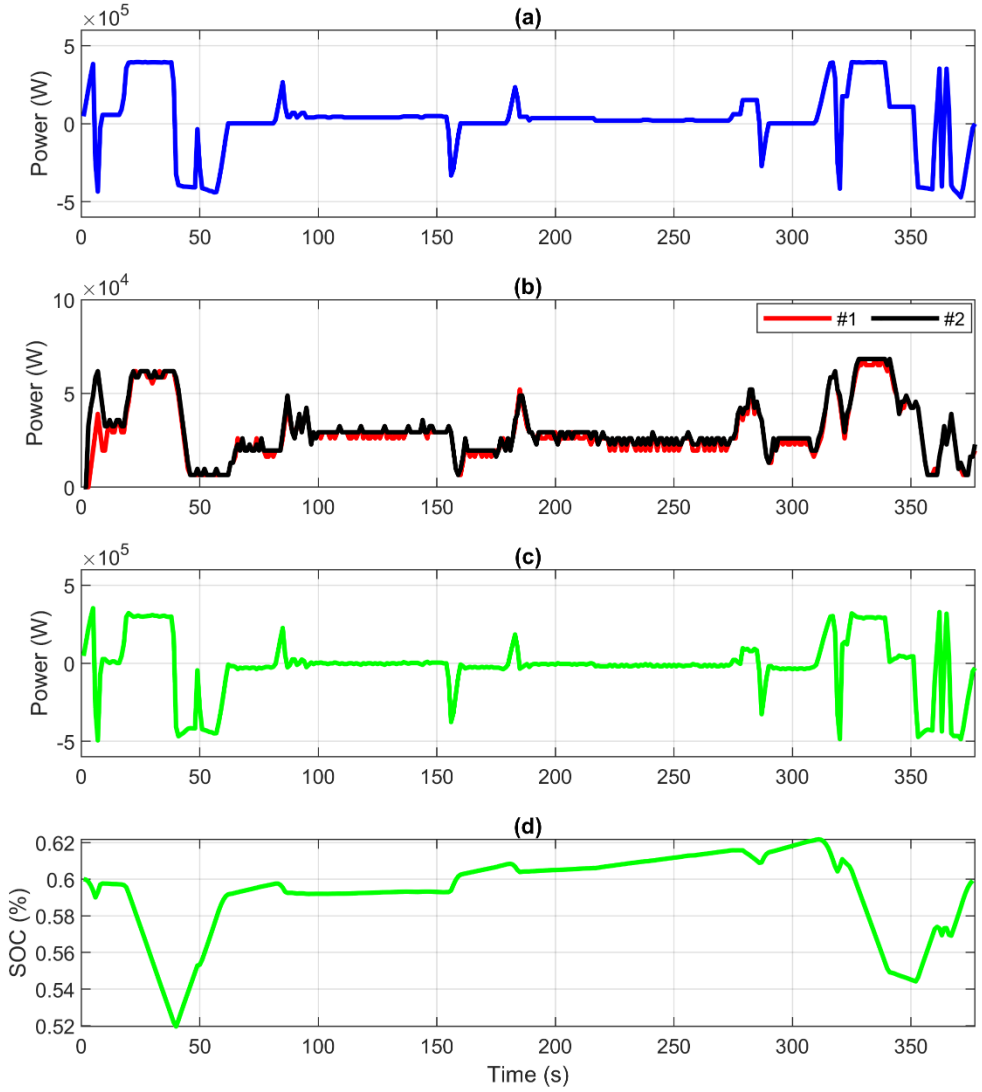

Fig. 2-12. The obtained results in case study 2: a) Power demand, b) FC stacks net power, c) Battery power, and d) Battery SOC.

Fig. 2-13 illustrates the distribution of various operational costs for the FC stacks, including fuel and degradation costs. For each FC stack, the larger circle chart on the left shows the total operating cost, while the smaller circle chart on the right details the breakdown of the degradation cost. As shown, the operational cost of stack 2 is higher than that of stack 1, which is attributed to its greater power generation depicted in Fig. 2-12. Additionally, the degradation costs for both stacks are roughly equal, with the exception of the fast-dynamic degradation cost, which is present in stack 2 but absent in stack 1.

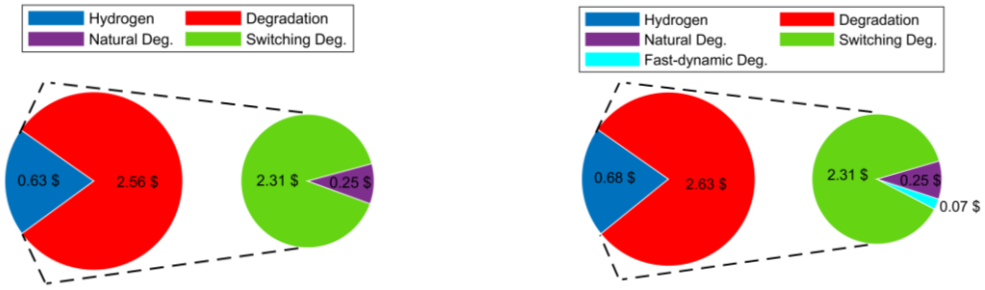

(a) (b)

Fig. 2-13. Operational cost distribution in case study 2: (a) FC stack 1, (b) FC stack 2.

2.5.2.2 Comparison with SQP

The results from the CEM method, which utilized 40 grids for state and control variables (referred to as simulation 4) and was chosen for its balance of accuracy and speed, are compared to those from the SQP method. Table 2-7 presents the findings from case study 2 for both the CEM and SQP methods.

Table 2-7. Comparison of the results of SQP and CEM methods in case study 2.

	SQP	**CEM**
H_2 consumption (gr)	457.6	327.2
Degradation cost ($)	5.96	5.19
Simulation time (s)	0.4	209

The table indicates that the CEM method reduces hydrogen consumption by 28.5% compared to the SQP method. Additionally, the degradation costs associated with the CEM method are 12.9% lower than those of the SQP method in the given case study. Taking into account the price of H2 at 0.004 $/gr, the operation costs of SQP and CEM are $7.79 and $6.5, respectively. Hence, using CEM decreases the operation cost by 16.6%. Considering that SQP operates as an online EMS while CEM functions offline, it is expected that the simulation time for the SQP method would be significantly shorter than that for the CEM method.

2.5.3 Case study 3

In the third case study, a long-haul heavy-duty truck equipped with four stacks of FC and a battery is investigated [56]. Using the vehicle parameters outlined in Table 2-8, along with the power calculation equations from Ref. [96] and the City Suburban Heavy Vehicle Cycle & Route (CSHVR) driving cycle, the requested power of the vehicle can be determined.

Table 2-8. Parameters heavy-duty truck.

Parameter	Symbol	Value
Vehicle mass	m	40000 (kg)
Rolling friction coefficient	c_r	0.006
Aerodynamic drag coefficient	c_d	0.73
Frontal area	A_f	9.75 (m^2)
Air density	ρ_{air}	1.225 (kg/m^3)
Gravitational acceleration	g	9.81 (m/s^2)
Differential efficiency	η_{diff}	0.97
Direct drive efficiency	η_{drive}	0.985

Four FC stacks, each rated at 75 kW from PowerCell Group, are used in this truck to collectively supply the required power. The polarization curve and I-P curve of this FC stack are presented in Fig. 2-14 [94].

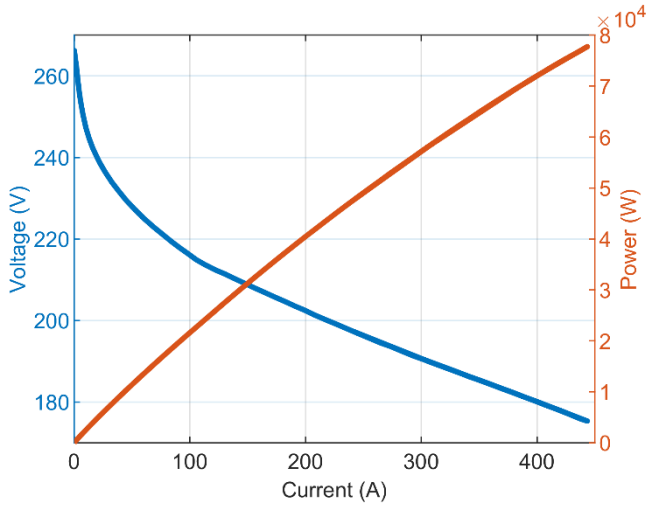

Fig. 2-14. Polarization and I-P curves of FC stacks used in case study 3.

The type of battery that is used to assist FC stacks to meet the demand power is the same cell as mentioned in case study 1 in Table 2-2. The distinction resides in the battery pack's configuration, comprising four parallel branches, with each branch having 144 series cells.

In this particular case study, there are a total of 9 variables, comprising 4 control variables and 4 state variables related to FC stacks power, along with 1 state variable associated with battery SOC. Hence, if 10 grid points are considered for each variable, the discretization level is 10^9, and the level-set DP encounters an error when attempting to solve a problem involving this quantity of variables. However, the discretization level of the CEM is 10^5, which is much lower than that of the level-set DP. Therefore, the CEM, whose validity was confirmed in case study 1 and case study 2 through comparison with the level-set DP and SQP, can successfully obtain the solution. This case study demonstrates the scalability and ability of the CEM to solve energy management problems for various FCSs with different configurations and applications, in comparison to conventional benchmark methods such as the level-set DP. Fig. 2-15 shows the demand power by the

truck (Fig. 2-15a), power generated by FC stacks (Fig. 2-15b), the battery power (Fig. 2-15c), and the SOC of the battery (Fig. 2-15d). Based on the figure, it is evident that the battery effectively fulfills its role by absorbing fast-dynamic loads, thereby ensuring smooth operation of the FC stacks. During low-power and negative-power phases, the battery is charged to adequately supply power during peak demand periods.

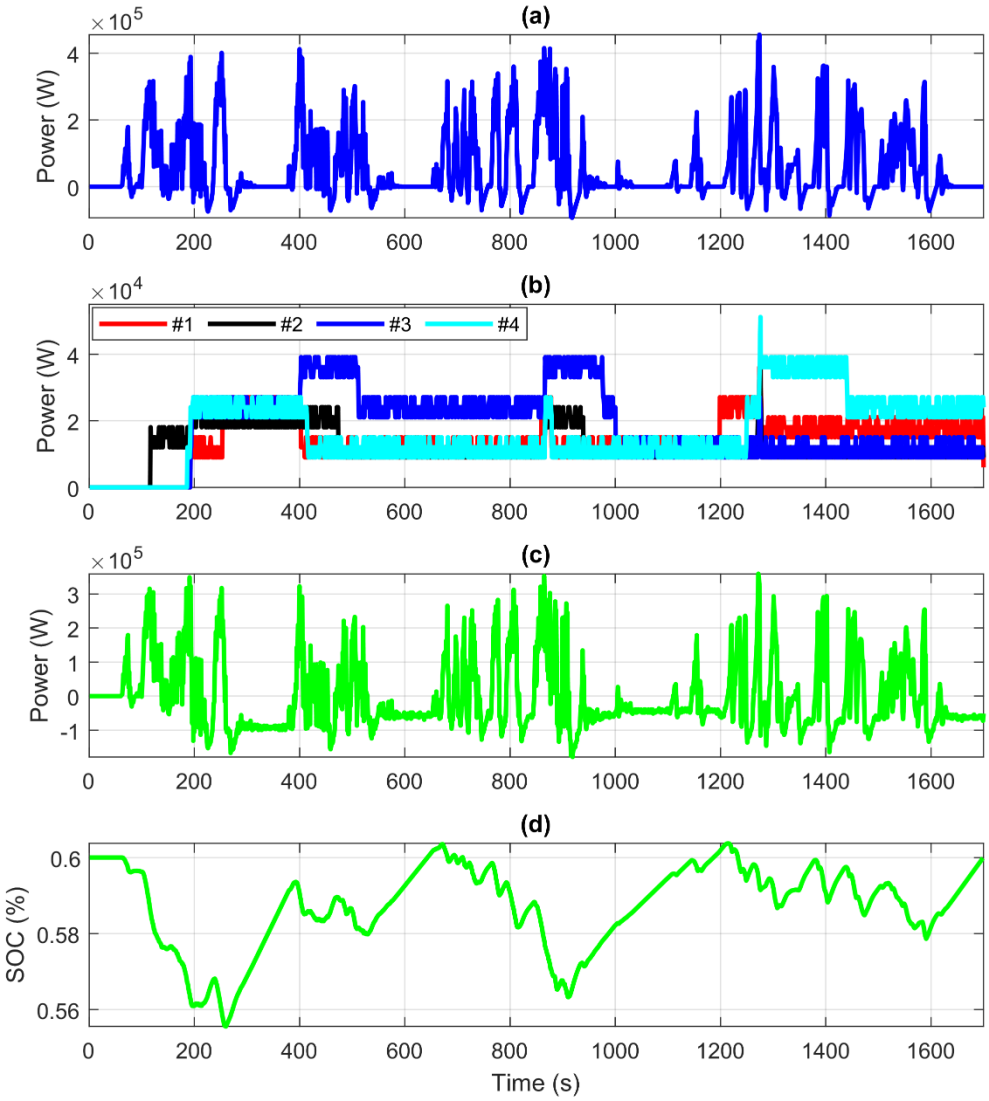

Fig. 2-15. Obtained results in case study 3: a) Power demand, b) FC stacks net power, c) Battery power, and d) Battery SOC.

Different operational costs of FC stacks during the CSHVR driving cycle can be observed in Fig. 2-16. For each FC stack, the left-hand chart (the larger circle) depicts the

total operating cost, whereas the right-hand chart (the smaller circle) provides a detailed composition of the degradation cost. Based on the presented figure and hydrogen cost, stack 3 assumes the primary role in meeting the vehicle's power demand, while stack 2 contributes the least towards this requirement. Another noteworthy observation is that the health-conscious nature of the proposed method results in the FC stacks incurring nearly equal degradation costs.

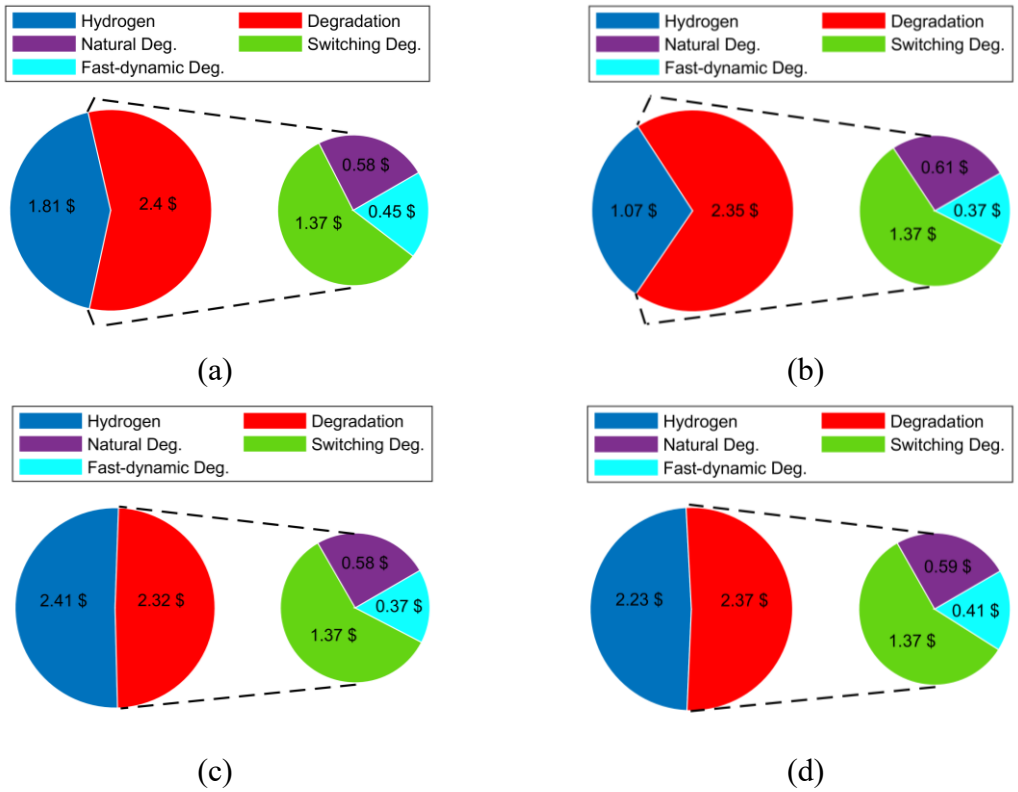

Fig. 2-16. Operational cost distribution in case study 3: (a) FC stack 1, (b) FC stack 2, (c) FC stack 3, (d) FC stack 4.

2.5.3.1 Comparison with SQP

Table 2-9 presents a comparison between the CEM and SQP methods applied to case study 3.

Table 2-9. Comparison of the results of SQP and CEM methods in case study 3.

	SQP	CEM
H2 consumption (gr)	2610	1881
Degradation cost ($)	10.03	9.45
Simulation time (s)	1.5	31007

The table shows that the CEM method reduces hydrogen consumption by 27.9% compared to the SQP method. Additionally, the degradation cost associated with the CEM method is 5.8% lower than that of the SQP method in the given case study. Considering the price of fuel at $0.004 per gram, the operation costs for SQP and CEM are $20.47 and $16.97, respectively. Therefore, using CEM decreases the operation cost by 17.1%. Given that SQP operates as an online EMS while CEM functions offline, it is anticipated that the simulation time for the SQP method would be considerably shorter than for the CEM method.

2.5.4 Discussion on the scalability of the CEM

The scalability of the CEM is a key attribute enabling its application across various types of HDVs and different operating conditions. This section elaborates the way of applying the CEM to different HDVs and operation conditions.

The CEM is designed to be flexible, allowing it to handle various configurations of FC stacks and battery systems. To apply the CEM to different types of HDVs, it is essential to specify several parameters, and give them as input to the CEM:

- **Requested Power:** The power demand of the vehicle.
- **FC stacks data:** Information about the number of stacks, their rated power, constraints and polarization curves.

- **Battery data:** Curves including open circuit voltage vs. SOC, internal resistance vs. SOC, data including capacity, voltage and current of a cell, as well as the number of cells in series and parallel.

- **Converters specifications:** The power usage and efficiency of the converters.

These data are related to the operation conditions and sizing of the FCS and are not the focus of this work; therefore, the necessary data are sourced from the manufacturer and literature. Provided that the sizing is correct, and the FC stacks and the battery can meet the required power at any given time, the CEM effectively distributes power between the FC stacks and the battery to minimize operational costs. This is elaborated in the theoretical section in "3.2.2.1 Concept of CEM Forward Calculation."

The main factor helping the CEM to be scalable is the way of defining state and control variables which was elaborated in "3.1.1 State space equation" section. Also, the incorporation of various filter mechanisms within the CEM ensures efficient handling of large numbers of control and state variables. These filters use the FCS data given to the CEM at the beginning of the procedure. Filters make the method scalable for more complex systems without a problem in solving the energy management. The ability to manage multiple FC stacks and battery configurations highlights the robustness of the CEM in adapting to diverse vehicle powertrains.

The method's scalability has been validated through different case studies, including an aircraft, a tramway, and a truck. Each case study presents unique power requirements and configurations, demonstrating the CEM's ability to adapt and optimize energy management across various scenarios. The CEM has shown superior performance compared to

established optimization techniques such as DP and SQP, reinforcing its applicability and scalability.

The systematic approach provided in the Fig. 3 and the following explanation in section 3 outlines the steps required to implement the CEM across different vehicle types and operating conditions. This practical guide ensures that the method can be easily adapted to specific applications, making it a versatile tool for optimizing energy management in FC-HEV.

Based on above-mentioned discussion, the proposed CEM offers a scalable and universal solution for energy management in HDVs. Its efficient handling of complex systems, and validation through diverse case studies confirm its potential for broad application. This adaptability ensures that the CEM can meet the demands of various vehicle types and operating conditions, providing an effective strategy for minimizing operational costs and enhancing system performance.

2.6 Conclusion

This paper introduces a CEM designed for energy management in HDVs equipped with MFCSs and a battery system. The CEM is a scalable, health-conscious, and time-efficient benchmark method. The method leverages various filters, such as battery power, SOC-range, and SOC filters, to address challenges related to the curse of dimensionality and time-consuming processes. Also, these filters enable CEM to be scalable and to solve the energy management problem in systems with multiple FC stacks, which involve a large number of state and control variables. Additionally, a health-conscious multi-objective function is utilized to minimize hydrogen consumption and degradation costs. Application

of the proposed method on the NASA X-57 Maxwell aircraft demonstrated a 2% reduction in operational costs and a 10.5% decrease in calculation time compared to level-set DP when employing 20 control variable grids. This case study demonstrates that solving energy management with the CEM approach can achieve a 14.6% operational cost reduction compared to the SQP method. The second case study, involving a hybrid dual-stack tramway with 40 grid points, shows the CEM approach surpassed both level-set DP and SQP. The CEM achieved a 1.7% reduction in operational cost and a 90.4% improvement in simulation time compared to level-set DP. Additionally, the CEM offered a cost-effective advantage, with a 16.6% lower operational cost than SQP. The validated CEM, initially tested in case studies 1 and 2, is then applied to a truck equipped with four 75 kW FC stacks and a battery system, effectively managing energy distribution in this scenario. Results from this case study highlight the method's capability to optimize FC stack health conditions, ensuring similar degradation costs across stacks. Comparing the CEM and SQP methods shows a 17.1% reduction in operation cost of case study 3. The paper bases the sizing of FC stacks and batteries on existing literature. Future work aims to develop a method that simultaneously determines the size of FC systems and battery pack, stack allocation, and energy management based on driving cycles and power demands. For the energy management section, to accelerate the solution process, future research could employ heuristic methods to guide the search process towards more promising areas of the state space. Additionally, approximation algorithms could be used to find near-optimal solutions more quickly, balancing solution quality and computational efficiency.

Chapter 3 - Integrated Sizing–EMS for Heavy-Duty Multi-Stack FC-HEVs

This chapter presents the ISEMS framework for heavy-duty MFCS applications. The chapter focuses on the joint sizing-control formulation, GA-MPC implementation, and cost-durability trade-off analysis.

3.1 Abstract

This paper proposes a degradation-aware integrated sizing and energy management strategy (ISEMS) for hybrid multi-stack fuel cell systems (MFCSs) in heavy-duty vehicles (HDVs), aiming to minimize total cost while enhancing system durability. While ISEMS approaches have been explored for single-stack systems, their extension to MFCSs remains unexplored. The proposed method simultaneously determines the size of the fuel cell (FC) stacks and the battery configuration, and evaluates the performance of the system under different FC stack arrangements. Unlike conventional approaches, sizing and stack allocation are handled jointly, without assuming a fixed total FC capacity. The degradation behavior of both the FC stacks and the battery is embedded in both sizing and energy management stages to improve system longevity. A hybrid genetic algorithm–model predictive control (GA–MPC) framework is employed, where GA explores design configurations and MPC ensures degradation-aware power allocation. The method is validated in a long-haul truck case study, where ISEMS reduces total cost by 68% and 50%

compared to single-stack and quad-stack configurations from previous studies. Experimental validation is also conducted using data from FCs installed on a multi-stack test bench, in order to identify their optimal arrangement with the proposed method. Sensitivity analyses also demonstrate that widening the battery state of charge (SOC) window leads to additional cost reductions of up to 67.4% by enhancing battery utilization. The proposed framework offers a scalable, degradation-aware solution for cost-effective MFCS design and control in HDV applications.

Keywords: proton exchange membrane fuel cell, design–operation integrated framework, multi-objective optimization, modular fuel cell system, degradation-aware optimization, heavy-duty vehicles

3.2 Introduction

The transportation sector uses 25% of the world's energy, relying mainly on fossil fuels and making a significant contribution to climate change [2]. While hybrid and battery electric vehicles (HEVs and BEVs) support cleaner transport, BEVs face major limitations for heavy-duty vehicles (HDVs), including short range, insufficient charging infrastructure, and bulky battery systems [7, 8].

Hydrogen is a promising energy source, with global demand projected to reach 1,370 MMT by 2050, up to 33.1% of which may come from transportation [10, 11]. Vehicles using fuel cells (FCs), particularly for HDVs, benefit from hydrogen's high energy density and fast refueling. Proton exchange membrane fuel cells (PEMFCs) are the most used in vehicles due to their low operating temperature, high power density, and compact, safe design [97]. However, PEMFCs face limitations like slow response and cold starts. To

overcome these, energy storage systems (ESSs) such as batteries and supercapacitors are integrated to enhance performance, protect the FC, and recover energy [1]. PEMFC-battery configurations are widely adopted in fuel cell hybrid electric vehicles (FC-HEVs) to ensure dynamic power support and system reliability [14].

While FC technology has matured for light-duty vehicles (LDVs) over the past two decades, its application to HDVs has gained interest more recently. A key advantage is reduced infrastructure needs, as HDVs often follow fixed routes, minimizing refueling station requirements [18]. High-power single-stack FC systems (FCSs) have been widely used in FC-HEV powertrains [98-100], but their output is insufficient for HDVs. Consequently, research is shifting toward multi-stack FC systems (MFCSs), which combine independent stacks to meet higher power demands. MFCSs offer advantages in power scalability, reliability, and spatial flexibility [26]. They also enhance modularity and adaptability across varying operational needs. However, managing multiple stacks and an ESS creates system complexity, requiring careful sizing and a robust energy management strategy (EMS) to fully exploit MFCS capabilities.

Accurate sizing of the FC and battery is essential in FC-HEVs to ensure that power demands are reliably met while avoiding excess weight and cost [32]. Undersizing impairs load supply, whereas oversizing increases weight and cost, potentially reducing appeal [33]. This is particularly crucial for HDVs, where high power demand and durability necessitate precise sizing for feasibility and cost-efficiency. [34]. Prior studies have addressed this: [53] proposed an FC-HEV outperforming the first-gen Toyota Mirai in gradeability and reducing power source cost by 28%; [54] found that in FC/battery buses, battery-dominant setups reduced degradation and lifetime costs; [55] studied FC-hybrid trains using real

locomotive data, showing higher battery-to-FC ratios; and [56] developed a sizing method for FC trucks, concluding that while batteries are currently cheaper, FCs may offer long-term economic benefits.

The EMS manages power distribution to follow the powertrain power request whilst minimizing hydrogen use and system degradation, and is typically classified as rule-based, optimization-based, or intelligent [101]. Rule-based EMSs are simple and efficient but rely on empirical tuning, limiting optimality [37, 102]. Optimization-based EMSs define an objective function with constraints to minimize it [103]. Dynamic programming (DP) has been used for offline global optimization in FC systems [44-46], but its application in MFCSs is limited due to computational complexity. Even as a benchmark [47], DP is often simplified and lacks health awareness. To address this, the authors of [104] proposed the Constrained Exploration Method (CEM), which uses filters to reduce DP's computational burden. This method was also adopted in an aircraft-focused study to evaluate the performance of single- and multi-stack FC configurations [105]. Online methods have also been proposed for real-time use. For example, [38, 39] introduced hierarchical EMSs, [41] extended ECMS to multi-stack and aircraft applications, while [42, 43] developed strategies for trams and modular FCs, and [106] introduced a predictive EMS combining rule-based control and MPC. Although suitable for real-time applications, these online approaches typically optimize over short horizons. More recently, advanced intelligent strategies such as deep reinforcement learning have been applied to FC buses to integrate future road information with cabin comfort control [107], while other health-conscious frameworks have demonstrated that coupling thermal management of the cabin and energy sources can significantly enhance system durability [108].

Some studies have shown that separating sizing and EMS design can reduce performance and increase energy storage costs, emphasizing the need for joint or integrated optimization [67]. Since component sizes constrain FCS operation, sizing directly influences EMS performance. Joint optimization of sizing and EMS enhances durability, cost-efficiency, and overall system effectiveness. However, these studies have primarily focused on single-stack FCSs, without addressing multi-stack configurations. In [68], a method based on Toyota Mirai data and MATLAB-SIMULINK modeling was proposed to optimize component sizing and power distribution, prolonging FC durability and reducing fuel consumption. In [69], integrated modeling, sizing, and EMS using tunnel DP and Pareto analysis reduced operational cost in FC-HEVs. Study [70] showed that slightly undersized FCs with well-tuned EMSs offered optimal trade-offs in consumption, degradation, and cost. In [71], DP-based sizing for FC-battery excavators showed that increasing the number of FC cells led to reduced hydrogen consumption and better SOC sustainability, while excessive sizing adversely affected battery performance. A hybrid ESS with an adaptive-weight genetic algorithm enhanced range and extended component life in [72]. Lastly, [73] proposed a cost-effective sizing method using chance-constrained optimization, evaluating three ESS types across HDV applications with FC degradation considerations.

However, the impact of stack number and sizing on MFCS performance has often been overlooked, despite their significant influence on both capital and operational costs. While a higher number of stacks allows the EMS to manage power more flexibly and potentially reduce degradation and hydrogen use, allowing for unequal rated powers introduces many possible configurations, each with different cost and performance implications. In [62],

modular FC configurations with differential control improved durability and reduced total ownership cost and emissions by up to 23%, though the analysis was limited to three dual-stack setups. The authors of [63, 64] proposed two optimization methods for MFCSs in HDVs: [63] used bi-level optimization to enhance efficiency and RUL, while [64] extended it to a multi-objective framework minimizing cost and maximizing durability. Both studies confirmed performance gains and hydrogen savings over equal-stack setups. In [65], SQP-based EMS was used to optimize stack allocation, showing that increasing the number of stacks from two to three and from three to four reduced operational costs by 6.33% and 14.87%, respectively. These studies developed multi-stack configurations based on predefined single-stack sizing, highlighting the critical role of appropriate stack allocation in minimizing FCS costs.

To provide a concise synthesis, the Table 3-1 categorizes the scope of the relevant studies. This analysis clearly highlights the persistent research gap regarding the integrated optimization of component sizing and EMS for MFCSs.

Table 3-1. Summary and comparison of literature focusing on power source sizing and EMSs for FC-HEVs.

Ref.	FC sizing	Battery sizing	EMS	Multi-stack	Stack allocation	FC count Analysis
[53-56]	✓	✓	×	×	×	×
[37-39, 41-47, 101, 102, 104-106, 109, 110]	×	×	✓	✓	×	×
[107, 108]	×	×	✓	×	×	×
[68-73]	✓	✓	✓	×	×	×
[62]	✓	×	✓	✓	×	×
[63-65]	×	×	✓	✓	✓	✓
This study	✓	✓	✓	✓	✓	✓

To the best of our knowledge, existing studies have not addressed sizing and EMS for reducing investment and operational costs in MFCSs. Some explore finite configurations or focus on stack allocation with fixed total FCS size, often overlooking battery sizing. This leaves a gap in integrated approaches to sizing, stack allocation, and EMS. To fill this, an optimization-based framework called the Integrated Sizing and Energy Management Strategy (ISEMS) is proposed, which jointly determines FC and battery sizes to minimize total cost. The total cost includes both investment and operational costs. The investment cost accounts for the expenses associated with FC systems, battery, and power converters, while the operation expense reflects the cost of hydrogen usage as well as the degradation costs of FC stacks and the battery. Unlike prior works that fix FC size before allocation, the proposed approach unifies stack sizing and allocation, and analyzes how the number of stacks affects investment and operational costs. The SOH constraints have been also added into the formulation to improve system durability. Therefore, the main contributions of this study can be summarized as follows:

- An optimization-based method is developed to simultaneously address ISEMS in MFCSs, with the goal of minimizing both operational and investment costs.
- The sizing and allocation of FC stacks are treated as a single integrated process, rather than being handled separately with a predefined total FC size.
- Joint determination of battery size and FC configuration, with SOH considerations included to ensure a integrated and durable system design.
- Optimal FC system sizes are identified for different numbers of FC stacks, and the impact of stack quantity on both investment and operational costs is analyzed.

The remainder of this paper is structured as follows: Section 2 presents system modeling; Section 3 details the ISEMS method; Section 4 reports simulation results; and Section 5 concludes with key findings.

3.3 System Modeling

3.3.1 MFCS Powertrain Configuration

This study employs a parallel architecture due to its inherent advantages in enabling independent control of each FC stack and enhancing system redundancy. In this design, a unidirectional DC-DC converter connects each FC stack to the DC bus, while the ESS is connected via a bidirectional DC-DC converter to allow for both charging and discharging. The configuration of the parallel MFCS powertrain is depicted in Fig. 3-1, and the number of stacks can vary based on the application.

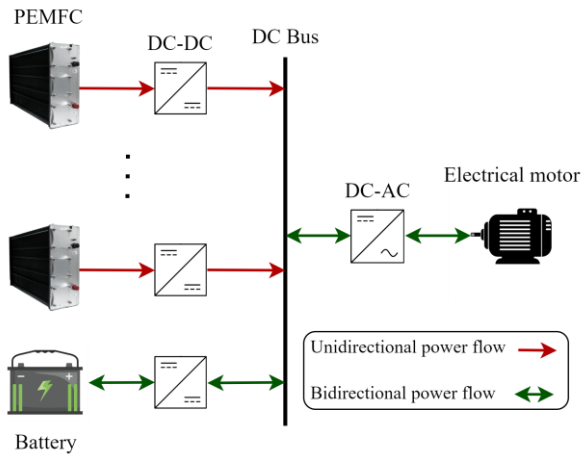

Fig. 3-1. The configuration of an MFCS powertrain.

The MFCS operates under a power balance constraint, expressed in (3-1), which ensures that total power demand is met by the available sources:

$$\frac{P_{Req}}{\eta_{DC-AC}} + P_{Aux} = \eta_{DC-DC,FC} \sum_{i=1}^{N_{st}} P_{FC,i} + \eta_{DC-DC,bat} P_{bat} \tag{3-1}$$

Here, P_{Req} is the load demand, P_{Aux} is auxiliary power of FCs, $P_{FC,i}$ is the *i*th FC stack output power, and P_{bat} is the battery power. Conversion efficiencies are denoted by η_{DC-AC} (inverter), $\eta_{DC-DC,FC}$ (FC converters), and $\eta_{DC-DC,bat}$ (battery converter). N_{st} is the total number of FC systems in the MFCS.

3.3.2 PEMFC Model

The authors of [111] proposed a semi-empirical model, which has been widely utilized in subsequent studies, to characterize the performance of PEMFCs based on experimental data. In this formulation, the output voltage of an individual cell, denoted as V_C, is expressed as the sum of four components:

$$V_C = E_{Nernst} + V_{act} + V_{ohmic} + V_{con} \tag{3-2}$$

where E_{Nernst} represents the reversible potential of the cell, while V_{act}, V_{ohmic}, and V_{con} correspond to the voltage losses due to activation, ohmic resistance, and concentration effects, respectively. The reversible potential is computed as (3-3) to (3-7):

$$\begin{aligned} E_{Nernst} = {} & 1.229 - 0.85 \times 10^{-3}(T_{FC} - 298.15) \\ & + 4.3085 \times 10^{-5} T_{FC}\left[\ln\left(P_{H_2}\right) + 0.5 \ln\left(P_{O_2}\right)\right] \end{aligned} \tag{3-3}$$

$$V_{act} = \xi_1 + \xi_2 T_{FC} + \xi_3 T_{FC} ln\left(C_{O_2}\right) + \xi_4 T_{FC} \ln(I_{FC}) \tag{3-4}$$

$$C_{O2} = \frac{P_{O2}}{5.08 \times 10^6 \exp(-498/T_{FC})} \tag{3-5}$$

$$V_{ohmic} = -I_{FC} R_{internal} = -I_{FC}(\zeta_1 + \zeta_2 T_{FC} + \zeta_3 I_{FC}) \tag{3-6}$$

$$V_{con} = Bln\left(1 - \frac{J_{FC}}{J_{max}}\right) \tag{3-7}$$

The detailed explanation of the utilized FC model parameters can be found in [76].

Hydrogen consumption for the FC stack is determined using the relation provided in [55], expressed as (3-8):

$$\dot{m}_{H_2} = 1.05 \times 10^{-8} \frac{P_{FC}}{V_C} \tag{3-8}$$

Where $\dot{m}_{H_2}$ indicates the hydrogen flow rate ($\mathrm{kg.\,s^{-1}}$), and P_{FC} represents the power generated by the FC stack (W).

The main operating conditions that lead to PEMFC performance loss include start-stop cycles, variable power demand, and operation under high or low load levels [112]. The amount of PEMFC degradation (in %) can be calculated by (3-9) [113]:

$$Deg_{FC} = \left(k_s n_s + k_f \Delta P_{FC} + k_l t_l + k_h t_h\right) \tag{3-9}$$

where k_s, k_f, k_l, and k_h represent the coefficients corresponding to start-stop events, fast load changes, low-power operation (defined as power below 5% of the FC rated power), and high-power operation (defined as power exceeding 90% of the FC rated power), respectively. The numerical values of these coefficients are provided in Table 3-2, based on data reported in [113]. Additionally, n_s denotes the number of start-stop events,

ΔP_{FC} indicates the magnitude of load variation (W), while t_l and t_h represent the durations of low-power and high-power operations (h), respectively.

Table 3-2. Coefficients related to FC degradation.

Coefficient	Value
k_s	1.379×10^{-3} $(\%.cycle^{-1})$
k_f	4.41×10^{-9} $(\%.W^{-1})$
k_l	8.662×10^{-4} $(\%.h^{-1})$
k_h	10^{-3} $(\%.h^{-1})$

3.3.3 Battery Model

The ESS in this study is a lithium-ion battery, which is utilized to recover energy during braking and regulate peak power needs. Because it has been widely utilized and verified in research related to EMS, the battery is represented using an internal resistance-based model [114] During discharge, the battery current (I_{bat}) assumes a positive value, whereas it becomes negative when the battery is being charged. The battery's behavior under these operating modes is captured through equations (3-10) to (3-13) [25].

$$V_t(t) = V_{OC}(t) - I_{bat}(t)R_{bat}(t) \tag{3-10}$$

$$P_{bat}(t) = V_t(t)I_{bat}(t) \tag{3-11}$$

$$I_{bat}(t) = \frac{V_{OC}(t) - \sqrt{V_{OC}(t)^2 - 4R_{bat}(t)P_{bat}(t)}}{2R_{bat}(t)} \tag{3-12}$$

$$SOC(t) = SOC(t_0) - \eta_{bat}\frac{\int_{t_0}^{t} I_{bat}\, dt}{Q_{bat}} \tag{3-13}$$

where P_{bat}, η_{bat}, Q_{bat}, R_{bat}, V_{OC} and V_t correspond to the battery's output power (W), Coulombic efficiency, capacity (Ah), internal resistance (Ω), open-circuit voltage (V) and terminal voltage of the battery.

The continuous charge and discharge of the battery result in a gradual decline in its performance, primarily driven by irreversible physical and electrochemical transformations. A prominent indicator of battery aging is the reduction in capacity. To quantify this degradation, a control-oriented battery aging model proposed in [115] is employed in this study, whose validity has been confirmed in previous works. The model utilizes the Arrhenius-based formulation to estimate the capacity loss percentage of the battery cell (ΔQ_{cell}) with respect to its initial capacity (assumed to be 100%) as presented in [116]:

$$\Delta Q_{cell} = B(c)\exp\left(\frac{-E_a(c)}{RT}\right)A(c)^z \tag{3-14}$$

where c represents the c-rate, parameter B is a pre-exponential factor that varies with the c-rate, with its values specified in Table 3-3. R and T refer to the universal gas constant (8.31 $\mathrm{J.mol^{-1}.K^{-1}}$) and the battery cell temperature (K), respectively. The discharge throughput, A, expressed in ampere-hours (Ah), is a c-rate-dependent quantity. The exponent z, accounting for the power-law effect, is taken as 0.55. The activation energy $E_a(\mathrm{J.mol^{-1}})$, which also varies with the c-rate, can be determined using (3-15)..

Table 3-3. Pre-exponential coefficient (B) values based on battery c-rate.

c	0.5	2	6	10
B	31,630	21,681	12,934	15,512

$$E_a(c) = 31700 - 370.3c \tag{3-15}$$

As a battery reaches its end-of-life (EOL) in vehicles, it typically loses 20% of its capacity. Accordingly, the associated discharge throughput (Ah) can be calculated using equation (3-16), while the total number of charge-discharge cycles at EOL is estimated by equation (3-17) [117].

$$A_{EOL}(c) = \left[\frac{20}{B(c)\exp\left(\frac{-E_a(c)}{RT}\right)}\right]^z \tag{3-16}$$

$$N_{EOL}(c) = \frac{A_{EOL}(c)}{Q_{cell}} \tag{3-17}$$

Consequently, the battery SOH and its rate of degradation can be formulated as follows:

$$SOH_{bat}(t) = 1 - \frac{\int_0^t \left|I_{bat,cell}(t)\right| dt}{2N_{EOL}(c)Q_{cell}} \tag{3-18}$$

$$\dot{SOH}_{bat}(t) = -\frac{\left|I_{bat,cell}(t)\right|}{2N_{EOL}(c)Q_{cell}} \tag{3-19}$$

The initial SOH is assumed to be 100%, and $I_{bat,cell}$ represents the current of a single cell.

The reported battery-related optima are specific to the adopted battery chemistry and parameter set; different chemistries may shift the trade-off among cost, degradation, power capability, and mass, although the proposed framework itself remains unchanged.

3.4 Integrated Sizing and EMS Design

To ensure optimal performance of FC-HEVs, an integrated optimization framework is developed to jointly address component sizing and EMS design (Fig. 3-2). It includes three layers: input data preparation, a GA–MPC optimization loop, and output extraction.

The input layer compiles FC models, battery specs, DC-DC converter data, requested power, and user-defined FC stack numbers (N_{st}), defining the design space and constraints. ISEMS is formulated as a mixed-integer nonlinear programming (MINLP) problem, with discrete sizing variables (e.g., FC type, battery configuration) and continuous control variables (e.g., power distribution). The objective and constraints are nonlinear due to degradation, hydrogen use, and system dynamics, making gradient-based methods unsuitable.

To solve this, a GA–MPC structure is used as a bi-level nested loop. The interaction mechanism functions as follows: The GA (outer loop) explores the discrete sizing space and generates a candidate sizing vector (S). This vector is passed to the MPC (inner loop), which uses these specific component sizes to simulate the mission profile and compute the optimal power split while respecting SOC, power limits, and degradation constraints.

After MPC execution, operational cost is calculated based on hydrogen use and component degradation. These results, specifically the operational cost and the degradation of components, are fed back to the GA. The most degraded FC stack is identified, and a weight factor (w) is computed to scale investment cost accordingly. A total cost is then formed by combining investment and operational costs using a degradation-based weighted sum (Eq. (3-20)). This equation serves as the mathematical coupling between the design

and control layers. It penalizes low-cost but high-degradation solutions, guiding the optimization toward durable, cost-effective configurations. This total cost becomes the GA's fitness value. The GA evolves the population through selection, crossover, and mutation until a certain number of generations or convergence is obtained.

The specific parameters for the GA are calibrated to balance exploration capability with computational efficiency for two case studies of this paper (Table 3-4). Population size and generation limits are scaled according to the search space complexity of each case study to ensure robust convergence within a feasible timeframe.

Table 3-4. GA parameters and settings in case studies 1 and 2.

Parameter	**Case study 1**	**Case study 2**
Population Size	100	50
Max. Generations	80	30
Mutation Function	Adaptive Feasible	Adaptive Feasible
Elite Count	3	3
Crossover Fraction	0.9	0.9

The end result consists of optimal FC stack types, battery configuration, and the power generated by the FCs and battery, which represents a co-optimized sizing and EMS solution balancing cost and durability. This process is repeated for each $N_{st} \in A$, allowing comparison across different FC stack counts and storing the best result for each configuration.

Sizing and EMS are tightly coupled in MFCSs. The selected component sizes define the admissible operating region and the loading conditions of the FC stacks and the battery, while the EMS determines how those components are actually used during the mission.

Therefore, the quality of a sizing solution can only be assessed through the EMS response associated with that solution.

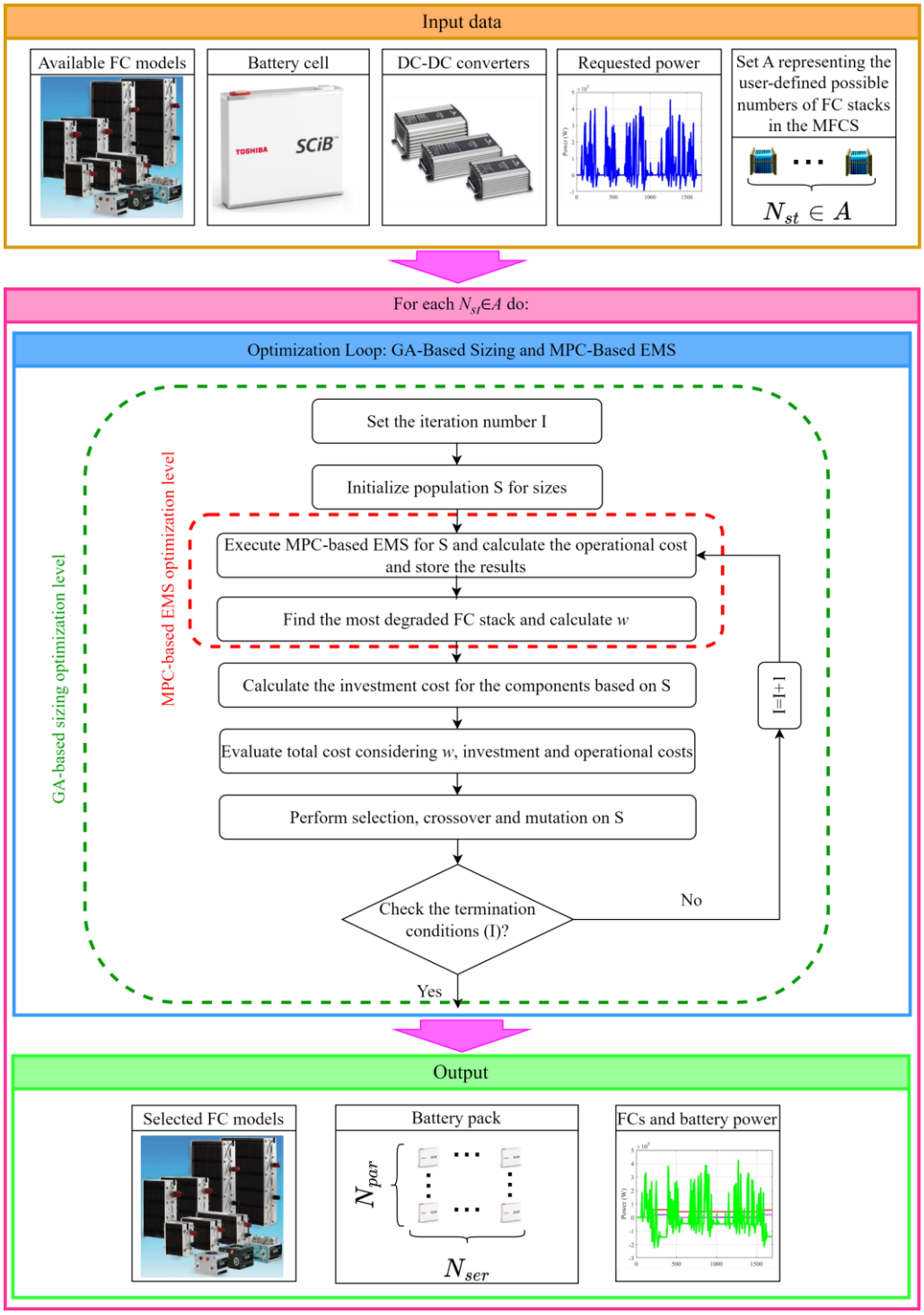

Fig. 3-2. GA–MPC framework for degradation-aware ISEMS in MFCSs.

3.4.1 Sizing Based on GA

In the proposed framework, the sizing task is addressed using the GA, which is a population-driven metaheuristic capable of effectively handling optimization problems characterized by mixed-integer variables, nonlinearity, and non-convexity [118]. The GA determines the optimal configuration of the FC system and battery pack by evolving a population of candidate solutions over successive generations. Each individual in the population represents a sizing candidate defined by a chromosome composed of discrete genes.

The decision variables include the types of FC stacks selected for the MFCS and the configuration of the battery pack. Specifically, the genes encode:

- The type index of each FC stack (discrete, selected from the available FC models),
- The number of battery cells in series,
- The number of battery cells in parallel.

The length of each chromosome is equal to $N_{st} + 2$, where N_{st} represents the FC stacks number and the additional two entries correspond to the battery configuration (series and parallel cell counts). Each chromosome is represented as a vector *S*, for example *S* = [3, 4, 4, 6, 205, 8], which denotes a configuration with four FC stacks (model indices 3, 4, 4, and 6), 205 battery cells in series, and 8 in parallel. This encoding allows the algorithm to evaluate different combinations of FC and battery configurations in a compact and flexible manner. Based on the structure of vector *S*, in which all elements are discrete integers, an integer version of the GA is adopted to perform the optimization.

The GA starts with an initial population generated randomly within predefined bounds. It evaluates each individual using the nested MPC-based EMS and total cost function. Based on the fitness values, individuals are selected for reproduction, and new candidates are generated through crossover and mutation. This evolutionary process is repeated across generations until a termination criterion is satisfied.

The total cost associated with each sizing candidate is computed using a weighted sum of the investment and operational costs. The investment cost reflects the capital expenses associated with the selected FC and battery configurations. However, a direct summation of the investment cost (a long-term capital expenditure) and the operational cost (a short-term expense per single mission) would result in an unbalanced objective function dominated entirely by the hardware cost. To resolve this time-scale mismatch and derive a cost function supported by the physical lifespan of the components, a degradation-based scaling factor w is introduced. To account for the mismatch in time scale between short-term operation and long-term investment, a degradation-based weight factor *w* is introduced. The final total cost (C_{tot}), used as the fitness metric within the GA, is formulated to represent the total cost per mission and is defined as (3-20):

$$C_{tot} = \frac{C_{inv}}{w} + C_{op} \tag{3-20}$$

where C_{inv} is the investment cost, C_{op} is the operational cost obtained from the EMS evaluation, and *w* is a scaling factor derived from the degradation of the most degraded FC stack. The operational cost, which reflects short-term performance and degradation during the mission, is evaluated using the EMS and is detailed in Section 3.4.2.

The investment cost is expressed as (3-21):

$$C_{inv} = \sum_{i=1}^{N_{st}} c_{FC}.P_{FC,i,max} + c_{bat}.N_{ser}.N_{par}.Q_{cell}.V_{cell.nom} + \sum_{i=1}^{N_{st}} c_{con}.P_{FC,i,max} + c_{con}.max(P_{bat,max}, |P_{bat,min}|) \quad (3\text{-}21)$$

where $P_{FC,i,max}$ is the *i*th FC stack rated power. Parameters c_{FC}, c_{bat} and c_{con} are the unit costs of the FC, battery, and converter, respectively. In this study, $c_{FC} = 250\ \$.\mathrm{kW}^{-1}$, $c_{bat} = 178.41\ \$.\mathrm{kWh}^{-1}$, $c_{con} = 100\ \$.\mathrm{kW}^{-1}$ [119]. N_{ser} and N_{par} represent the number of battery cells in series and parallel. $V_{cell.nom}$ is the nominal voltage of a battery cell. $P_{bat,max}$ and $P_{bat,min}$ are the maximum and minimum powers of battery pack, respectively.

The weight *w* is defined as (3-22):

$$w = \frac{Deg_{FC,allowed}}{max_i(Deg_{FC,i})} \quad (3\text{-}22)$$

where $Deg_{FC,allowed}$ is the highest allowable degradation of the FC stacks, and $Deg_{FC,i}$ is the *i*th FC stack degradation.

The derivation of this formula is based on the definition of component EOL. In commercial applications, the EOL of a FC stack is empirically defined as the point where performance drops by a specific percentage (typically 10% voltage loss) from its beginning-of-life. Therefore, $Deg_{FC,allowed}$ represents the total "degradation budget" available to the stack. Since $Deg_{FC,i}$ represents the degradation consumed during one specific mission profile, the ratio w physically represents the projected number of missions (or cycles) the system can perform before the most critical stack fails. Consequently, the

term C_{inv}/w in (3-20) effectively converts the total capital expenditure into an amortized investment cost per mission. This ensures that the optimization objective C_{tot} is a consistent summation of the operational cost of the mission plus the depreciation cost of the hardware attributed to that mission. This formulation penalizes designs that may be cheap to build but degrade rapidly (low w, high depreciation), guiding the algorithm toward solutions that balance initial cost with long-term durability.

The sizing problem is subject to a set of constraints, as expressed in (3-23) to (3-25), that govern the selection of FC models and battery configuration bounds.

$$S_i \in \{1,2,\dots,N_{FC,models}\}, \qquad \forall i = 1,\dots,N_{st} \tag{3-23}$$

$$N_{ser,min} \leq N_{ser} \leq N_{ser,max} \tag{3-24}$$

$$N_{par,min} \leq N_{par} \leq N_{parr,max} \tag{3-25}$$

Where $N_{FC,models}$ is the number of available FC stack models. $N_{ser,min}$, $N_{par,min}$ are the minimum numbers of battery cells in series and parallel, and $N_{ser,max}$ and $N_{parr,max}$ are the maximum numbers of battery cells in series and parallel, respectively, based on the voltage constraints of the problem.

3.4.2 EMS Based on MPC

This section presents the formulation of an EMS based on MPC, implemented as the inner loop of the ISEMS framework. For each sizing candidate *S*, the operational cost C_{op} is evaluated using an MPC strategy. MPC is used to determine the optimal power split between the FC stacks and battery over a prediction horizon, based on a receding horizon

framework. At each time step, only the first control action is applied, and the optimization is repeated at the next step using updated measurements.

The system dynamics are modeled in a discrete-time state-space form as shown in (3-26) to (3-29) where the SOC is the state variable (x), the power of FC (P_{FC}) is the control variable (u) and the requested power (P_{req}) is a disturbance (d) [106].

$$\Delta x(t+1) = A\Delta x(t) + B\Delta u(t) + E\Delta d(t) \tag{3-26}$$

$$\Delta x(t) = \Delta SOC(t) = \frac{(SOC(t) - SOC(t-1))}{\Delta t} \tag{3-27}$$

$$\Delta u(t) = \Delta P_{FC}(t) = \frac{(P_{FC}(t) - P_{FC}(t-1))}{\Delta t} \tag{3-28}$$

$$\Delta d(t) = \Delta P_{req}(t) = \frac{(P_{req}(t) - P_{req}(t-1))}{\Delta t} \tag{3-29}$$

Two critical MPC design parameters, the prediction (P_h) and control (C_h) horizons, dictate the trade-off between control optimality and computational burden. In this work, both horizons are set to 10 seconds, a value selected based on established findings in FC-HEVs literature [86, 106, 113]. These studies demonstrate that a 10-second window provides sufficient look-ahead capability for effective energy management while maintaining a computational cost feasible for the nested sizing optimization.

The operational cost is evaluated using (3-30) to (3-34). At each time step, the MPC computes an optimal sequence of FC stacks power adjustments over the defined prediction horizon. From this sequence, denoted as $[\Delta P_{FC}^{*}(t),\ \Delta P_{FC}^{*}(t+1),\ \dots,\ \Delta P_{FC}^{*}(t+P_h-1)]$,

only the first element is implemented in accordance with the receding horizon approach. The optimization is then repeated at the next time step using updated system states.

$$J_{EMS} = \sum_{t=1}^{T} [C_{H_2}(t) + C_{Deg,FC}(t) + C_{Deg,bat}(t)] \tag{3-30}$$

$$C_{H_2}(t) = c_{H_2} \sum_{p=0}^{P_h-1} \sum_{i=1}^{N_{st}} \dot{m}_{H_2,i}(t+p) \tag{3-31}$$

$$C_{Deg,FC}(t) = \sum_{p=0}^{P_h-1} \sum_{i=1}^{N_{st}} \frac{c_{FC} P_{FC,i,\max} Deg_{FC,i}(t+p)}{SOH_{FC,i}(t+p)} \tag{3-32}$$

$$SOH_{FC,i}(t) = 1 - \sum_{q=1}^{t-1} Deg_{FC,i}(q) \tag{3-33}$$

$$C_{Deg,bat}(t) = c_{bat}.Q_{bat}.V_{bat.nom} \sum_{p=0}^{P_h-1} (SOH_{bat}(t+p) - SOH_{bat}(t+p+1)) \tag{3-34}$$

The cost function of EMS (J_{EMS}) consists of the costs of hydrogen consumption (C_{H_2}), FC stacks degradation ($C_{Deg,FC}$) and battery degradation ($C_{Deg,bat}$) over the mission profile duration (T), which can be seen in (3-30). The hydrogen cost at time step t, is computed as shown in (3-31). This cost reflects the cumulative hydrogen consumption of all N_{st} FC stacks over the prediction horizon P_h, where the mass flow rate of ith stack ($\dot{m}_{H_2,i}$) is obtained by (2-8). The total consumption is then multiplied by the hydrogen price (c_{H_2}=$0.004\ \$.\mathrm{g}^{-1}$).

In (3-32), the FC stacks degradation cost at time step *t* is calculated over the prediction horizon, by summing the degradation costs of all N_{st} stacks. The price of *i*th stack is determined by multiplying its maximum power by the unit cost of FC. The parameter $Deg_{FC,allowed}$ defines the highest allowable FC stacks degradation level to remain in service. When this threshold is exceeded, the corresponding stack is considered no longer operational. The degradation cost expression incorporates a penalty factor $\frac{1}{SOH_{FC,i}}$, which increases the cost contribution of stacks with lower SOH, thereby promoting operation strategies that preserve FC durability. The SOH of *i*th stack ($SOH_{FC,i}$) is obtained using (3-33), while the degradation of *i*th stack ($Deg_{FC,i}$) is evaluated according to (2-9).

Given that the starting and ending SOC values could differ, a fair comparison between different cases requires accounting for the net energy difference stored in the battery. To this end, after completing the EMS procedure, an additional term is incorporated to convert the SOC variation into its hydrogen-equivalent cost, as expressed in (3-35):

$$C_{H_2,\Delta SOC} = c_{H_2}.\frac{(SOC(t_0) - SOC(t_f)).Q_{bat}.V_{bat.nom}}{\eta_{bat}.\eta_{FC}.LHV_{H_2}} \tag{3-35}$$

where LHV_{H_2} is the lower heating value of hydrogen. Hence, the total operational cost of the FCS can be calculated as (3-36):

$$C_{op} = J_{EMS} + C_{H_2,\Delta SOC} \tag{3-36}$$

Hence, the equivalent hydrogen consumption cost consists of the hydrogen cost consumed by the FC stacks and the hydrogen cost associated with the difference between the initial and final SOC of the battery, as shown in (3-37):

$$C_{H_{2,eq}} = C_{H_2} + C_{H_2,\Delta SOC} \quad (3\text{-}37)$$

The constraints applied to the operation of the MFCS are defined by (3-38) to (3-42):

$$SOC_{min} \leq SOC(t+p) \leq SOC_{max} \quad (3\text{-}38)$$

$$P_{bat,min} \leq P_{bat}(t+p) \leq P_{bat,max} \quad (3\text{-}39)$$

$$P_{FC,i,min} \leq P_{FC,i}(t+p) \leq P_{FC,i,max} \quad (3\text{-}40)$$

$$P_{FC,i,min} \leq u_{FC,i}(t+p) \leq P_{FC,i,max} \quad (3\text{-}41)$$

$$\Delta P_{FC,i,min} \leq u_{FC,i}(t+p) - u_{FC,i}(t+p-1) \leq \Delta P_{FC,i,max} \quad (3\text{-}42)$$

where, $p \in \{1,2,\dots,P_h\}$, and the permitted lower and higher boundaries for each state and control variable are denoted by the subscripts "min" and "max." The rate of change in the *i*th stack's output power is constrained by (3-42).

3.5 Results

The effectiveness of the proposed ISEMS is evaluated through simulation in this section. Two case studies are considered for validation. In the first case study, ISEMS is employed to determine the optimal configuration of FC stacks and the battery pack size for a heavy-duty truck. The resulting configuration is then compared with a benchmark configuration reported in the literature. In the second case study, the FC stacks available in the Hydrogen Research Institute of the Université du Québec à Trois-Rivières are utilized to identify the optimal system configuration. The stack characteristics, experimentally measured, are integrated into the ISEMS framework for this purpose. All simulations were

performed using MATLAB R2024a on a server equipped with a 16-core 2.4 GHz processor, providing 4 GB of RAM per core.

3.5.1 Case Study 1

3.5.1.1 Input data

The first case study focuses on a long-haul heavy-duty truck, where the proposed ISEMS is applied to determine the optimal sizing of the FC stacks and battery pack, as well as the power distribution between these components. Based on the vehicle specifications detailed in Table 3-5 [56], the power demand equations established in [96], and the speed profile of the City Suburban Heavy Vehicle Cycle & Route (CSHVR), the vehicle's power requirements are calculated.

Table 3-5. Parameters heavy-duty truck.

Parameter	Symbol	Value
Vehicle mass	m	40000 (kg)
Rolling friction coefficient	c_r	0.006
Aerodynamic drag coefficient	c_d	0.73
Frontal area	A_f	9.75 (m2)
Air density	ρ_{air}	1.225 (kg/m3)
Gravitational acceleration	g	9.81 (m/s2)
Differential efficiency	η_{diff}	0.97
Direct drive efficiency	η_{drive}	0.985

In this case study, all nine off-the-shelf FC stack models offered by PowerCell Group, including both P-Stack and V-Stack series, are considered. The P-Stack series features high-power, compact stacks with metallic bipolar plates and high power density, while the V-Stack series includes lower-power stacks characterized by their ease of integration, gas

tolerance, and the ability to operate on both pure hydrogen and reformate gases. The specifications of these stacks are presented in Table 3-6, while the polarization and current-power (I-P) curves for individual cells of each model are illustrated in Fig. 3-3 [120, 121].

Table 3-6. Specifications of nine off-the-shelf FC stack models from PowerCell Group [120, 121].

	Rated power (kW)	**No. of cells**
V-stack	3	24
	6.5	48
	10	72
	26	192
	35.5	264
P-stack	78	275
	95	335
	119	419
	129	455

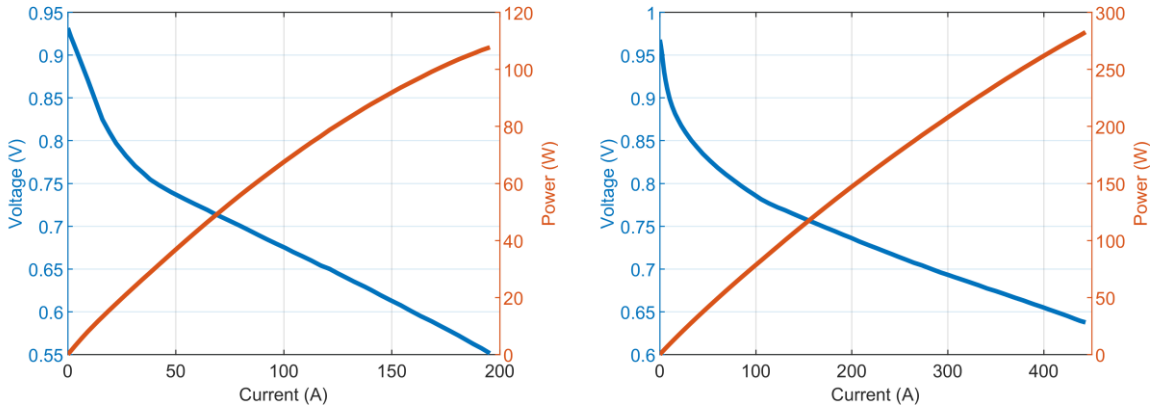

(a) (b)

Fig. 3-3. Polarization and I-P curves of (a) V-stack and (b) P-stack models used in case study 1.

The battery cell used in this case study is a high-power lithium-ion cell manufactured by Toshiba. Its specifications are presented in Table 3-7, and additional technical details are

available in [122]. At this stage, the SOC of the battery pack is assumed to be within the range [0.5, 0.7], with an initial value of 0.6.

Table 3-7. Battery cell parameters utilized in case study 1.

Parameter	Symbol	Value
Capacity (Ah)	Q_{cell}	10
Nominal voltage (V)	$V_{cell,nom}$	2.4
Max. power (W)	$P_{cell,max}$	1800
Min. power (A)	$P_{cell,min}$	-1500

3.5.1.2 Optimal configuration

To evaluate the optimal system configuration under varying levels of FC modularity, simulations were conducted for different numbers of stacks, ranging from $N_{st} = 1$ to $N_{st} = 6$. For each configuration, the ISEMS framework identified the optimal combination of FC stack models, the corresponding number of battery cells in series and parallel, and the power distribution strategy between the battery and the FC stacks. The resulting optimal configurations are summarized in Table 3-8.

Considering on this table, the five-stack configuration yields the lowest total cost ($79.65), driven by the lowest normalized investment cost per mission ($61.62) and a moderate operational cost ($18.03). It comprises four 35.5 kW stacks and one 78 kW stack, with a battery of 150 series and 8 parallel cells. Both FC (0.0021%) and battery (0.0007%) degradation levels remain acceptable. The three-stack case also performs well, achieving the lowest operational cost ($13.41), competitive total cost ($83.29), and minimal FC degradation (0.0021%). Although the six-stack configuration offers the lowest investment cost ($272,192.58), its total cost ($80.85) is slightly higher due to increased FC degradation (0.0023%), which shortens system lifetime and raises the normalized investment cost. The

single-stack setup shows the highest total cost ($123.00), driven by the highest normalized investment cost ($106.04) and FC degradation (0.0031%), highlighting the drawbacks of limited modularity. Battery degradation is consistently low (0.0005–0.0007%) across all cases, confirming effective sizing. These results confirm that higher FC modularity enhances cost-effectiveness and durability, with the five-stack design offering the most favorable trade-off for the given mission profile.

Table 3-8. Optimal configurations from ISEMS for different FC stack counts in case study 1, including costs and degradation levels.

	Optimal configuration		**Costs ($)**				**Degradations (%)**	
No. of FC stacks	FC stack sizes (kW)	Battery (N_{ser}, N_{par})	C_{inv}	C_{inv}/w	C_{op}	C_{tot}	Max. FCs	Battery
1	119	180s, 9p	339995.91	106.04	16.96	123.00	0.0031	0.0005
2	10, 95	213s, 8p	349879.43	77.14	13.58	90.72	0.0022	0.0005
3	10, 26, 78	196s, 8p	326121.55	69.88	13.41	83.29	0.0021	0.0005
4	2×35.5, 78, 95	156s, 9p	339003.85	74.41	19.77	94.18	0.0022	0.0006
5	4×35.5, 78	150s, 8p	288176.38	61.62	18.03	79.65	0.0021	0.0007
6	10, 2×26, 2×35.5,	141s, 8p	272192.58	63.65	17.20	80.85	0.0023	0.0007

Fig. 3-4 presents a heatmap illustrating the total cost associated with various configurations of a five-stack FCS. Each colored cell represents a unique feasible configuration, with the color gradient ranging from cyan (lower total costs) to magenta (higher total costs). Black cells denote infeasible configurations that cannot satisfy the load constraints. The configuration with the minimum total cost, highlighted by a red circle, consists of four 35.5 kW stacks and one 78 kW stack, combined with a battery comprising

150 cells in series and 8 parallel strings. The five-stack architecture was selected for this analysis as it yields the lowest total cost compared to all other evaluated architectures with one to six stacks.

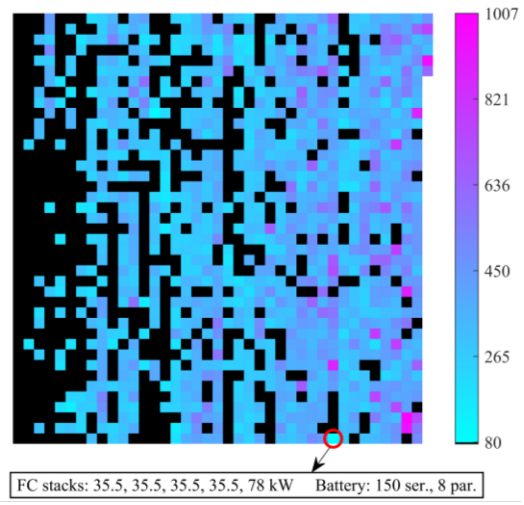

Fig. 3-4. Total cost heatmap of five-stack FCS configurations in case study 1. (Each colored cell represents a unique configuration; x- and y-axes are arbitrary indices with no physical meaning.)

Fig. 3-5 illustrates the operational cost breakdown, indicating that increasing the number of FC stacks does not necessarily improve cost performance and can, in some cases, worsen degradation. The equivalent hydrogen cost remains relatively stable across all configurations ($7.54–$7.97), suggesting that hydrogen demand is primarily driven by the driving cycle and energy requirements, rather than stack count. Battery degradation costs are consistently low ($0.17–$0.19), confirming that proper battery sizing effectively mitigates aging impacts and contributes minimally to the total cost. FC degradation cost emerges as the dominant factor in operational expenses. Although modularity increases flexibility, the number of stacks must be carefully selected to avoid excessive stress on individual units. Among the evaluated setups, the three-stack configuration provides the most favorable trade-off, balancing low degradation with efficient energy supply and yielding the lowest overall operational cost.

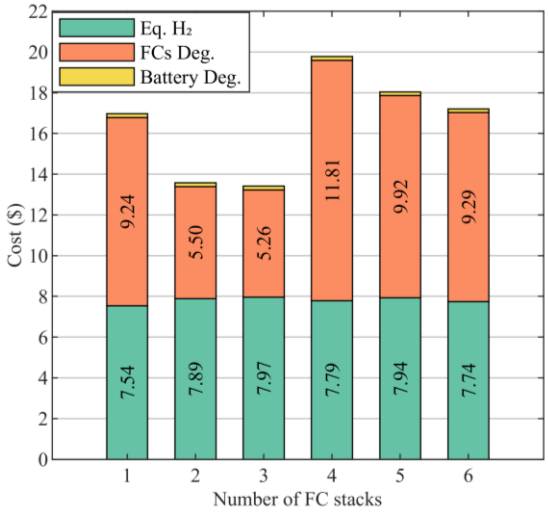

Fig. 3-5. Operational cost breakdown by number of FC stacks in case study 1.

Fig. 3-6 shows the SOH evolution of FC stacks for configurations with 1 to 6 stacks under a degradation-aware EMS. In the single-stack case, SOH declines more sharply due to the full load being carried by one unit, leading to concentrated degradation. As modularity increases, power is more evenly distributed, reducing stress on individual stacks. In configurations with three or more stacks, SOH trajectories converge despite differences in rated power, indicating that the EMS allocates power to promote uniform degradation. This highlights the EMS's role in balancing costs and durability through coordinated power distribution.

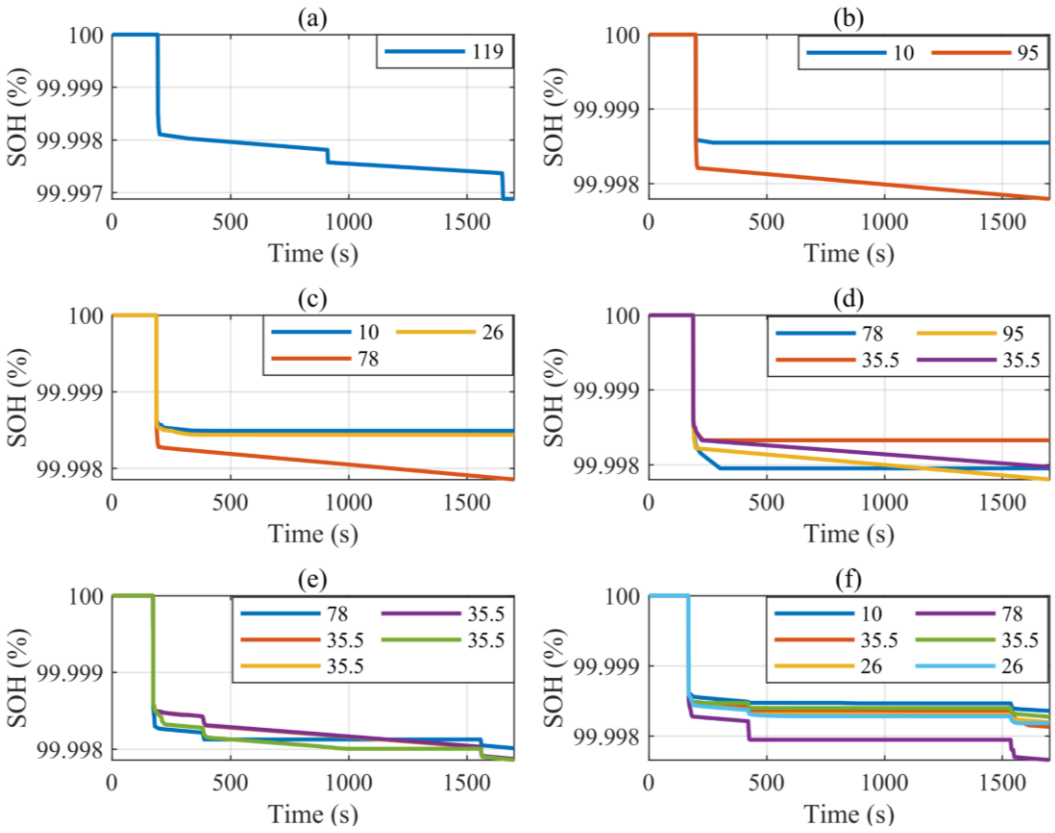

Fig. 3-6. SOH trajectories of FC stacks under degradation-aware EMS for (a) 1-stack, (b) 2-stack, (c) 3-stack, (d) 4-stack, (e) 5-stack, (f) 6-stack configurations in case study 1.

Fig. 3-7 illustrates results for the five-stack configuration from case study 1, selected for its lowest total cost and longest system lifetime. Subplot (a) shows highly variable requested power with several peaks. In (b), the five FC stacks collectively supply most of the power, with load distributed by a degradation-aware EMS to avoid overloading any single stack. This results in stable operation for most stacks, limiting rapid transitions and reducing degradation. Subplot (c) shows the battery responding to fast power fluctuations, supplying or absorbing energy to stabilize system output and protect FC stacks, especially evident around 400 s and 800 s. Subplot (d) confirms that battery SOC is effectively maintained within a stable range throughout the mission.

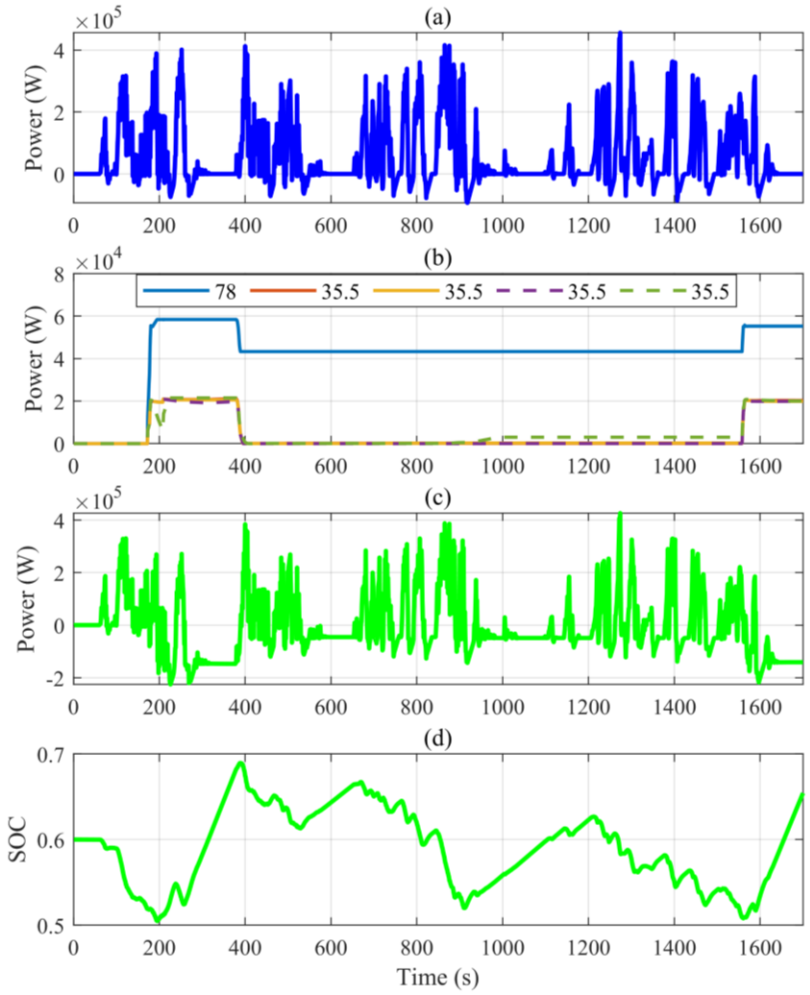

Fig. 3-7. The results corresponding to the five-stack configuration in case study 1: (a) requested power, (b) net output power of FC stacks, (c) battery power, and (d) battery SOC.

3.5.1.3 Validation

To validate the effectiveness of the proposed ISEMS, a comparative analysis is conducted using the configurations proposed in previous studies. Ref. [56] introduces an optimal sizing solution for a single-stack FCS, recommending a 334 kW FC and an 87 kWh battery. In [104], the authors adopt the sizes suggested in [56] and implement them as a four-stack configuration using FC stacks with a 75 kW power rating manufactured by PowerCell Group.

The MPC-based EMS used in this paper is applied to both the reconstructed system based on [104] and the configuration defined in [56]. The resulting performance is then compared against the proposed ISEMS under identical hardware constraints. Fig. 3-8 illustrates the comparative results, where subfigure (a) corresponds to the single-stack configuration of [56], and subfigure (b) presents the four-stack configuration based on [104]. All cost values are presented on a logarithmic scale to enhance visibility across several orders of magnitude.

The results clearly demonstrate the advantages of ISEMS. In both cases, C_{tot} is significantly reduced compared to the referenced strategies. Specifically, in the single-stack scenario, the proposed method results in approximately 68% lower C_{tot} and 69% lower C_{inv}/w compared to [56]. A deeper look at C_{inv}/w reveals that its higher value in [56] is due to two main factors. First, the absolute investment cost in [56] is substantially higher, as shown in the figure. Second, the degradation rate of the FC stack in [56] is also notably higher. In [56], the maximum degradation of the FC stack reaches 0.0043, whereas in the proposed method, it is only 0.0021. This accelerated degradation in [56] implies a shorter expected lifetime for the FC stack, meaning that the investment cost is distributed over fewer mission cycles. Consequently, the share of the investment cost per mission increases, which directly elevates C_{inv}/w.

Similar improvements are observed in the four-stack case, where all costs are lower under ISEMS. In particular, C_{tot} is reduced by nearly 50% compared to [104], while both C_{inv} and C_{inv}/w are also notably lower. Overall, these results confirm that the proposed ISEMS can supply the required load using smaller FC stacks and battery sizes, leading to significant savings in the total system cost, including both operational cost and investment

cost per mission profile. This improvement is attributed to the degradation awareness of the proposed ISEMS, implemented at both the sizing and EMS levels.

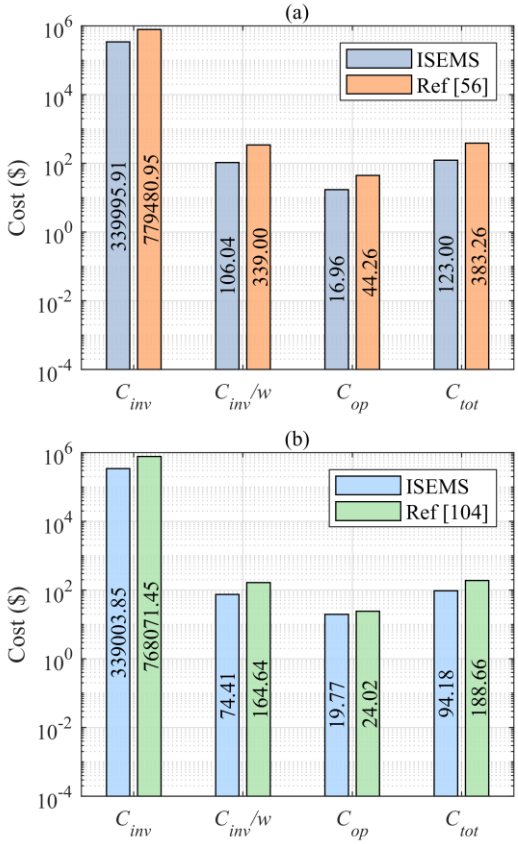

Fig. 3-8. Comparison of cost metrics between ISEMS and previous works: (a) single-stack ([56]), (b) four-stack ([104]).

3.5.1.4 Sensitivity analysis

The performance of the FCS is strongly influenced by the assumptions related to the battery's SOC limits. Modifying the minimum and maximum allowable SOC changes the usable energy capacity of the battery, which directly impacts the distribution of power between the battery and FC stacks. This section evaluates the sensitivity of investment cost, operational cost, and total cost to SOC range assumptions across different FC stack configurations.

As shown in Fig. 3-9a, increasing the SOC window from [0.50–0.70] to [0.20–1.00], with an initial SOC of 0.6, results in a consistent reduction in the investment cost across all FC stack configurations. For instance, C_{inv} in the 1-stack system decreases from 339,995.91 $ to 144,657.16 $ (−57.5%). Similarly, the 2-stack configuration shows a reduction from 349,879.43 $ to 145,021.22 $ (−58.6%), while the 3-stack system drops from 326,121.55 $ to 160,914.97 $ (−50.7%). For the 4-stack, 5-stack, and 6-stack systems, the reductions are from 339,003.85 $ to 130,051.30 $ (−61.6%), from 288,176.38 $ to 148,689.24 $ (−48.4%), and from 272,192.58 $ to 151,252.94 $ (−44.4%), respectively.

The investment cost per mission profile follows the same trend, as shown in Fig. 3-9b. For the narrowest SOC window [0.50–0.70], C_{inv}/w is highest across all configurations, particularly in the 1-stack case (106.04 $), while the corresponding value under the [0.20–1.00] window drops from 106.04 $ to 26.75 $ (−74.8%). Significant declines are also observed in other configurations: from 77.14 $ to 27.10 $ in the 2-stack (−64.9%), from 69.88 $ to 28.64 $ in the 3-stack (−59.0%), and from 74.41 $ to 22.33 $ in the 4-stack (−70.0%). The 5-stack and 6-stack systems also show reductions from 61.62 $ to 22.04 $ and from 63.65 $ to 22.41 $, respectively.

As shown in Fig. 3-9c, the operational cost remains relatively stable across SOC ranges in all configurations. The variations are mostly within a narrow band of ±1 $, confirming that the expansion of the SOC window does not impair the operational cost. A minor increase is seen in some cases, such as the 3-stack configuration, where C_{op} slightly rises from 13.41 $ to 13.81 $, while in others, like the 2-stack case, it decreases from 13.58 $ to 12.53 $. No significant operational deterioration is observed.

The total cost, depicted in Fig. 3-9d, captures the combined effects of investment and operational costs. Broadening the SOC range from [0.50–0.70] to [0.20–1.00] results in substantial reductions across all configurations. In the 1-stack system, C_{tot} drops from 123.00 $ to 40.11 $ (−67.4%). For the 2-stack, 3-stack, and 4-stack cases, reductions are from 90.72 $ to 39.63 $ (−56.3%), 83.29 $ to 42.45 $ (−49.0%), and 94.18 $ to 35.80 $ (−62.0%), respectively. The 5-stack and 6-stack configurations decrease from 79.65 $ to 34.92 $ and from 80.85 $ to 35.41 $, both showing cost reductions of over 55%.

These results demonstrate that wider SOC ranges enable greater exploitation of the battery's energy capacity, allowing the powertrain to rely less on the FC system and consequently reduce its size and cost. The improvement in cost-effectiveness is most prominent when moving from [0.50–0.70] to [0.20–1.00], but the downward trend is also apparent across intermediate SOC ranges. These findings reinforce the importance of careful SOC range selection in hybrid FC-battery design, as it directly impacts sizing decisions and overall economic performance.

It should be noted, however, that the exact magnitude of these cost trends depends on the adopted battery chemistry and its associated energy, power, cost, and aging characteristics.

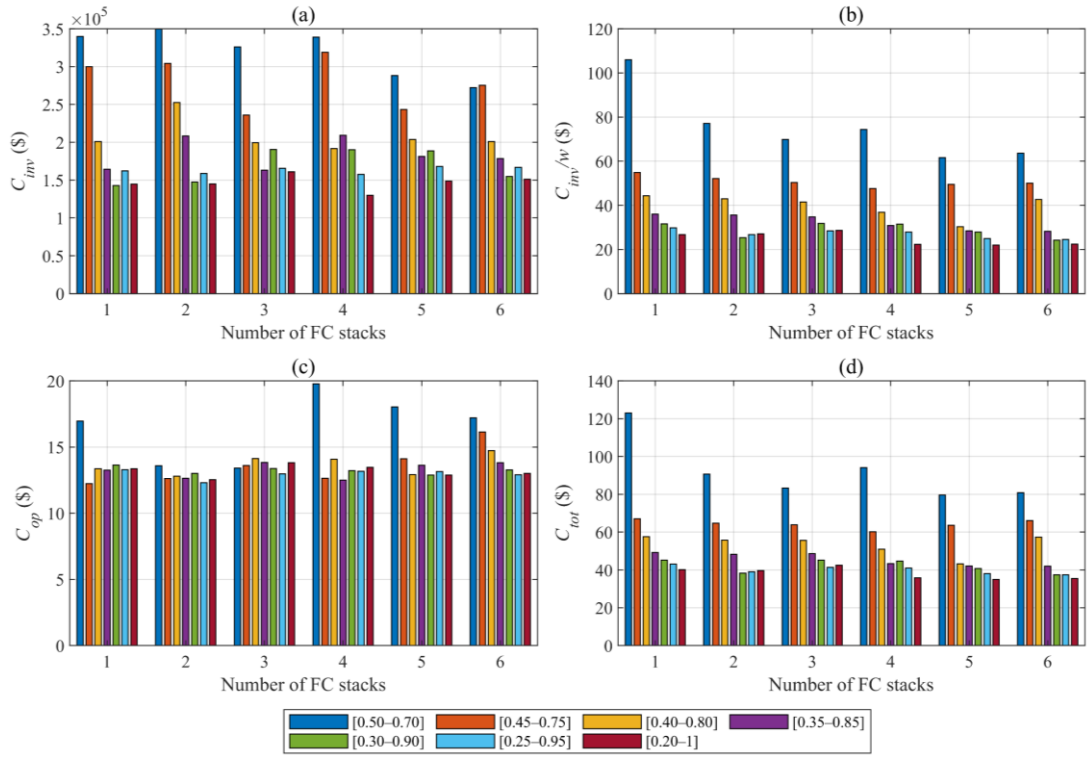

Fig. 3-9. Impact of SOC range on (a) investment cost, (b) investment cost per mission, (c) operational cost, and (d) total cost for different FC stack configurations in case study 1.

3.5.2 Case Study 2

3.5.2.1 Input data

The second case study is based on the experimental setup available at the Hydrogen Research Institute of the Université du Québec à Trois-Rivières, using the multi-stack test bench shown in Fig. 3-10. In this study, the test bench is used to extract performance data from Horizon FC stacks as part of case study 2. The hybrid setup consists of three closed-cathode Horizon PEMFC stacks rated at 1 kW, 2 kW, and 3 kW, connected in a parallel architecture with a lithium-ion battery pack. Each FC stack is connected to a DC-DC converter that boosts the FC output voltage to match the battery pack voltage, which serves as the DC bus. Each FC stack is also monitored by an individual FC controller that collects real-time data, including voltage, current, hydrogen flow rate, and temperature. A DC

electronic load is used to emulate various power demands. A Siemens 1214C PLC sends the power demand to the DC load and provides the reference current signals to the DC-DC converters by adjusting their PWM control. Measurement and control signals are exchanged between the controllers, converters, and PLC, with real-time data acquisition handled via USB and Ethernet connections.

In this case, the proposed ISEMS is employed to determine the optimal sizing of the FC stacks and battery pack, as well as the power distribution between these components. The characterization data for the FC stacks, including polarization curves and hydrogen flow measurements, are experimentally obtained from the available test bench and subsequently integrated into the ISEMS framework. The power demand profile is obtained using the Worldwide harmonized Light-duty vehicles Test Cycle (WLTC) Class 3 driving cycle, which is suitable for evaluating powertrain performance under a wide range of operating conditions.

(a)

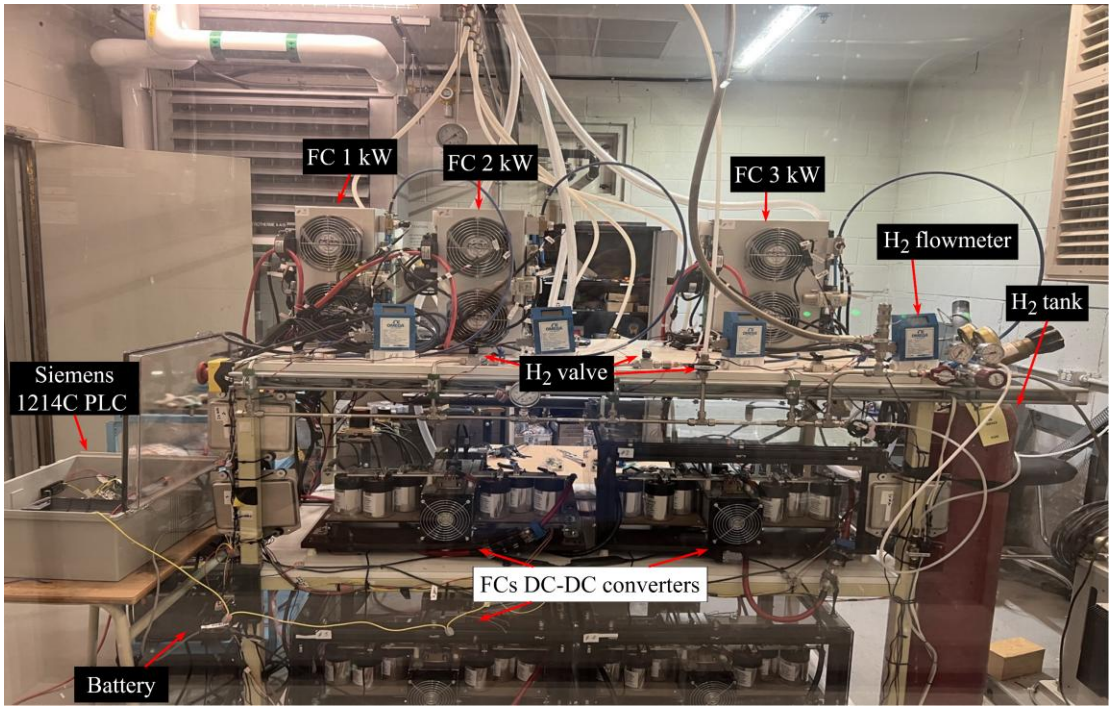

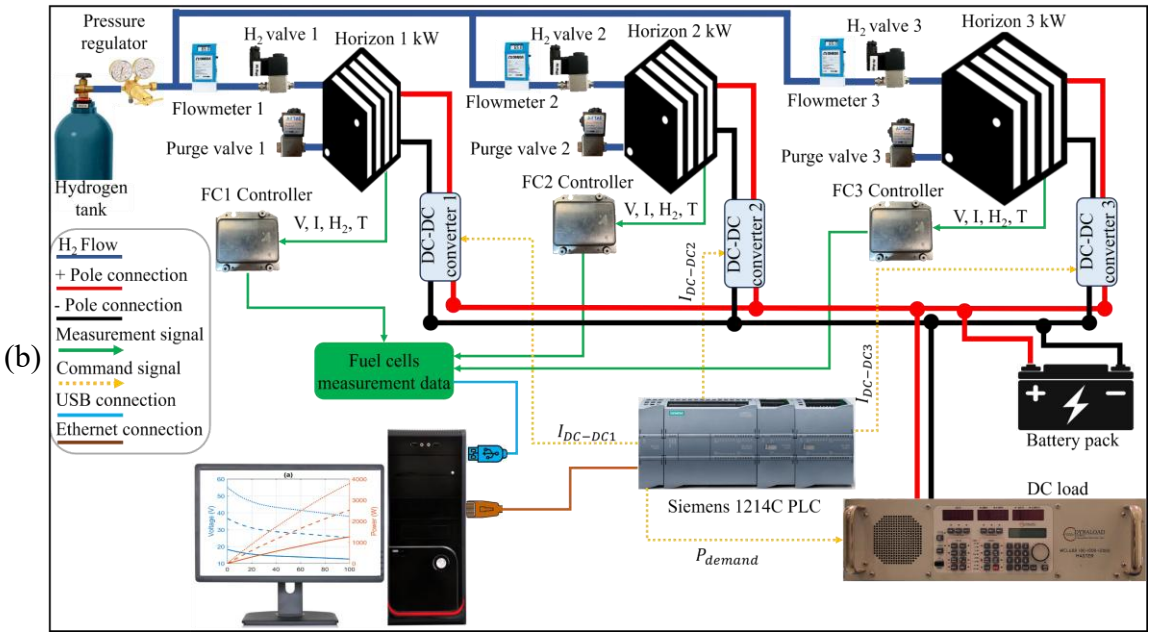

Fig. 3-10. Multi-stack test bench: a) real experimental setup; b) schematic diagram.

In this case study, three commercial FC stack models manufactured by Horizon are considered. These stacks, with rated powers of 1, 2, and 3 kW, are available in the laboratory test bench and have been experimentally characterized. Their specifications are listed in Table 3-9. Fig. 3-11 compares the modeled and experimental performance of the FC stacks at 1 kW, 2 kW, and 3 kW. In Fig. 3-11(a), the polarization curves show the expected voltage drop with increasing load, while a close alignment between the model (solid, dashed, and dotted lines) and the experimental points (square, circle, and star) is observed. The experimental voltages are slightly lower than the modeled values, with a maximum deviation of approximately 3% across all operating points. Fig. 3-11(b) presents the corresponding hydrogen flow rates, which increase with current as predicted by the model. The experimental measurements follow the same trend, showing only minor deviations, and the hydrogen consumption is slightly higher than the modeled predictions, with a maximum difference of about 1%.

Table 3-9. Specifications of FC stack models from Horizon used in case study 2.

Rated power (kW)	No. of cells	Price ($)	Associated Converter Price ($)
1	24	4107.16	1964.59
2	48	5845.58	2796.06
3	72	7655.73	3662.00

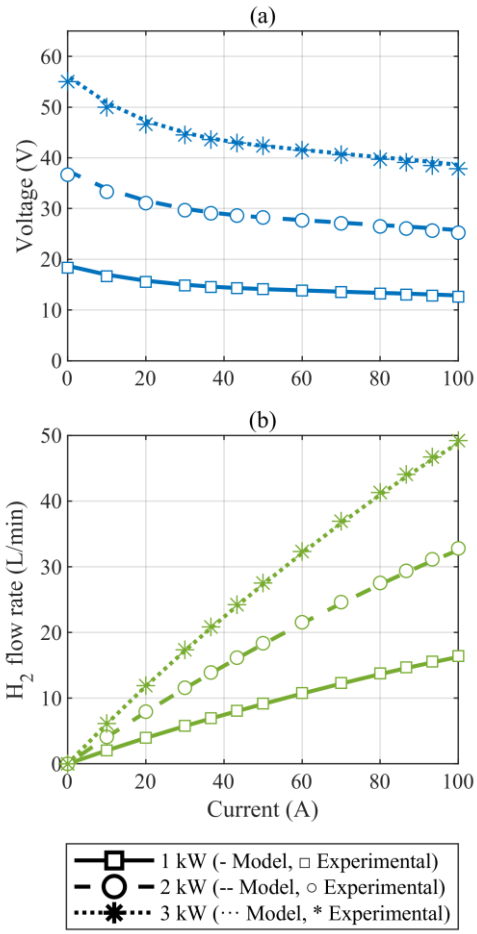

Fig. 3-11. Modeled and experimental (a) polarization curve, and (b) hydrogen flow rate for Horizon FC stacks used in case study 2.

In this case study, a high-power lithium-ion cell produced by Toshiba is selected as the battery technology. The key parameters characterizing this cell are summarized in Table 3-10, with more detailed technical information available in [122]. The battery pack operates within a predefined SOC window of [0.5, 0.7], and the initial SOC is set to 0.6.

Table 3-10. Battery cell parameters utilized in case study 2.

Parameter	Symbol	Value
Capacity (Ah)	Q_{cell}	2.9
Nominal voltage (V)	$V_{cell,nom}$	2.4
Max. power (W)	$P_{cell,max}$	520
Min. power (A)	$P_{cell,min}$	-410

High-power PEMFC stacks suitable for heavy-duty applications are generally not available for laboratory testing due to their high cost. However, the fundamental electrochemical behavior of PEMFCs is scale-independent, and the polarization and efficiency curves of high-power stacks follow the same form as those of low-power stacks, with the main difference being the number of cells connected in series. Therefore, the experimental 1–3 kW stacks effectively capture the stack-level dynamics required for model validation. Moreover, since the primary complexity of HDVs arises from their multi-stack architecture, validating the proposed ISEMS on a multi-stack configuration at laboratory scale ensures direct scalability to HDV-scale systems.

3.5.2.2 Optimal configuration

To evaluate the impact of FC modularity, configurations with 1 to 5 stacks were simulated using the ISEMS framework, which optimized stack selection, battery sizing, and power sharing. As shown in Table 3-11, the single-stack configuration was infeasible under the given mission, unable to meet power demand. Among feasible options, the two-stack setup achieved the lowest total cost ($3.55), driven by a minimal normalized investment cost ($2.95) and low operational cost ($0.60). It employed two 2 kW stacks and a 25s–10p battery, with low FC (0.0017%) and battery (0.0003%) degradation. The three- and four-stack configurations showed nearly identical degradation values and retained the same

battery size but incurred higher total costs of \$4.14 and \$4.72, respectively, due to increased modularity and investment cost, without notable gains in durability. The five-stack setup significantly raised total cost (\$10.80), mainly due to higher investment cost (\$33,208.04) and increased FC degradation (0.0030%), which reduced system life and elevated the normalized investment per mission (\$9.84). Battery degradation remained minimal (0.0003–0.0004%) across all feasible configurations, indicating adequate battery sizing and limited electrochemical stress. Overall, moderate modularity, particularly the two- or three-stack configurations, provided the most cost-effective and durable solution for the evaluated mission profile.

Table 3-11. Optimal configurations from ISEMS for different FC stack counts in case study 2, including costs and degradation levels.

	Optimal configuration		**Costs (\$)**				**Degradations (%)**	
No. of FC stacks	FC stack sizes (kW)	Battery (N_{ser}, N_{par})	C_{inv}	C_{inv}/w	C_{op}	C_{tot}	Max. FCs	Battery
1	-	-	-	-	-	-	-	-
2	2×2	25, 10	17593.71	2.95	0.60	3.55	0.0017	0.0003
3	2×1, 2	25, 10	21095.58	3.54	0.61	4.14	0.0017	0.0003
4	4×1	25, 10	24597.44	4.11	0.61	4.72	0.0017	0.0003
5	4×1, 2	25, 9	33208.04	9.84	0.95	10.80	0.0030	0.0004

Fig. 3-12 illustrates the SOH evolution of FC stacks for 2- to 5-stack configurations in case study 2 under the degradation-aware EMS. Each subplot represents a modularity level, with legends indicating stacks rated powers in kW. Across all configurations, SOH trajectories remain nearly identical, demonstrating the EMS's ability to balance power distribution, even with heterogeneous stacks.

In the 2-stack configuration (Fig. 3-12a), a sharp SOH drop appears around 800 s due to the activation of the 2 kW stacks, after which both units exhibit overlapping degradation profiles. The 3-stack setup (Fig. 3-12b) follows a similar trend, as all SOH trajectories remain closely aligned despite differences in rated power. In the 4-stack configuration (Fig. 3-12c), the SOH curves fully overlap throughout the mission. In the 5-stack configuration (Fig. 3-12d), all SOH trajectories exhibit two distinct degradation steps. These steps correspond to switching phases where stacks are activated dynamically based on system demand. Despite these transitions, the SOH curves remain closely grouped.

Overall, the results confirm that the degradation-aware EMS applies a consistent load balancing strategy that harmonizes stack degradation across different modular configurations. This uniformity in SOH evolution supports effective utilization of available resources and contributes to the long-term durability of the FC system.

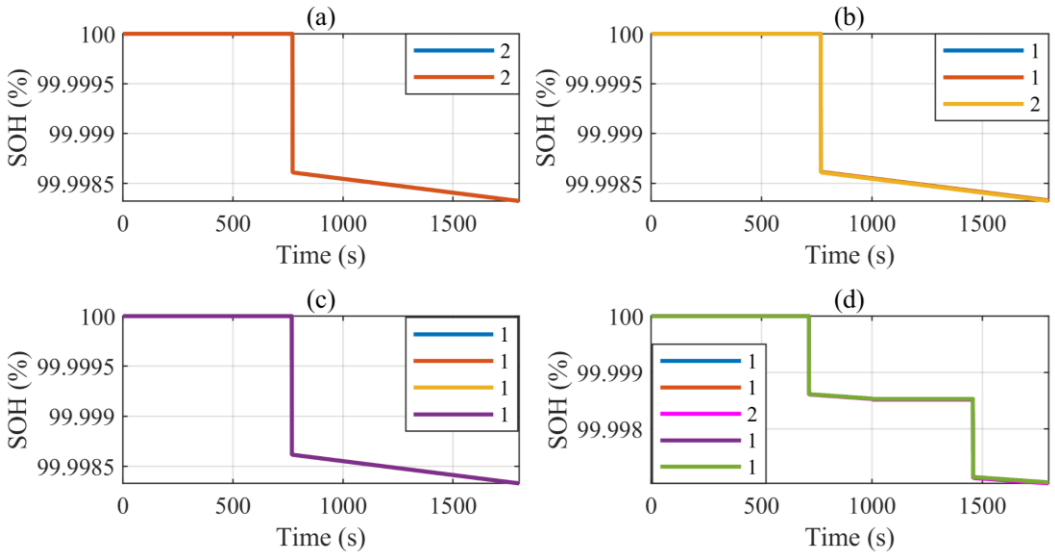

Fig. 3-12. SOH trajectories of FC stacks under degradation-aware EMS for (a) 2-stack, (b) 3-stack, (c) 4-stack, (d) 5-stack configurations in case study 2.

Fig. 3-13 presents results for the dual-stack FC configuration from case study 2, selected due to its lowest total cost among all configurations. Fig. 3-13a depicts a highly

dynamic requested power profile with several sharp peaks, particularly in the latter part of the mission. Fig. 3-13b shows the output power of the two 2 kW FC stacks, which remain off until approximately 770 s, after which they are simultaneously activated and operate continuously at their rated power. The complete overlap of the curves confirms perfectly balanced load sharing. Fig. 3-13c demonstrates that the battery alone supplies power before FC activation and continues to manage rapid transients by absorbing or delivering power as needed. In Fig. 3-13d, the SOC decreases steadily while the FCs are off, followed by a sharp recovery and gradual increase once the FCs are engaged, indicating sustained charging. Overall, the EMS ensures coordinated and continuous FC operation after activation, with the battery supporting transient conditions and maintaining SOC stability throughout the mission.

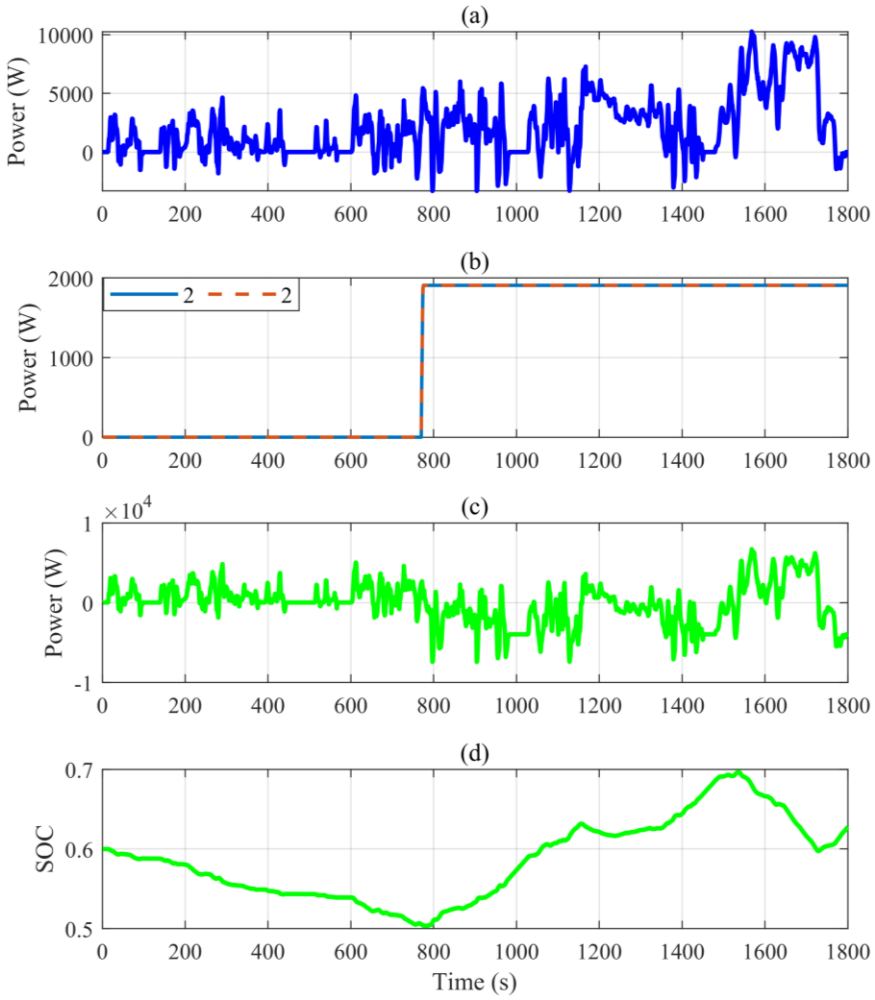

Fig. 3-13. The results corresponding to the dual-stack configuration in case study 2: (a) requested power, (b) net output power of FC stacks, (c) battery power, and (d) battery SOC.

3.5.3 Robustness Against Parameter Variations

The proposed ISEMS framework relies on the profile of the FC polarization and efficiency curves rather than static operating points. In a real-world operational environment, parameters such as temperature, air stoichiometry, pressure, and humidity represent nominal operating conditions that are actively regulated by the balance of plant to maintain the stack within the manufacturer's specified performance window. While minor real-world fluctuations in these variables may cause slight deviations in instantaneous efficiency and polarization curve, they do not alter the fundamental characteristic shape of

the curves used by the optimization algorithm. Consequently, the optimization logic remains valid and robust against these minor transient disturbances. Furthermore, regarding aging variability, previous studies on online parameter identification using Kalman Filters such as [123, 124] have demonstrated that physical degradation manifests primarily as a parametric shift in the polarization curve—specifically, an increase in internal resistance or a drop in open-circuit voltage—rather than a fundamental structural change in the system's behavior. Crucially, in the MPC simulation, this degradation effect is explicitly considered, and the polarization curve is dynamically updated based on the accumulated degradation amount. The proposed ISEMS anticipates these shifts by incorporating EOL conditions directly into the sizing constraints. By optimizing for the worst-case degradation scenario via the weighting factor (w), the resulting system architecture is inherently robust against aging rate variability and parametric uncertainties encountered during long-term operation.

3.6 Conclusion

This paper proposed a degradation-aware ISEMS for MFCSs in HDVs. By embedding degradation models directly into a hybrid GA-MPC framework, the method simultaneously optimized component sizing and power distribution. The key findings are summarized as follows:

Cost and Durability Improvement: In the long-haul truck case study, the proposed approach reduced the total cost by 68% compared to single-stack and by 50% compared to quad-stack configurations from the literature. The optimal five-stack configuration achieved the lowest total cost ($79.65) and extended system lifetime to 2209 hours, significantly outperforming the 1514 hours of the single-stack baseline.

Experimental Validation: Tests using real-world stack data confirmed the method's adaptability. A dual-stack configuration (2 × 2 kW) was identified as the most cost-effective solution ($3.55), offering a projected lifetime of 2984 hours, whereas increasing modularity beyond this point (e.g., five stacks) reduced lifetime due to higher degradation.

Impact of Battery Utilization: Sensitivity analysis demonstrated that widening the battery SOC window (from [0.50–0.70] to [0.20–1.00]) yielded additional cost reductions of up to 67.4%, highlighting the critical role of battery sizing in reducing FC stress.

Overall, the proposed method provides a scalable and durable solution for cost-effective MFCS design and control in HDVs. Future work will consider uncertainty in the requested power profile, investigate system performance under different hybridization factors, and determine optimal component sizes under varying FC and battery price scenarios.

Chapter 4 - Multi-Objective Integrated Sizing–EMS for MFCSs in Aircrafts

This chapter extends the integrated sizing-EMS framework to aircraft through the multi-objective MISEMS formulation. The emphasis is placed on simultaneous cost-weight optimization under demand uncertainty.

4.1 Abstract

A multi-objective integrated sizing and energy management strategy (MISEMS) is presented for aircraft-oriented multi-stack fuel cell systems (MFCSs) under requested power uncertainty. Unlike existing studies, which typically addressed sizing or energy management strategy (EMS) separately for predominantly single-stack architectures and did not jointly optimize cost and weight, this work integrates MFCS sizing and EMS with explicit, simultaneous minimization of total cost and powertrain weight under uncertainty. The framework optimizes degradation-weighted investment and operational cost together with total system weight, while robustness to demand uncertainty is ensured through scenario generation and reduction. The sizing problem is solved using an integer-based NSGA-II, while a nested MPC embedded within the NSGA-II performs EMS and evaluates operational costs. Case studies are conducted using NASA's X-57 Maxwell aircraft and an experimental multi-stack test bench. In case study 1, total cost and total system weight are reduced by 11.8% and 17.6%, respectively, compared to a benchmark from the literature.

Pareto fronts reveal cost–weight trade-offs across one- to four-stack architectures, with limited performance gains beyond intermediate modularity levels. Experimental results validate the feasibility of the optimized configurations and demonstrate effective FC–battery power sharing under practical hardware constraints. The proposed MISEMS provides a systematic and degradation-aware framework for MFCS design and operation in weight-sensitive aircraft applications.

Keywords: proton exchange membrane fuel cell, modular fuel cell system, aeronautic, multi-objective optimization, integrated design–operation framework

4.2 Introduction

The transportation sector remains a major contributor to global greenhouse gas emissions, with aviation exhibiting one of the fastest growth rates among all transport modes [125]. Despite accounting for a relatively small share of total energy-related CO_2 emissions, aviation faces unique decarbonization challenges due to its stringent power-to-weight requirements, long operational lifetimes, and limited flexibility in onboard energy storage [5]. Without significant technological shifts, aviation emissions are projected to surpass pre-pandemic levels in the near term and increase substantially in the coming decades [3].

Several pathways are currently being explored to mitigate aviation emissions. Sustainable aviation fuels (SAFs) offer near-term compatibility with existing aircraft architectures but do not eliminate NO_x emissions or non-CO_2 climate effects, and their long-term sustainability remains debated [126]. Battery-electric propulsion has demonstrated potential for light aircraft; however, its applicability to larger platforms is

constrained by the low specific energy of current battery technologies [127]. Hydrogen-based propulsion has therefore emerged as a promising alternative, either through combustion or via fuel cell (FC) systems. While hydrogen combustion eliminates CO_2 emissions during flight, it still produces NO_x and contrails [128]. In contrast, proton exchange membrane fuel cells (PEMFCs) enable fully electric propulsion with zero local emissions, quiet operation, and modular scalability, making them attractive candidates for hybrid-electric aviation architectures [129].

Despite these advantages, PEMFC systems face intrinsic limitations in aircraft applications, notably limited specific power and slow dynamic response. As a result, practical aircraft implementations typically rely on hybrid architectures combining FC systems with batteries to meet transient power demands [130, 131]. For high-power applications, including aircraft, single-stack FC systems are often insufficient, motivating the use of multi-stack fuel cell systems (MFCSs). By distributing power across multiple stacks, MFCSs improve scalability, fault tolerance, and packaging flexibility, while also enabling more refined control of operating conditions that can reduce degradation and improve efficiency. However, the integration of multiple FC stacks alongside a battery significantly increases system complexity, making appropriate sizing and energy management strategy (EMS) design critical.

Component sizing plays a particularly decisive role in aircraft, where excess mass directly penalizes performance, range, and cost. Undersized systems risk failing to meet power demands, while oversized components increase weight and capital expenditure [32].

Existing sizing studies for hybrid-electric aircraft have largely focused on single-stack FC configurations and have predominantly targeted performance metrics such as range,

endurance, payload, or emissions, often reporting system weight as a byproduct rather than explicitly optimizing it. For example, endurance maximization with a competitive range was addressed in [57], emission reduction under range and climb constraints in [58], and combined range–endurance targets with substantial emission reductions in [59] and [25]. Techno-economic analyses have emphasized cost–performance trade-offs[60], while uncertainty-aware sizing approaches have focused on feasibility under operational constraints [61]. Consequently, the potential benefits of MFCS architectures for aircraft remain largely unexplored from an integrated sizing perspective, particularly with respect to direct powertrain weight minimization. In parallel, research on MFCSs in ground vehicles has shown that increasing the number of stacks and allowing heterogeneous stack sizes can improve efficiency, reduce degradation, and lower operational costs. Differential control of modular FC configurations was investigated in [62], while stack allocation under a fixed total FC capacity was addressed using bi-level [63] or multi-objective [64] optimizations, and operational cost reductions achieved by increasing the number of stacks were reported in [65]. These studies, however, have assumed a fixed total FC capacity and focused on stack allocation or predefined configurations, without jointly optimizing individual stack sizes and battery capacity.

Moreover, treating sizing and EMS design as independent problems has been shown to lead to suboptimal solutions [67], as component sizes fundamentally constrain operational flexibility and control decisions. While integrated sizing and EMS frameworks have been explored for single-stack FC systems in ground applications, no such approach has been proposed for aircraft or for multi-stack architectures. For example, [68] used Toyota Mirai data with MATLAB–SIMULINK modelling to optimize component sizes and power

distribution, extending FC life and lowering hydrogen use. Similar integrated approaches have been used for hybrid ESS optimization [72], and chance-constrained ESS sizing for HDVs [73].

Effective operation of hybrid MFCSs further requires an EMS capable of distributing power among multiple FC stacks and the battery while minimizing hydrogen consumption and component degradation [104, 132, 133]. Although numerous EMSs have been developed for FC–battery hybrid aircraft, these efforts have almost exclusively addressed single-stack systems, employing methods such as model predictive control (MPC), Pontryagin's minimum principle, fuzzy adaptive control, and metaheuristic optimizations [134-140]. Only [141] has considered MFCSs in aircraft, and none has embedded EMS design within an integrated sizing framework.

Additionally, aircraft missions are subject to significant uncertainty in requested power due to atmospheric conditions, operational deviations, and system aging [142, 143]. Ignoring such uncertainty can lead to conservative oversizing or insufficient power margins, underscoring the need for robust, uncertainty-aware design methodologies.

To date, no study has undertaken a comprehensive integration of MFCS sizing and EMS design for aircraft applications with the explicit aim of reducing both total cost and system weight. To address these gaps, this paper proposes a multi-objective integrated sizing and energy management strategy (MISEMS) for aircraft-oriented hybrid MFCSs under power demand uncertainty. The proposed framework simultaneously minimizes total powertrain cost and weight, explicitly accounting for investment costs, operational hydrogen consumption, and degradation of both FC stacks and the battery. Stack number, individual stack sizes, and battery capacity are optimized jointly, while a nested MPC

scheme evaluates operational performance. Power demand uncertainty is incorporated through scenario-based optimization to ensure robust system capability. The effectiveness of the proposed approach is demonstrated through simulation on NASA's X-57 Maxwell aircraft and validated experimentally on a multi-stack test bench.

The main contributions of this work are summarized as follows:

- A multi-objective framework is developed for coordinating the sizing and energy management of multiple FCSs and a battery in aircraft applications, explicitly targeting reductions in both powertrain cost and weight.
- Uncertainty in the requested power profile is incorporated into the optimization process, enabling robust sizing decisions to guarantee the system capability to meet the load under demand variations.
- The sizing and allocation of FC stacks are treated as a single integrated process, rather than being addressed separately with a predefined total FC capacity.

The remainder of the paper is organized as follows. Section II presents the system models, Section III details the proposed MISEMS framework, Section IV discusses the case studies and results, and Section V concludes the paper.

4.3 System Modeling

4.3.1 MFCS Architecture for Aircraft Propulsion

This study adopts a parallel MFCS architecture to enable independent FC stack control and improve redundancy. Each FC stack connects to the DC bus via a unidirectional DC–DC converter, while the ESS uses a bidirectional converter for charge/discharge. Fig. 4-1

illustrates the configuration, and the number of stacks is selected based on application needs.

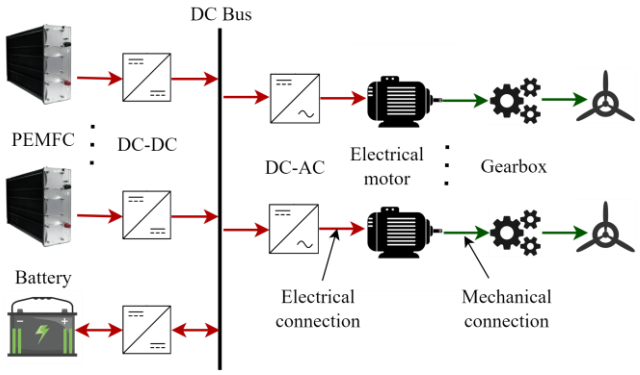

Fig. 4-1. MFCS Powertrain Architecture.

The MFCS is subject to the power-balance condition in (4-1), requiring that the aggregate load demand be fully supplied by the available sources.

$$\sum_{k=1}^{N_{EM}} \frac{P_{EM,k}}{\eta_{C,EM,k}} + P_{Aux} = \sum_{i=1}^{N_{FC}} \eta_{C,FC,i} P_{FC,i} + \eta_{C,bat} P_{bat} \tag{4-1}$$

where $P_{EM,k}$, P_{Aux}, $P_{FC,i}$ and P_{bat} are the powers of the k-th electric motor, auxiliaries of FCs, i-th FC stack, and battery, respectively; $\eta_{C,EM,k}$, $\eta_{C,FC,i}$ and $\eta_{C,bat}$ are their conversion efficiencies; N_{EM} and N_{FC} denote the numbers of electric motors and FCSs.

4.3.2 PEMFC Model

A widely adopted semi-empirical model introduced in [111] represents PEMFC behavior using experimentally identified parameters. In this framework, the voltage of a single cell, V_C, is decomposed into four constituent terms, whose sum yields the cell output.

$$V_C = E_{Nernst} + V_{act} + V_{ohmic} + V_{con} \tag{4-2}$$

where E_{Nernst} is the reversible cell potential, and V_{act}, V_{ohmic}, and V_{con} are losses from activation, ohmic, and concentration effects, whose values can be calculated using the details provided in [111].

The hydrogen consumption of the FC stack is calculated according to the relation presented in (4-3) [55].

$$\dot{m}_{H_2} = 1.05 \times 10^{-8} \frac{P_{FC}}{V_C} \tag{4-3}$$

where $\dot{m}_{H_2}$ denotes the hydrogen mass flow rate ($\mathrm{kg.\,s^{-1}}$) and P_{FC} is the power produced by the FC stack (W).

PEMFC performance degradation is primarily driven by start–stop cycling, time-varying power demand, and prolonged operation at high or low load levels [112]. The degradation percentage is computed via (4-4).

$$Deg_{FC} = \left(k_s n_s + k_f \Delta P_{FC} + k_l t_l + k_h t_h\right) \tag{4-4}$$

where k_s, k_f, k_l, and k_h are the coefficients associated with start–stop cycling, fast load transients, low-power operation, and high-power operation, respectively; their numerical values are provided in [113]. Moreover, n_s denotes the number of start–stop events, ΔP_{FC} quantifies the load variation (W), and t_l and t_h are the durations of low- and high-power operation (h), respectively.

4.3.3 Battery Model

This study employs a lithium-ion ESS to shave peak demand and recover braking energy. The battery is captured with an internal-resistance model, a formulation widely used and validated in EMS research [114]. The operating behavior is specified by equations (4-5)-(4-8).

$$V_t(t) = V_{OC}(t) - I_{bat}(t)R_{bat}(t) \tag{4-5}$$

$$P_{bat}(t) = V_t(t)I_{bat}(t) \tag{4-6}$$

$$I_{bat}(t) = \frac{V_{OC}(t) - \sqrt{V_{OC}(t)^2 - 4R_{bat}(t)P_{bat}(t)}}{2R_{bat}(t)} \tag{4-7}$$

$$SOC(t) = SOC(t_0) - \eta_{bat}\frac{\int_{t_0}^{t} I_{bat}\, dt}{Q_{bat}} \tag{4-8}$$

where V_t, V_{OC}, I_{bat}, R_{bat}, P_{bat}, SOC, η_{bat}, and Q_{bat} are terminal voltage (V), open-circuit voltage (V), battery current (A), internal resistance (Ω), output power (W), state of charge, Coulombic efficiency, and capacity (Ah), respectively.

Battery performance progressively declines with repeated cycling due to irreversible physicochemical changes. Capacity fade is the most obvious sign of this aging process. To quantify it, this study adopts a control-oriented aging model from [115], previously validated in the literature. The framework uses an Arrhenius-type expression to estimate the percentage capacity loss (ΔQ_{cell}) relative to the initial capacity (assumed 100%), following [116], as given by (4-9).

$$\Delta Q_{cell} = B(c)exp\left(\frac{-E_a(c)}{RT}\right)A(c)^z \tag{4-9}$$

where c specifies the c-rate; B denotes a c-rate-dependent Arrhenius prefactor; A denotes the discharged ampere-hour throughput (Ah) and varies with c-rate; R and T stand for the universal gas constant and cell temperature (K); z=0.55 encodes the power-law contribution; and E_a ($\mathrm{J.mol^{-1}}$) is the activation energy, which depends on c-rate and is determined via (4-10).

$$E_a(c) = 31700 - 370.3c \tag{4-10}$$

In vehicle applications, end-of-life (EOL) is conventionally taken as a 20% reduction in usable capacity. Under this criterion, the cumulative discharge throughput (Ah) is obtained from (4-11), and the corresponding number of charge–discharge cycles at EOL is inferred from (4-12) [117].

$$A_{EOL}(c) = \left[\frac{20}{B(c)exp\left(\frac{-E_a(c)}{RT}\right)}\right]^z \tag{4-11}$$

$$N_{EOL}(c) = \frac{A_{EOL}(c)}{Q_{cell}} \tag{4-12}$$

Hence, the battery's SOH and its degradation rate can be defined as follows:

$$SOH_{bat}(t) = 1 - \frac{\int_0^t \left|I_{bat,cell}(t)\right| dt}{2N_{EOL}(c)Q_{cell}} \tag{4-13}$$

$$\dot{SOH}_{bat}(t) = -\frac{\left|I_{bat,cell}(t)\right|}{2N_{EOL}(c)Q_{cell}} \tag{4-14}$$

where $I_{bat,cell}$ denotes the current of a single cell, and the SOH is initialized at 100%.

4.4 MISEMS Framework

Algorithm 1 shows the framework of the MISEMS for MFCSs under power demand uncertainty. The algorithm begins by acquiring all required input data, including available FC models, battery cell specifications, DC-DC converter parameters, the original requested power profile, segment counts (N_{seg}), noise level (δ), preliminary scenario count (M), cluster count (Λ) and user-defined set (A) of desired FCS number (N_{FC}). These parameters establish the design space and constraints for subsequent optimization.

The process continues with scenario generation and reduction: the power profile is segmented, noise is applied to create scenarios, principal component analysis (PCA) reduces dimensionality, and K-means clustering selects representative cases for optimization.

Next, in the sizing optimization level, for each $N_{FC} \in A$, NSGA-II initializes and evolves a population of sizing candidates (S) consistent with the fixed N_{FC}. Each candidate (s) is assessed across all representative scenarios in the EMS optimization level. Here, an MPC-based EMS determines the optimal power distribution for each scenario. Operational cost ($C_{op,\lambda}$), investment cost ($C_{op,\lambda}$), and a degradation-based weight factor (ω_λ) are computed for each scenario, and all system constraints are enforced.

Aggregate metrics, including total cost (C_{tot}) (combining scaled investment and operational costs) and total system weight (W_{tot}), are computed for every sizing candidate under the fixed N_{FC}. The NSGA-II algorithm refines the candidate population through

selection, crossover, mutation, and Pareto ranking; upon meeting the termination criteria for the current N_{FC}, the resulting Pareto-optimal sets of FC models, battery configurations, and their corresponding power profiles are stored, and the procedure is repeated for all $N_{FC} \in A$.

Algorithm 1 MISEMS for MFCSs using NSGA-II and MPC under power demand uncertainty

Require: Available FC models, battery specs, DC-DC converters, original requested power profile, segment count N_{seg}, noise level δ, initial number of scenarios M, cluster count k, user-defined set A of FC systems number N_{FC}

Scenario Generation and Reduction
Divide original power profile into N_{seg} equal-length segments
for each scenario $j = 1, ..., M$ **do**
  for each segment $r = 1, ..., N_{seg}$ **do**
    Sample noise multiplier $\nu_{j,r} \sim \mathcal{U}[1 - \delta, 1 + \delta]$
    Multiply segment r by $\nu_{j,r}$
  end for
  Form scenario j using noise-injected segments
end for
Assemble all scenarios into a scenario matrix
Mean-center scenario matrix
Apply PCA, keep principal components with $\geq 95\%$ variance
Apply K-means clustering in PCA space (Λ clusters)
Extract one representative scenario from each cluster
for each $N_{FC} \in A$ **do**
  Sizing Optimization Level (NSGA-II)
  Initialize population S of sizing variables
  repeat
    EMS Optimization Level
    for each sizing candidate $s \in S$ **do**
      for each representative scenario $\lambda = 1, ..., \Lambda$ **do**
        Execute MPC-based EMS for s under scenario λ
        Compute operational cost $C_{op,\lambda}$, investment cost $C_{inv,\lambda}$, and degradation-based weight factor ω_λ
        Check and enforce system constraints
      end for
      Compute total cost C_{tot}
      Compute total weight W_{tot}
    end for
    Update S using NSGA-II (selection, crossover, mutation, Pareto ranking)
  until termination criteria are met
  Store Pareto-optimal set for this N_{FC} (FC models, battery pack configurations, and optimal power profiles of FCs and battery)
end for

Ensure: For each $N_{FC} \in A$, Pareto-optimal sets of FC models, battery pack configurations, and optimal power profiles of FCs and battery.

4.4.1 Uncertainty Modeling

Requested power demand uncertainty arises from operational changes such as mission rerouting and delays, environmental variability including winds and turbulence, and system influences like payload adjustments and component aging. These sources collectively cause fluctuations in power demand profiles, which this work captures through a systematic scenario generation and reduction process, structured in the following stages:

4.4.1.1 Scenario generation

The power demand profile is segmented into N_{seg} partitions of equal length. Within each segment, a unique noise multiplier ($v_{j,r}$) is independently drawn from a uniform distribution spanning $\mathcal{U}[1-\delta, 1+\delta]$, where $\delta = 0.1$ represents the maximum allowable deviation. This segment-wise noise injection technique introduces localized perturbations while preserving the overall temporal dynamics of the demand profile. Subsequently, M distinct scenarios are synthesized, providing a comprehensive representation of variability. This procedure follows widely accepted Monte Carlo principles employed in power systems uncertainty modeling [144].

4.4.1.2 Dimensionality reduction

The generated scenarios are organized into a matrix and mean-centered to eliminate bias. Principal Component Analysis (PCA) is then utilized to condense the scenario data into fewer dimensions by maintaining enough principal components to cover 95% of the total variance. This process effectively captures the primary modes of variability, streamlining the dataset for computationally efficient clustering and optimization steps [145].

4.4.1.3 Clustering and extraction

Within this reduced-dimensional space, K-means clustering partitions the scenarios into Λ clusters. Each cluster embodies a subset of scenarios that share similar statistical features. Representative scenarios, typically cluster centroids or closest actual members, are extracted for use in further optimization, ensuring a balance between computational feasibility and uncertainty representation [144].

This combined approach closely follows established methods used for managing uncertainty in requested power, providing a reliable and practical way to generate and reduce scenarios.

4.4.2 Sizing Based on NSGA-II

In the proposed framework, the sizing task is solved using NSGA-II, a population-based evolutionary method that efficiently yields well-distributed Pareto solutions with strong convergence and effective constraint handling [146]. NSGA-II searches the FC-battery design space by evolving a population of candidate solutions across generations. Each candidate is encoded as a chromosome of discrete genes specifying FC stack types and battery layout.

The decision vector s encodes the MFCS architecture by selecting specific FC stack models and defining the battery pack layout; correspondingly, the gene structure records: (i) the discrete type index allocated to each FC stack from the admissible FC models, (ii) the number of battery cells arranged in series, and (iii) the number of battery cells arranged in parallel. Each chromosome consists of $N_{FC} + 2$ genes, where N_{FC} is the number of FCSs, and the last two terms specify battery series and parallel cell quantities. For instance,

s = [7, 3, 1, 4, 182, 7] indicates a configuration with four FCSs using stack models 7, 3, 1, and 4, 205 series battery cells, and 8 parallel branches. This compact representation enables efficient evaluation of various FC and battery layouts. Since all vector entries are integers, optimization utilizes an integer-based NSGA-II.

The integer-based NSGA-II generates an initial population randomly within prescribed bounds and evaluates each solution using the nested MPC-based EMS and objective functions for all representative scenarios. Selection, crossover, and mutation are applied for population updates according to Pareto ranking. This iterative process continues until the stopping criterion is met. NSGA-II aims to simultaneously minimize the objective functions, defined as follows:

4.4.2.1 Objective function 1: total cost

The total cost (C_{tot}) for each sizing candidate is computed as the average, across scenarios (Λ), of the weighted sum of investment ($C_{inv,\lambda}$) and operational costs ($C_{op,\lambda}$) in scenario (λ), as defined in (4-15). Investment cost represents the capital expenditure for the selected FC and battery configurations. To reconcile the difference in time scales between short-term operations and long-term investments, a degradation-based weighting factor (ω_λ) is incorporated.

$$C_{tot} = \frac{1}{\Lambda}\sum_{\lambda=1}^{\Lambda}\left(\frac{C_{inv,\lambda}}{\omega_\lambda} + C_{op,\lambda}\right) \tag{4-15}$$

The operational cost is calculated through the EMS and is explained in detail in Section II-C. The investment cost in the scenario λ is defined by (4-16):

$$C_{inv,\lambda} = \sum_{i=1}^{N_{FC}} \left(C_{FCS,i} + C_{C,FC,i}\right) + C_{stg,\lambda} + C_{bat} + C_{C,bat} \tag{4-16}$$

where $C_{FCS,i}$ and $C_{C,FC,i}$ are the costs of *i*th FCS and its converter, $C_{stg,\lambda}$ is the hydrogen storage cost, C_{bat} denotes the battery cost and $C_{C,bat}$ stands for battery converter cost.

The weight ω_λ is obtained by (4-17):

$$\omega_\lambda = \frac{Deg_{FC,per}}{max_i\left(Deg_{FC,i,\lambda}\right)} \quad i\epsilon\{1,..,N_{FC}\} \tag{4-17}$$

where $Deg_{FC,per}$ denotes the maximum permissible FC stack degradation, while $Deg_{FC,i,\lambda}$ represents the degradation of the *i*th stack in the scenario λ. ω_λ reflects the number of mission profiles achievable before the most degraded stack reaches its EOL, and $C_{inv,\lambda}/\omega_\lambda$ in (4-15) gives the investment cost attributable to a single mission profile in each scenario.

4.4.2.2 Objective function 2: total weight

The total weight (W_{tot}) of the powertrain system can be calculated as (4-18):

$$W_{tot} = W_{bat} + W_{C,bat} + W_{comp} + W_{cooling} + \sum_{i=1}^{N_{FC}} \left(W_{FC,i} + W_{C,FC,i}\right) + \frac{1}{\Lambda} \sum_{\lambda=1}^{\Lambda} W_{stg,\lambda} \tag{4-18}$$

where $W_{bat}, W_{C,bat}, W_{comp}, W_{cooling}, W_{FC,i}, W_{C,FC,i}$, and $W_{stg,\lambda}$ represent the weights of the battery, battery converter, compressor, cooling system, the ith FC stack, the ith FC stack converter, and the hydrogen storage in the scenario λ, respectively. These weights are calculated using the component unit weights in Table 4-1, and $W_{FC,i}$ for different FC models is taken from [120, 121].

Table 4-1. Unit weight parameters of FCHEV powertrain components [59, 122, 147-149]

Parameter	Description	Value
w_{bat}	Battery unit weight (kg/kWh)	21.5
$w_{C,bat}$	Battery DC/DC converter unit weight (kg/kW)	0.05
w_{comp}	Compressor unit weight (kg/kW)	0.97
$w_{cooling}$	Cooling system unit weight (kg/kW)	0.8
$w_{C,FC}$	FC DC/DC converter unit weight (kg/kW)	0.05
w_{stg}	H2 storage system unit weight (kg/kg-H2)	5.6

The sizing problem is constrained by (4-19):

$$\begin{cases} s_i \in \{1,2,\dots,N_{FC,models}\} \quad \forall i = 1,\dots,N_{FC} \\ N_{ser,min} \le N_{ser} \le N_{ser,max} \\ N_{par,min} \le N_{par} \le N_{par,max} \end{cases} \tag{4-19}$$

where $N_{FC,models}$ denotes the total available FC stack models. The lower bounds $N_{ser,min}$ and $N_{par,min}$ define the minimum permitted battery cell counts in series and parallel, while $N_{ser,max}$ and $N_{par,max}$ set the corresponding maxima, all determined by the voltage requirements imposed by the problem constraints.

4.4.3 MPC-based EMS

The EMS, built on MPC, serves as the inner loop of the MISEMS framework. For each sizing option s, the MPC evaluates $C_{op,\lambda}$ by optimizing power distribution between FCSs and the battery over a moving prediction horizon. Based on the receding horizon method,

the controller applies only the first input at each step and re-optimizes at the next step using the latest measurements.

The system dynamics are written in discrete-time state-space form as shown in (4-20).

$$\begin{cases} \Delta x(t+1) = A\Delta x(t) + B\Delta u(t) + E\Delta d(t) \\ \Delta x(t) = \Delta SOC(t) = (SOC(t) - SOC(t-1))/\Delta t \\ \Delta u(t) = \Delta P_{FC}(t) = (P_{FC}(t) - P_{FC}(t-1))/\Delta t \\ \Delta d(t) = \Delta P_{req}(t) = (P_{req}(t) - P_{req}(t-1))/\Delta t \end{cases} \tag{4-20}$$

where the state variable x denotes the battery SOC, the control variable u represents the increment in FC power, and the disturbance d corresponds to the requested power at the DC-bus.

The $C_{op,\lambda}$ can be obtained using (4-21):

$$C_{op,\lambda} = \sum_{t=1}^{T} \left[C_{H_2,\lambda}(t) + C_{Deg,FC,\lambda}(t) + C_{Deg,bat,\lambda}(t) \right] + C_{H_2,\Delta SOC,\lambda} \tag{4-21}$$

where $C_{H_2,\lambda}, C_{Deg,FC,\lambda}, C_{Deg,bat,\lambda}$ and $C_{H_2,\Delta SOC,\lambda}$ are the costs of used hydrogen, FCSs degradation, battery degradation and hydrogen-equivalent terminal SOC deviation, and they can be calculated as (4-22)-(4-26):

$$C_{H_2}(t) = c_{H_2} \sum_{p=0}^{P_h} \sum_{i=1}^{N_{FC}} \dot{m}_{H_2,i}(t+p) \tag{4-22}$$

$$C_{Deg,FCS}(t) = \sum_{p=0}^{P_h} \sum_{i=1}^{N_{FC}} \frac{C_{FCS,i} Deg_{FC,i}(t+p)}{SOH_{FC,i}(t+p-1)} \tag{4-23}$$

$$SOH_{FC,i}(t) = 1 - \sum_{q=1}^{t-1} Deg_{FC,i}(q) \tag{4-24}$$

$$C_{Deg,bat}(t) = C_{bat} \sum_{p=0}^{P_h} \dot{SOH}_{bat}(t+p) \tag{4-25}$$

$$C_{H_2,\Delta SOC} = c_{H_2}.\frac{(SOC(t_0) - SOC(t_f)).Q_{bat}.V_{bat.nom}}{\eta_{bat}.\eta_{FC}.LHV_{H_2}} \tag{4-26}$$

In (4-22), the hydrogen cost is obtained based on the cost of hydrogen ($c_{H_2=}0.004\ \$.\mathrm{g}^{-1}$) and the amount of consumed hydrogen by the FCSs in the prediction horizon P_h.

The degradation cost of FCSs in (4-23) is defined over the prediction horizon by summing, across all FCSs, each FCS's cost multiplied by the related FC stack degradation, normalized by the maximum permitted degradation and weighted by an SOH-based penalty implemented as $1/SOH_{FC,i}$. This weight increases the cost share of lower-SOH stacks, steering the strategy toward load allocations that protect the durability of the FCSs, and it can be calculated as (4-24).

Similarly, in (4-25), the battery degradation cost is obtained by accumulating the battery degradation rate over the prediction horizon, dividing by the permitted degradation, and then multiplying by the battery price to convert that fractional wear into a monetary term.

Since initial SOC ($SOC(t_0)$) and final SOC ($SOC(t_f)$) may differ, fair comparison between cases must account for the net battery energy gap; thus, (4-26) includes a term that

converts the SOC change into an hydrogen-equivalent cost. In this equation, LHV_{H_2} denotes hydrogen lower heating value.

The operational constraints of the MFCS are specified in (4-27)

$$\begin{cases} SOC_{min} \le SOC(t+p) \le SOC_{max} \\ P_{bat,min} \le P_{bat}(t+p) \le P_{bat,max} \\ P_{FC,i,min} \le P_{FC,i}(t+p) \le P_{FC,i,max} \\ P_{FC,i,min} \le u_{FC,i}(t+p) \le P_{FC,i,max} \\ \Delta P_{FC,i,min} \le \Delta u_{FC,i}(t+p) \le \Delta P_{FC,i,max} \end{cases} \tag{4-27}$$

where, $p \in \{1,2,\dots,P_h\}$, and the allowable lower and upper limits for each state and control variable are indicated by the subscripts “min” and “max.”

4.5 Results

The effectiveness of the proposed MISEMS is evaluated by simulation in this section. Two case studies are selected for validation. In the first case, MISEMS determines the optimal configuration of FC stacks and battery pack size for an aircraft, and the resulting setup is compared with the results of the configuration reported in the literature. In the second case, FC stacks from the Hydrogen Research Institute of the Université du Québec à Trois-Rivières are incorporated to identify the optimal configuration, utilizing experimentally measured stack characteristics within the MISEMS framework. All simulations operate in MATLAB R2024a on a server featuring a 16-core 2.4 GHz processor, with 4 GB of RAM allocated per core.

4.5.1 Case Study 1

The aircraft selected for this case is NASA's X-57 Maxwell [90]. Fig. 4-2 displays both the original power demand profile and four scenarios generated to simulate load uncertainty in the system. Nine off-the-shelf FC stack models from PowerCell Group, with rated powers of 3, 6.5, 10, 26, 35.5, 78, 95, 119, and 129 kW, were utilized. Further technical details can be found in [120, 121]. A high-power lithium-ion cell from Toshiba is utilized, featuring a capacity of 10 Ah, nominal voltage of 2.4 V, maximum power of 1800 W, and minimum power of -1500 W. The SOC of the battery pack is considered to range between 0.4 and 0.8, with an initial value of 0.6. Comprehensive specifications are provided in [122].

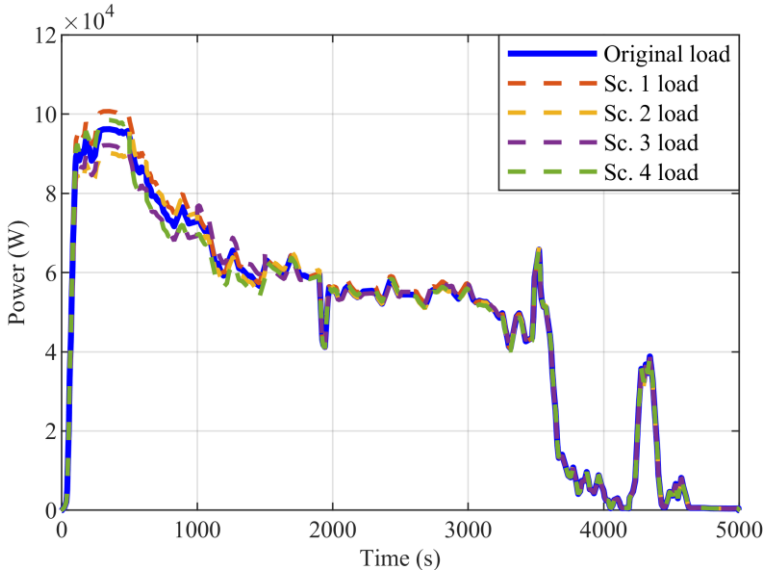

Fig. 4-2. Original and various scenarios requested loads.

Fig. 4-3 presents the Pareto fronts obtained for configurations with one to four FC stacks ($N_{FC} = 1, 2, 3, 4$), where total cost and total weight serve as the two objective functions. Each curve represents the trade-off frontier generated by the MISEMS framework under power-demand uncertainty. As observed, using multi-stack structure

shifts the Pareto front toward lower cost and weight regions, demonstrating the advantages of modular architectures in improving system performance. The single-stack configuration shows the highest cost and weight due to limited architecture flexibility and higher degradation rates. As the number of FCSs increases, enhanced power distribution among stacks reduces hydrogen consumption and component stress, yielding better cost–weight trade-offs. However, the improvement becomes marginal beyond three stacks, as the additional converters and balance-of-plant components increase the total cost and weight.

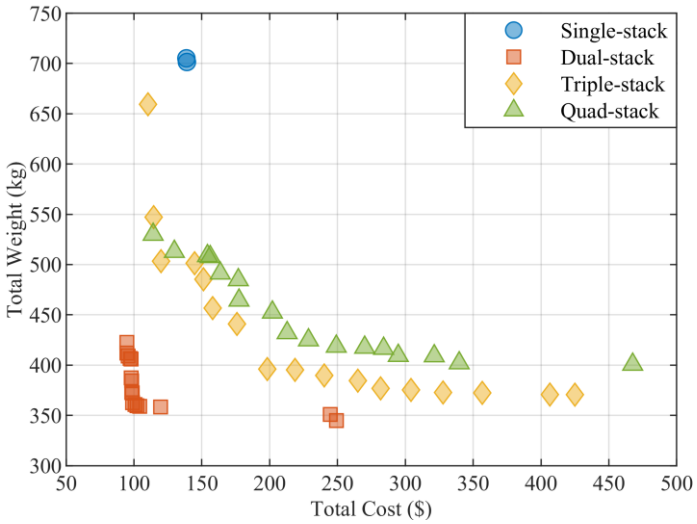

Fig. 4-3. Pareto fronts for configurations with one to four FCSs in case study 1.

The configurations corresponding to the minimum cost, minimum weight, and the best compromise solution (BCS) are summarized in Table 4-2. The BCS is determined using the distance-to-ideal-point method, in which the Pareto-optimal solution closest to the ideal (utopia) point is selected. The distance is calculated through a normalized Euclidean metric based on the objective functions, ensuring an equitable balance between cost and weight. It should be noted that the bar notation represents average values computed over all scenarios. In the transition from the minimum cost to the minimum weight region, the MISEMS reduces the battery capacity to minimize system mass, as the battery possesses a much

lower energy density than FC and therefore contributes more significantly to the total weight. The smaller battery limits the power-buffering capability, forcing the FCSs to supply more dynamic power variations. This operating condition accelerates FC stacks' degradation, which increases the $\overline{C_{op}}$ through higher degradation-related expenses. Although the $\overline{C_{inv}}$ decreases due to smaller battery and converter sizes, $\overline{C_{inv/\omega}}$ rises because ω (indicator of the effective lifetime of the FCSs) diminishes under higher degradation. Consequently, C_{tot} increases due to the combined rise in $\overline{C_{op}}$ and $\overline{C_{inv/\omega}}$, despite the reduction in initial investment.

Table 4-2. Optimal configurations of MISEMS for different numbers of FC systems in case study 1.

No. of FCSs	Solution type	Optimal configuration		Costs ($)				W_{tot} (kg)	$\overline{Deg_{FC}^{max}}$ (%)
		FC (kW)	Battery (kWh)	$\overline{C_{op}}$	$\overline{C_{inv}}$	$\overline{C_{inv/\omega}}$	C_{tot}		
1	Min. cost	129	17.06	57.05	273292.82	81.59	138.64	705.11	0.0030
	Min. weight	129	16.92	57.34	272186.85	81.68	139.01	701.50	0.0030
2	Min. cost	78, 78	3.50	51.51	198660.59	43.27	94.77	422.62	0.0022
	BCS	78, 78	0.96	57.57	179126.09	46.66	104.23	359.00	0.0026
	Min. weight	119, 26	0.96	98.88	161197.50	150.35	249.23	344.84	0.0093
3	Min. cost	119, 35.5, 26	10.30	52.70	264154.23	57.64	110.34	659.44	0.0022
	BCS	78, 35.5, 35.5	1.97	86.19	164012.37	112.06	198.25	396.07	0.0068
	Min. weight	78, 35.5, 35.5	0.96	156.90	156265.32	268.05	424.95	370.61	0.0172
4	Min. cost	78, 26, 26, 26	6.43	54.99	203982.62	59.14	114.13	529.89	0.0029
	BCS	78, 35.5, 26, 10	3.02	90.72	172143.21	122.14	212.86	432.06	0.0071
	Min. weight	78, 35.5, 26, 10	1.78	161.58	162554.40	305.96	467.54	400.64	0.0188

Fig. 4-4 illustrates the SOH evolution of FC stacks under the most severe degradation scenario. In each configuration, the stacks exhibit nearly identical degradation rates, confirming that the degradation-aware EMS effectively balances operating conditions and prevents unequal aging among stacks. Among all configurations, the two-stack system experiences the lowest overall degradation, demonstrating the most favorable durability performance.

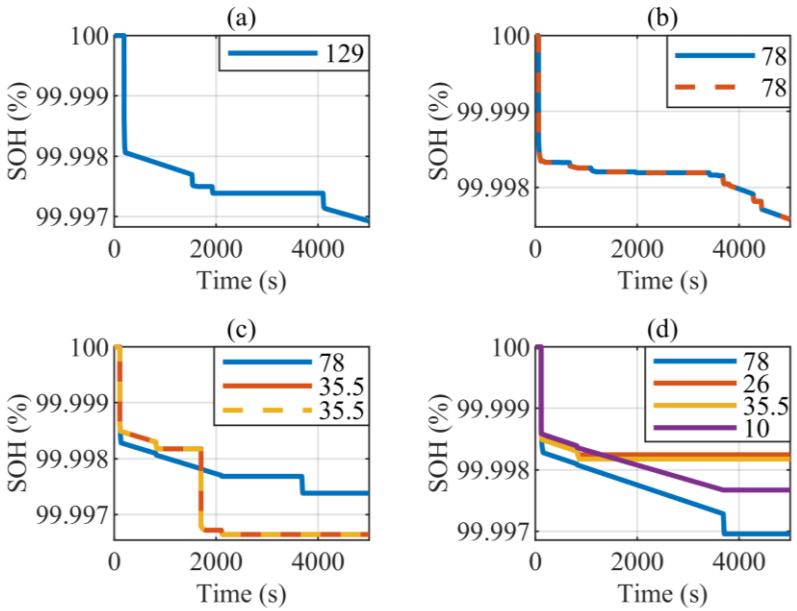

Fig. 4-4. FC stacks SOH trajectories of BCS for (a) 1-stack, (b) 2-stack, (c) 3-stack, and (d) 4-stack configurations in case study 1 and scenario 1.

Fig. 4-5 presents MPC-based EMS results for the two-stack configuration in case study 1, scenario 1. As shown in (a), the requested power exhibits significant variability with several peaks. In (b), the two FCSs share the load effectively, maintaining balanced power delivery without overloading either stack. The battery response in (c) smooths rapid power fluctuations, supplying or absorbing energy to stabilize the net output power. The SOC profile in (d) remains within acceptable limits, confirming that the EMS effectively coordinates FC and battery operation to ensure power balance and system stability.

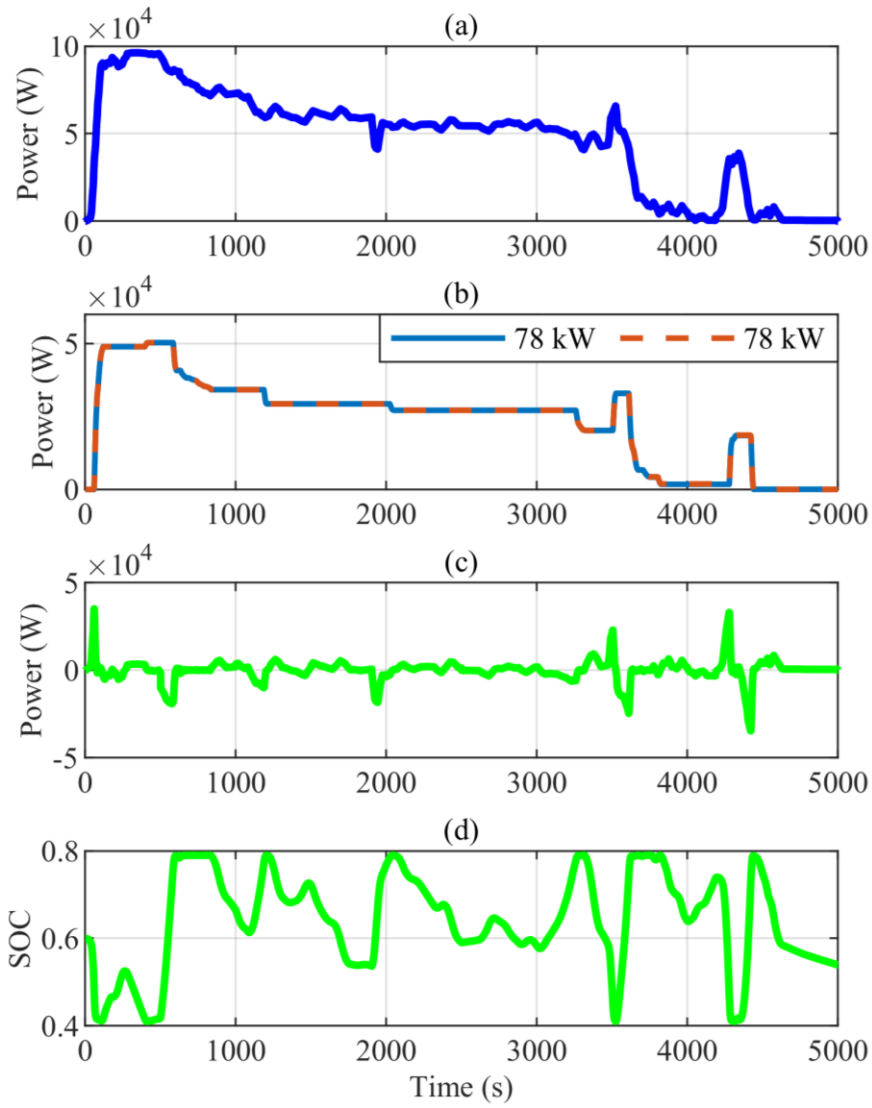

Fig. 4-5. MPC-based EMS results of 2-stack configuration in case study 1 under scenario 1: (a) requested power, (b) net output power of FC stacks, (c) battery power, and (d) battery SOC.

To validate the proposed MISEMS framework, its performance is compared with the NASA's X-57 aircraft reported in [90], which employed a single 100 kW FC and a 25 kWh battery. Fig. 4-6(a) presents a normalized comparison ofthe main performance indicators with all values normalized to [90], while Fig. 4-6(b) quantifies the percentage reductions achieved by MISEMS. Numerically, MISEMS reduces the total cost from 157.12 $ to 138.64 $, representing an improvement of 11.8%, and lowers the investment cost from 319.21 k$ to 273.29 k$ (14.4% reduction). The operational cost decreases from 58.55 $ to

57.05 $ (2.6% reduction). Meanwhile, the total weight declines from 855.63 kg to 705.11 kg, corresponding to a 17.6% reduction. These simultaneous cost and weight improvements confirm that the integrated sizing and EMS optimization, enhanced by degradation-aware considerations in both layers, leads to a more cost-efficient and lightweight configuration compared with the baseline design.

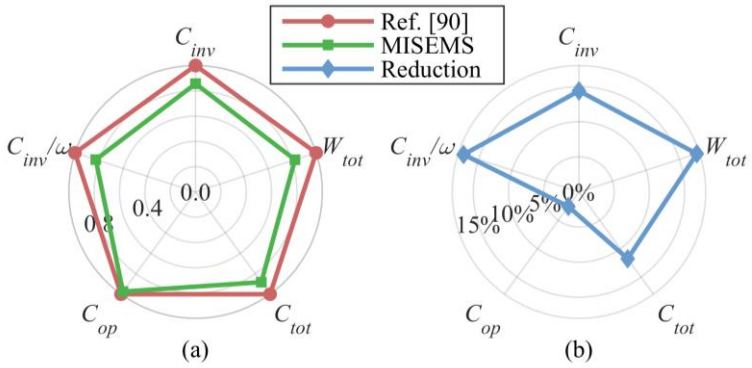

Fig. 4-6. Comparison between the proposed MISEMS and Ref. [90]: (a) normalized values, (b) corresponding reduction percentages.

4.5.2 Case Study 2

The second case study utilizes the Hydrogen Research Institute's multi-stack test bench at the Université du Québec à Trois-Rivières (Fig. 4-7) to experimentally characterize Horizon PEMFC stacks. The setup comprises three closed-cathode stacks rated at 1, 2, and 3 kW, connected in parallel with a lithium-ion battery pack through individual DC–DC converters that boost the stack voltages to the common DC bus. Each stack is supervised by an independent controller measuring voltage, current, hydrogen flow, and temperature in real time. A programmable DC electronic load emulates the demanded power, while a Siemens 1214C PLC governs operation by generating PWM-based reference currents for the converters and transmitting load commands. Data exchange among the PLC,

converters, and controllers occurs via USB and Ethernet for synchronized measurement and control.

(a)

(b)

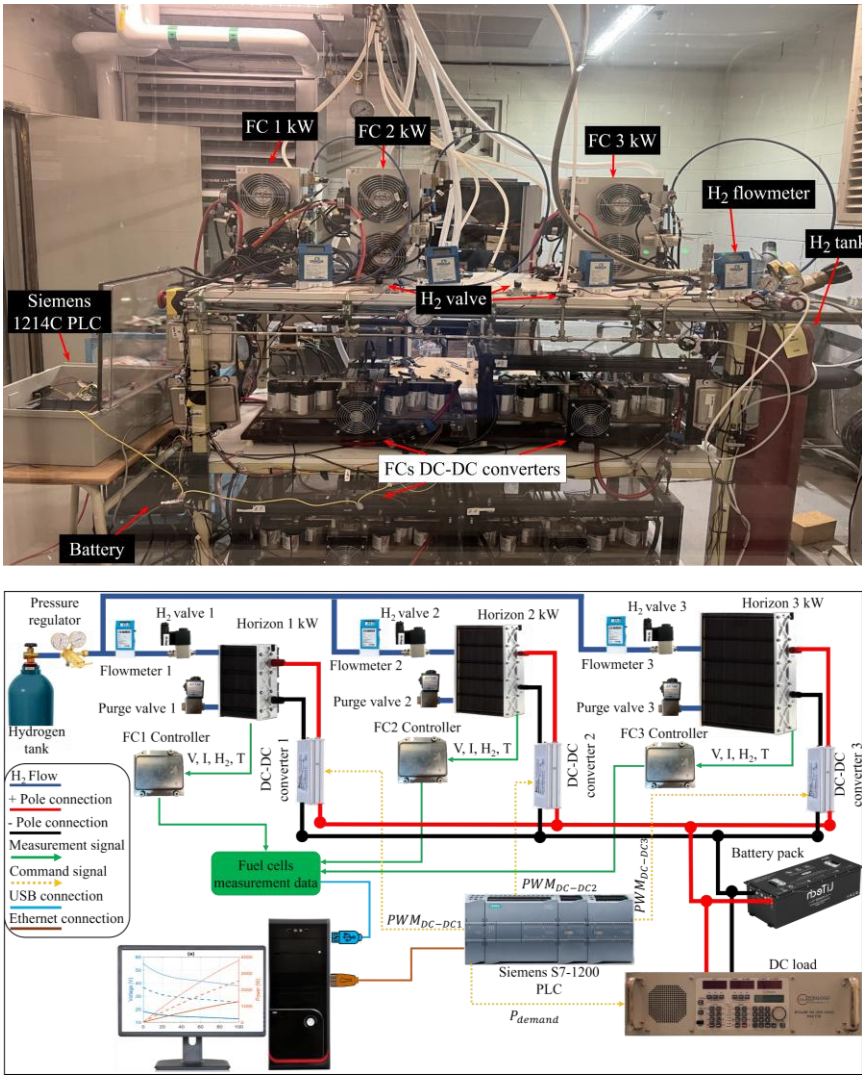

Fig. 4-7. Multi-stack test bench: (a) experimental setup and (b) schematic layout.

Experimental polarization and hydrogen flow data acquired from the test bench are integrated into the MISEMS model to ensure realistic performance representation. The requested power is obtained by scaling the Case Study 1 load profile down by 20, preserving its temporal characteristics while reducing its magnitude. The stacks available

on the test bench have been experimentally characterized, and their polarization, power–current, and hydrogen flow rate characteristics are depicted in Fig. 4-8.

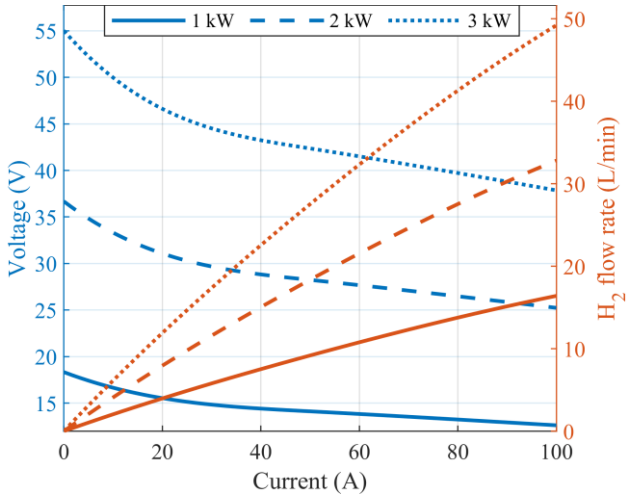

Fig. 4-8. Polarization and hydrogen flow rate curves for Horizon FC stacks used in case study 2.

In this case study, a high-power lithium-ion cell manufactured by Toshiba is adopted as the battery technology. The cell has a nominal voltage of 2.4 V and a capacity of 2.9 Ah. Additional technical specifications are provided in [122].

Fig. 4-9 shows the Pareto fronts for the dual-, triple-, and quad-stack configurations, with total cost and total weight as the optimization objectives. The single-stack setup was infeasible since it could not satisfy the required power demand. Feasible solutions span total weights from 38.80 kg to 87.30 kg and costs between 5.81 $ and 28.15 $. The triple-stack configuration yields the lightest system but the most expensive one, whereas the dual-stack achieves the lowest cost. As observed, all feasible configurations exhibit comparable cost–weight ranges, indicating that increasing the number of stacks does not lead to a clear improvement in this case. In case study 2, the configurations associated with the minimum-cost, BCS, and minimum-weight solutions for systems with two to four FCSs are reported in Table 4-3. In contrast to case study 1, the battery capacity remains at its minimum

allowable value for almost all configurations, indicating that further weight reduction through battery downsizing is not feasible. Consequently, the transition from the minimum-cost solution toward the minimum-weight solution is primarily achieved through modifications in the FC stack configuration rather than through changes in battery capacity. Specifically, minimizing the total system weight favors the selection of FC stacks with lower rated power. However, this choice forces the smaller FC stacks to supply the same fluctuations in the load demand, leading to increased degradation in the FC stacks. As a result, the FC stacks are driven to operate under more demanding conditions, leading to increased degradation. This effect is reflected in the higher values of $\overline{C_{inv/\omega}}$ and consequently C_{tot} for the minimum-weight solutions. This outcome highlights a pronounced trade-off between cost and weight in case study 2, where weight minimization is achieved at the expense of FC durability and total cost, rather than through battery size reduction.

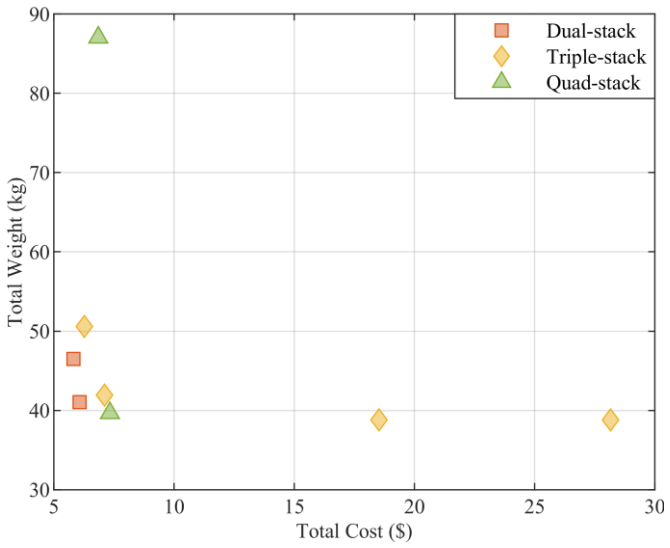

Fig. 4-9. Pareto fronts for configurations with one to four FCSs in case study 2.

Table 4-3. Optimal configurations of MISEMS for different numbers of FC systems in case study 2.

No. of FCSs	Solution type	Optimal configuration		Costs ($)				W_{tot} (kg)	$\overline{Deg_{FC}^{max}}$ (%)
		FC (kW)	Battery (kWh)	$\overline{C_{op}}$	$\overline{C_{inv}}$	$\overline{C_{inv/\omega}}$	C_{tot}		
2	Min. cost	3, 3	0.17	2.27	22710.25	3.54	5.81	46.49	0.0016
	Min. weight	2, 3	0.17	2.31	20035.50	3.76	6.07	41.04	0.0019
3	Min. cost	2, 2, 2	0.17	2.26	25999.66	4.00	6.27	50.59	0.0015
	BCS	1, 2, 2	0.17	2.21	23430.92	4.90	7.10	41.93	0.0021
	Min. weight	1, 1, 3	0.17	4.08	23539.14	24.07	28.15	38.80	0.0102
4	Min. cost	1, 2, 2, 2	1.57	2.32	32320.93	4.53	6.85	87.03	0.0014
	Min. weight	1, 1, 1, 2	0.17	2.31	26933.72	5.02	7.33	39.66	0.0019

Fig. 4-10 shows the experimental EMS results for the two-stack configuration corresponding to the minimum-weight solution on the Pareto front, selected due to its availability in the testbench. The requested power in (a) exhibits substantial variability with several high-demand intervals. As shown in (b), the two stacks deliver power according to their ratings, maintaining stable operation without severe fluctuation in the stacks' power. The battery response in (c) compensates for fast transients, smoothing rapid fluctuations that the stacks cannot track. The resulting SOC trajectory in (d) remains within allowable limits, confirming that the EMS achieves coordinated FC–battery operation under real hardware conditions.

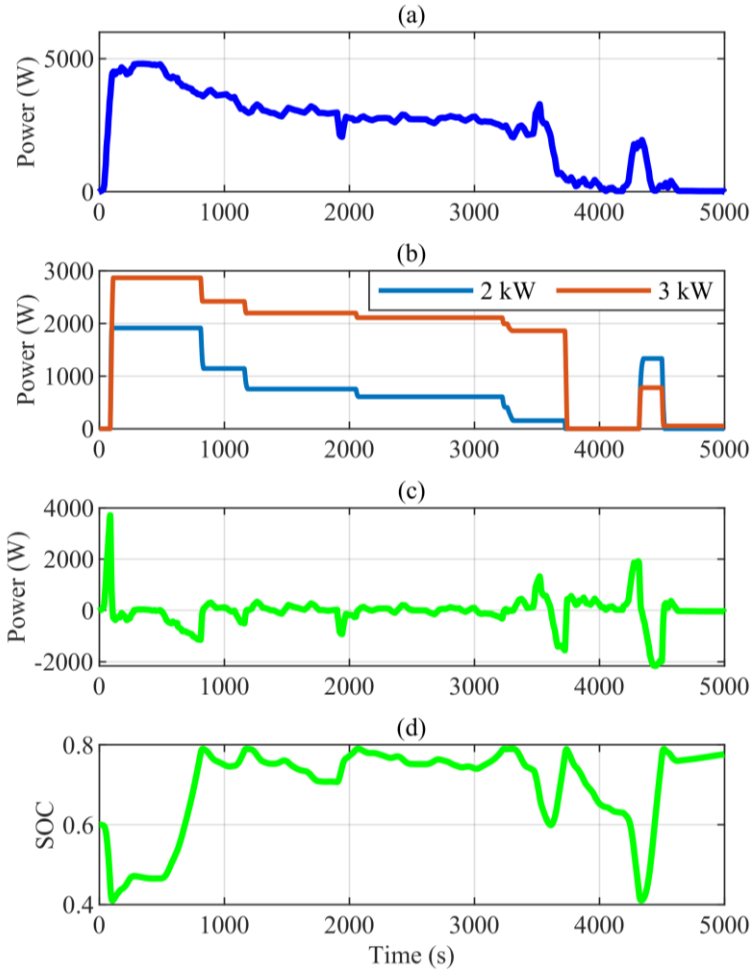

Fig. 4-10. MPC-based EMS experimental results of 2-stack configuration in case study 2 under scenario 1: (a) requested power, (b) net output power of FC stacks, (c) battery power, and (d) battery SOC.

4.6 Conclusion

This work addressed a fundamental gap in the literature by jointly investigating the sizing and energy management of aircraft-oriented MFCSs with explicit consideration of both total cost and total system weight. Unlike existing studies that focus on single-stack architectures, predefined FC capacities, or sequential design approaches, the proposed MISEMS enables a unified exploration of architectural and operational decisions for MFCS-based hybrid powertrains under power-demand uncertainty. An integer-based NSGA-II was employed to perform the multi-objective sizing of the MFCS architecture,

enabling systematic exploration of discrete design configurations and explicit characterization of cost–weight trade-offs. A nested MPC was used as the EMS, ensuring that each candidate design is evaluated under realistic operational constraints and degradation-aware power allocation.

The results demonstrated that MFCS modularity plays a decisive role in shaping cost–weight trade-offs in aircraft applications. While additional stacks improve load-sharing capability and operational flexibility, the associated increase in conversion hardware and balance-of-plant mass limits the achievable benefits. Consequently, the optimal configurations consistently emerged at intermediate levels of modularity, highlighting that neither minimal nor maximal stack counts are desirable when both cost and weight are considered simultaneously. Battery sizing was shown to strongly influence these trends, as reductions in battery capacity decrease system weight but impose higher dynamic stress on FC stacks, increasing degradation-related costs.

By embedding degradation models and uncertainty handling directly into the sizing and EMS layers, the proposed framework captured interactions that are overlooked in conventional design methodologies. The obtained cost and weight reductions relative to the benchmark configuration confirm the importance of integrated and degradation-aware optimization for aircraft powertrains. Experimental validation further verified that the identified configurations are practically feasible and that coordinated FC–battery power sharing can be achieved under real hardware constraints.

Overall, this study establishes a systematic methodology for MFCS design in weight-sensitive aircraft applications and provides quantitative insight into the interplay between

modularity, battery utilization, cost, and durability, thereby supporting informed architectural decisions for future hybrid-electric aircraft.

Chapter 5 - Conclusion

Hydrogen has emerged as a strategic energy carrier for transportation because its high gravimetric energy density and rapid refueling enable long-range applications where battery-only solutions are constrained by range as well as pack mass and weight, especially in HDVs. Despite infrastructure challenges in production, storage, and distribution, sustained interest and deployment trajectories position hydrogen as a credible pathway for low-carbon mobility. Within hydrogen pathways, PEMFC technology aligns with vehicular constraints due to low operating temperature and high voltage, current, and power density, but its limited transient capability, cold-start constraints, and lack of regenerative braking necessitate hybridization with ESSs to meet drivability, efficiency, and reliability requirements. FC-HEVs address FC dynamics and energy recovery via hybrid powertrains.

The necessity for MFCSs follows from limits of single-stack systems at high power and the advantages of modularity, where multiple lower-power stacks provide redundancy, access to multiple high-efficiency operating points, and selective participation that enhances efficiency and durability, alongside packaging flexibility and potential cost benefits from mass production. However, achieving low operating cost and long component life still depends on coordinated management of multiple sources under changing operating demands, which requires an appropriate EMSs which are capable to minimize hydrogen use and degradation across missions.

Sizing choices (the number and rating power of FC stacks, and the battery configuration) determine the power and energy capabilities of the MFCS and thus shape

capital expenditure; under-sizing risks unmet demand, whereas over-sizing adds mass and cost without proportional benefit. Integrating sizing with EMS is equally important because EMS governs how stacks and the battery are dispatched in practice; Integrating sizing with EMS means evaluating candidate architectures under a realistic EMS, so the chosen number and ratings of stacks, their heterogeneity, and the battery settings are selected based on actual mission profiles and constraints affecting hydrogen use and degradation behavior, rather than on sizing assumptions alone.

The literature and prior works exhibit three related gaps in MFCSs: (i) a lack of a scalable, health-aware offline EMS benchmark for MFCSs, as DP becomes impractical and often omits SOH or uses coarse grids that distort optimal dispatch and costs, (ii) sizing and EMS are often handled separately, with fixed FC capacity or stack allocation decided independently of the sizing process and limited battery treatment, which obscures how modularity and heterogeneity influence investment, hydrogen use, and durability; an integrated, degradation-aware sizing–operation approach for MFCSs is missing, and (iii) in aircraft, studies rarely co-optimize cost and propulsion weight for MFCSs or account for uncertain missions with EMS-in-the-loop, leaving modularity benefits underexplored in weight-sensitive contexts such as aircraft.

This dissertation contributes three core advances in MFCSs across design and control: (i) CEM, a scalable offline benchmark EMS for MFCSs that yields health-aware, near-global optimal power splits with reduced dimensionality burden (Chapter 2), (ii) ISEMS, an integrated sizing–operation co-design framework that jointly determines MFCS architecture and evaluates mission-level operational cost and degradation via an inner EMS, enabling economically durable designs for heavy-duty applications (Chapter 3), and (iii)

MISEMS, a multi-objective aircraft extension for MFCSs that co-optimizes total cost and propulsion weight under power-demand uncertainty with EMS-in-the-loop (Chapter 4).

Chapter 2 developed a method named CEM as an offline EMS benchmark for HDVs with MFCSs and a battery, achieving scalability, health awareness, and time efficiency through constraint-guided filters on battery power and SOC bounds. By embedding a cost function that couples hydrogen use with degradation, CEM identified selective stack activation patterns that preserve stack health while meeting power demand, and it remained tractable as control grid density and stack count increased. Case studies demonstrated consistent gains: on NASA X-57, CEM reduced operational cost by 2% and computation time by 10.5% versus level-set DP at 20 grids and outperformed SQP by 14.6% in cost; on a dual-stack tram at 40 grids, CEM lowered cost by 1.7% and simulation time by 90.4% relative to DP and reduced cost by 16.6% versus SQP; on a truck including 4 FC stacks with the power of 75 kW each, CEM coordinated stacks to equalize degradation costs and cut operation cost by 17.1% compared with SQP, while level-set DP was not able to perform EMS for a system containing 4 FC stacks. Chapter 2 thus establishes CEM as a reliable offline reference EMS for MFCS development and as a foundation for future EMS validation.

Chapter 3 presented a degradation-aware ISEMS for MFCSs in HDVs, extending simultaneous sizing and EMS beyond single-stack applications by using a GA–MPC framework that jointly optimized FC stack sizes and battery configuration while evaluating alternative numbers of stacks. Unlike studies that predefined total FC power and then inferred individual stack sizes, the method directly specified each stack's rating and embedded degradation-aware control within a single optimization, enabling architecture

and operation to be assessed together. In the long-haul truck case, the approach reduced total cost by as much as 68% relative to reported configurations, and it identified an optimal design for every modularity level from one to six stacks; the five-stack solution was the most economical at 79.65 $, comprising 18.03 $ operational and 61.62 $ normalized investment, and it achieved the longest life at roughly 2209 hours versus 1514 hours for a single-stack system. In a second case with experimental stacks, the single-stack layout was infeasible under mission limits; among feasible two- to five-stack options, two 2 kW stacks delivered the minimum total cost (3.55 $) and the longest life (~2984 hours), while five stacks shortened life (~1687 hours) owing to higher FC degradation. Sensitivity analysis showed that widening the SOC window from [0.50–0.70] to [0.20–1.00] lowered total cost by up to 67.4% through greater battery use, reduced reliance on FC stacks, and fewer switching events that accelerate degradation of FC stacks. Overall, the method provided a scalable and durable pathway for cost-effective MFCS design and control in HDVs.

Chapter 4 extended the integrated sizing–operation paradigm to aircraft-oriented MFCSs by proposing MISEMS, a multi-objective framework that simultaneously minimized total system cost and propulsion system weight under power demand uncertainty with an embedded EMS. Using an integer-based NSGA-II coupled with a degradation-aware MPC, the method co-optimized FC modularity, FC stacks rated power, and battery sizing. In the NASA X-57 case study, MISEMS reduced the total cost from 157.12 $ to 138.64 $ (11.8%) and lowered the propulsion system weight from 855.63 kg to 705.11 kg (17.6%) relative to a benchmark single-stack configuration, demonstrating the quantitative benefit of MISEMS. Pareto fronts obtained for one- to four-stack architectures showed that increasing modularity shifts solutions toward lower cost–weight regions by

improving load sharing and reducing hydrogen consumption and component stress, while performance gains became marginal beyond intermediate modularity due to the added mass of converters and balance-of-plant components. Battery sizing emerged as a critical driver of the trade-off, where reductions in battery capacity decreased system weight but increased FC dynamic loading and degradation-related costs, particularly for minimum-weight solutions. In the experimental case study, feasible designs spanned total weights from 38.80 kg to 87.03 kg and costs from 5.81 $ to 28.15 $, with the dual-stack configuration achieving the lowest cost and higher stack counts offering no clear advantage, further confirming the existence of an optimal intermediate modularity level. Overall, Chapter 4 demonstrated that robust, cost-efficient, and weight-efficient MFCS architectures for aircraft can only be identified through multi-objective co-design of sizing and EMS.

5.1 Recommendation for Future Works

While this thesis presented novel methods for operation and design of MFCSs in HDVs, the following attempts should be made to further verify and improve the proposed techniques: realize a hierarchical EMS that combines CEM-based EMS with MPC-based one, conduct hybridization-factor studies in ISEMS and MISEMS, consider the outage of FCSs and embed N−1 contingency to enhance reliability of the system, and couple sizing decisions with load updates through mass-aware mission profiles.

5.1.1 Hierarchical EMS: CEM + MPC

CEM has been a high-fidelity benchmark EMS for MFCSs because it can coordinate multi-stack power sharing with health-aware logic, whereas classical DP is not suited to

multi-stack configurations. The goal, therefore, is a time-efficient EMS that is validated by CEM and is competitive enough to serve as a practical benchmark EMS in its own right. A hierarchical EMS addresses this by pairing a CEM-inspired with MPC: the first layer uses CEM to split the requested power between the FCSs and the battery, and the second layer uses MPC at fast rates to allocate the amount of power for FCSs (which is calculated by the CEM in the first layer) among FC stacks while enforcing the constraints of the MFCS.

This hierarchical EMS reduces computation by shrinking the decision space at the upper layer and delegating the high-dimensional allocation to a fast lower layer. When considering M FC stacks and N_{grid} grid points, the discretization level in the CEM is given by ${N_{grid}}^{M+1}$. This corresponds to M variables for the power of the FC stacks and one variable for the battery SOC. In contrast, with a hierarchical EMS, the discretization level reduces to ${N_{grid}}^{2}$, since only two variables are considered: the total power of all FCSs and the battery SOC. In the second layer, the computational time of the MPC is low because it operates as a real-time EMS. Therefore, as the number of FC stacks increases, the gap in computational time between the sole CEM and hierarchical CEM+MPC grows significantly.

5.1.2 Hybridization Factor

The hybridization factor (HF) is the ratio of the battery's peak power to the total peak power of the system, defined as the sum of the battery's maximum power ($P_{bat,max}$) and the combined maximum power of all FC stacks ($\sum_{i=1}^{N_{FC}} P_{FC,i,max}$) [150]:

$$HF = \frac{P_{bat,max}}{P_{bat,max} + \sum_{i=1}^{N_{FC}} P_{FC,i,max}} \tag{5-1}$$

Higher HF means the battery supplies a larger fraction of peak and transient power, while the FC contributes a smaller fraction, directly shaping how power is split during demanding events.

Studies that parameterized designs by HF reported consistent trends: increasing HF enabled FC downsizing and operation nearer efficient regions, improving fuel economy and reducing purchase cost, while also enhancing acceleration performance (e.g., reported gains of several percent in fuel economy and double-digit reductions in purchase price in representative case studies) [150-152]. These benefits diminished at very high HF because added battery mass and conversion/cycling losses reduced net gains, and because meeting the constraints on sustained power sometimes required a substantial FC share, which bounded feasible HF ranges in practice.

As a future extension, ISEMS should set HF to several fixed values, re-solve the sizing for each value, and then run EMS in the inner loop so that the investment and operational costs are obtained for different values of HF. Because the investment cost per unit power is lower for the battery than for the FC, a higher HF is expected to reduce the upfront cost of FCSs by allowing a smaller FC rating. It should also lower operational cost by mitigating FC degradation, since battery support smooths FC transients and reduces damaging load excursions.

Similarly, MISEMS should apply an HF sweep, solving the sizing for each HF and evaluating the missions with the inner EMS to report total cost and weight for multi-stack aircraft-style systems. In this aircraft context, higher HF is expected to lower upfront cost by permitting smaller FC ratings and to reduce operational cost by mitigating FC degradation through battery-smoothed transients, analogous to ISEMS. However, because

battery energy density is lower than that of the FC system, shifting more duty to the battery will increase total system weight to deliver the same energy, so cost reductions at higher HF are anticipated to be accompanied by weight growth that must be considered in aircraft applications.

5.1.3 Reliability and Redundancy Planning

FC stacks may fail in service due to faults, aging, or thermal and voltage stress, which can suddenly remove a significant share of available power from a MFCS. In aircraft and other safety-critical missions, it is essential to continue meeting the requested power during such events to maintain required power without exceeding power limits after the outage of damaged FC stack.

One practical way to ensure this capability is to design and operate for N−1 contingency, meaning the system can tolerate the loss of any single stack without violating constraints. In ISEMS and MISEMS, this requirement should be enforced directly in sizing so that reserve capacity, battery support, and load reallocation are planned for stack-out events; doing so will typically increase total cost and, in aircraft settings, add weight, but it provides the assurance that the MFCS can continue operating safely and meeting mission power if any one FC stack cannot function properly.

5.1.4 Coupling Size Changes to Requested Power

Coupling size changes to requested power requires closing the loop between architecture, mass, and mission demand so that sizing decisions propagate to requested power and, in turn, to EMS outcomes. Because component sizes set powertrain mass and thereby vehicle mass, they reshape the mission load profile; neglecting this feedback biases

cost and lifetime estimates, with particularly large errors in weight-sensitive aircraft missions where small mass shifts affect power requirements. A consistent co-design should therefore update the load after each change in FC or battery sizing and re-evaluate EMS under the revised demand.

Practically, this can be implemented with a mass-aware mission model that recomputes the requested power from weight-dependent aerodynamic drag, rolling resistance, and grade whenever FC or battery sizes are modified, followed by reruns of EMS to obtain hydrogen use, degradation, and lifetime. In aircraft applications, propulsion weight should be coupled with aerodynamic performance and certification constraints to reveal how variations in mass affect cost–weight trade-offs and operational feasibility under uncertain mission and environmental conditions. In HDVs, the framework should identify where added battery mass is beneficial due to increased regenerative capture on specific route segments versus where it worsens grade penalties, thereby yielding actionable mass thresholds at which modular FC additions become preferable to further storage increases.

References

[1] H. B. Yamchi, H. Shahsavari, N. T. Kalantari, A. Safari, and M. Farrokhifar, "A cost-efficient application of different battery energy storage technologies in microgrids considering load uncertainty," *Journal of Energy Storage,* vol. 22, pp. 17-26, 2019.

[2] S. T. Tzeiranaki *et al.*, "The impact of energy efficiency and decarbonisation policies on the European road transport sector," *Transportation Research Part A: Policy and Practice,* vol. 170, p. 103623, 2023.

[3] "International Energy Agency, Aviation." https://www.iea.org/energy-system/transport/aviation (accessed July 22, 2025).

[4] B. Kumar, J. Kumar, A. Q. Amjad, L. Kumar, and C. Sassanelli, "Sustainable aviation finance: Integration of environmental impact mitigation and green investment strategies," *Research in Transportation Business & Management,* vol. 61, 2025, doi: 10.1016/j.rtbm.2025.101410.

[5] A. Ziemińska-Stolarska, M. Sobulska, D. Izquierdo, D. Neumann Dela Cruz, M. Pietrzak, and I. Zbiciński, "Life Cycle Assessment of Hybrid-Electric Aircraft Technologies—A Review," *IEEE Access,* vol. 13, pp. 49989-49999, 2025, doi: 10.1109/access.2025.3549924.

[6] D. S. Lee *et al.*, "The contribution of global aviation to anthropogenic climate forcing for 2000 to 2018," *Atmospheric environment,* vol. 244, p. 117834, 2021.

[7] C. C. Chan, "The state of the art of electric, hybrid, and fuel cell vehicles," *Proceedings of the IEEE,* vol. 95, no. 4, pp. 704-718, 2007.

[8] T. Rudolf, T. Schürmann, S. Schwab, and S. Hohmann, "Toward holistic energy management strategies for fuel cell hybrid electric vehicles in heavy-duty applications," *Proceedings of the IEEE,* vol. 109, no. 6, pp. 1094-1114, 2021.

[9] "Hydrogen Economy Outlook." BloombergNEF. https://data.bloomberglp.com/professional/sites/24/BNEF-Hydrogen-Economy-Outlook-Key-Messages-30-Mar-2020.pdf (accessed 2024-07-16.

[10] A. Alaswad, A. Baroutaji, H. Achour, J. Carton, A. Al Makky, and A.-G. Olabi, "Developments in fuel cell technologies in the transport sector," *International Journal of Hydrogen Energy,* vol. 41, no. 37, pp. 16499-16508, 2016.

[11] E. Çabukoglu, G. Georges, L. Küng, G. Pareschi, and K. Boulouchos, "Fuel cell electric vehicles: An option to decarbonize heavy-duty transport? Results from a Swiss case-study," *Transportation Research Part D: Transport and Environment,* vol. 70, pp. 35-48, 2019.

[12] T. Yalcinoz and M. Alam, "Improved dynamic performance of hybrid PEM fuel cells and ultracapacitors for portable applications," *International Journal of Hydrogen Energy,* vol. 33, no. 7, pp. 1932-1940, 2008.

[13] F. Barbir, *PEM fuel cells: theory and practice*. Academic press, 2012.

[14] N. Sulaiman, M. Hannan, A. Mohamed, E. Majlan, and W. W. Daud, "A review on energy management system for fuel cell hybrid electric vehicle: Issues and challenges," *Renewable and Sustainable Energy Reviews,* vol. 52, pp. 802-814, 2015.

[15] X. Hu, N. Murgovski, L. M. Johannesson, and B. Egardt, "Optimal dimensioning and power management of a fuel cell/battery hybrid bus via convex programming," *IEEE/ASME transactions on mechatronics,* vol. 20, no. 1, pp. 457-468, 2014.

[16] K. Simmons, Y. Guezennec, and S. Onori, "Modeling and energy management control design for a fuel cell hybrid passenger bus," *Journal of Power Sources,* vol. 246, pp. 736-746, 2014.

[17] M. Chen and G. A. Rincon-Mora, "Accurate electrical battery model capable of predicting runtime and IV performance," *IEEE transactions on energy conversion,* vol. 21, no. 2, pp. 504-511, 2006.

[18] D. A. Cullen *et al.*, "New roads and challenges for fuel cells in heavy-duty transportation," *Nature Energy,* vol. 6, no. 5, pp. 462-474, 2021, doi: 10.1038/s41560-021-00775-z.

[19] S. E. Williams, S. C. Davis, and R. G. Boundy, "Transportation energy data book: Edition 36," Oak Ridge National Laboratory (ORNL), Oak Ridge, TN (United States), 2017.

[20] "Fast Facts on Transportation Greenhouse Gas Emissions." US Environmental Protection Agency. https://www.epa.gov/greenvehicles/fast-facts-transportation-greenhouse-gas-emissions (accessed July 30, 2024).

[21] "Hydrogen Deployments." International Partnership for Hydrogen and Fuel Cells in the Economy. https://www.iphe.net/ (accessed July 30, 2024).

[22] D. Papadias, R. Ahluwalia, E. Connelly, and P. Devlin, "Total cost of ownership (tco) analysis for hydrogen fuel cells in maritime applications–preliminary results," *Argonne National Laboratory, Fuel Cell Technologies Office US Department of Energy,* 2019.

[23] P. Hoenicke *et al.*, "Power management control and delivery module for a hybrid electric aircraft using fuel cell and battery," *Energy Conversion and Management,* vol. 244, 2021, doi: 10.1016/j.enconman.2021.114445.

[24] S. Li, C. Gu, P. Zhao, and S. Cheng, "A novel hybrid propulsion system configuration and power distribution strategy for light electric aircraft," *Energy Conversion and Management,* vol. 238, 2021, doi: 10.1016/j.enconman.2021.114171.

[25] Z. Ji, M. M. Rokni, J. Qin, S. Zhang, and P. Dong, "Energy and configuration management strategy for battery/fuel cell/jet engine hybrid propulsion and power

systems on aircraft," *Energy Conversion and Management,* vol. 225, 2020, doi: 10.1016/j.enconman.2020.113393.

[26] L. Zhang, J. Liu, W. Qi, Q. Chen, R. Long, and S. Quan, "A parallel modular computing approach to real-time simulation of multiple fuel cells hybrid power system," *International Journal of Energy Research,* vol. 43, no. 10, pp. 5266-5283, 2019.

[27] A. K. Soltani, M. Kandidayeni, L. Boulon, and D. L. St-Pierre, "Modular energy systems in vehicular applications," *Energy Procedia,* vol. 162, pp. 14-23, 2019.

[28] C. Zhang, T. Zeng, Q. Wu, C. Deng, S. H. Chan, and Z. Liu, "Improved efficiency maximization strategy for vehicular dual-stack fuel cell system considering load state of sub-stacks through predictive soft-loading," *Renewable Energy,* vol. 179, pp. 929-944, 2021/12/01/ 2021, doi: https://doi.org/10.1016/j.renene.2021.07.090.

[29] X. Zhao *et al.*, "Energy management strategies for fuel cell hybrid electric vehicles: Classification, comparison, and outlook," *Energy Conversion and Management,* vol. 270, 2022, doi: 10.1016/j.enconman.2022.116179.

[30] T. Liu, X. Tang, H. Wang, H. Yu, and X. Hu, "Adaptive hierarchical energy management design for a plug-in hybrid electric vehicle," *IEEE Transactions on Vehicular Technology,* vol. 68, no. 12, pp. 11513-11522, 2019.

[31] D.-D. Tran, M. Vafaeipour, M. El Baghdadi, R. Barrero, J. Van Mierlo, and O. Hegazy, "Thorough state-of-the-art analysis of electric and hybrid vehicle powertrains: Topologies and integrated energy management strategies," *Renewable and Sustainable Energy Reviews,* vol. 119, p. 109596, 2020/03/01/ 2020, doi: https://doi.org/10.1016/j.rser.2019.109596.

[32] D. Abdeldjalil, B. Negrou, T. Youssef, and M. M. Samy, "Incorporating the best sizing and a new energy management approach into the fuel cell hybrid electric vehicle design," *Energy & Environment,* 2023, doi: 10.1177/0958305x231177743.

[33] D. Feroldi and M. Carignano, "Sizing for fuel cell/supercapacitor hybrid vehicles based on stochastic driving cycles," *Applied Energy,* vol. 183, pp. 645-658, 2016, doi: 10.1016/j.apenergy.2016.09.008.

[34] M. Cha, H. Enshaei, H. Nguyen, and S. G. Jayasinghe, "Optimal sizing and evaluation of efficient fuel cell utilization for fuel cell battery hybrid electric ferry," *Energy Conversion and Management,* vol. 315, 2024, doi: 10.1016/j.enconman.2024.118723.

[35] A. Macias, M. Kandidayeni, L. Boulon, and H. Chaoui, "A novel online energy management strategy for multi fuel cell systems," in *2018 IEEE International Conference on Industrial Technology (ICIT)*, 2018: IEEE, pp. 2043-2048.

[36] Y. Yan, Q. Li, W. Chen, W. Huang, J. Liu, and J. Liu, "Online control and power coordination method for multistack fuel cells system based on optimal power allocation," *IEEE Transactions on Industrial Electronics,* vol. 68, no. 9, pp. 8158-8168, 2020.

[37] T. Wang, Q. Li, L. Yin, and W. Chen, "Hydrogen consumption minimization method based on the online identification for multi-stack PEMFCs system," *international journal of hydrogen energy,* vol. 44, no. 11, pp. 5074-5081, 2019.

[38] F. Peng, X. Xie, K. Wu, Y. Zhao, and L. Ren, "Online hierarchical energy management strategy for fuel cell based heavy-duty hybrid power systems aiming at collaborative performance enhancement," *Energy Conversion and Management,* vol. 276, p. 116501, 2023.

[39] T. Wang, Q. Li, L. Yin, W. Chen, E. Breaz, and F. Gao, "Hierarchical Power Allocation Method Based on Online Extremum Seeking Algorithm for Dual-PEMFC/Battery Hybrid Locomotive," *IEEE Transactions on Vehicular Technology,* vol. 70, no. 6, pp. 5679-5692, 2021, doi: 10.1109/tvt.2021.3078752.

[40] M. Moghadari, M. Kandidayeni, L. Boulon, and H. Chaoui, "Hydrogen minimization of a hybrid multi-stack fuel cell vehicle using an optimization-based strategy," in *2021 IEEE Vehicle Power and Propulsion Conference (VPPC)*, 2021: IEEE, pp. 1-5.

[41] X. Chai, R. Ma, J. Song, H. Sun, C. Wang, and Z. Feng, "An Energy Management Strategy for All Electric Aircraft Based on Multi-stack Fuel Cells," in *2023 IEEE Transportation Electrification Conference & Expo (ITEC)*, 2023: IEEE, pp. 1-6.

[42] Q. Li *et al.*, "Online extremum seeking-based optimized energy management strategy for hybrid electric tram considering fuel cell degradation," *Applied Energy,* vol. 285, p. 116505, 2021.

[43] A. K. Soltani, L. Boulon, and X. Hu, "Fully Decentralized Energy Management Strategy Based on Model Predictive Control in a Modular Fuel Cell Vehicle," in *2021 IEEE Transportation Electrification Conference & Expo (ITEC)*, 2021: IEEE, pp. 767-770.

[44] H. Zhou, Z. Yu, X. Wu, Z. Fan, X. Yin, and L. Zhou, "Dynamic programming improved online fuzzy power distribution in a demonstration fuel cell hybrid bus," *Energy,* vol. 284, p. 128549, 2023.

[45] S. Tao *et al.*, "Energy management strategy based on dynamic programming with durability extension for fuel cell hybrid tramway," *Railway Engineering Science,* vol. 29, no. 3, pp. 299-313, 2021, doi: 10.1007/s40534-021-00247-w.

[46] X. Meng, Q. Li, G. Zhang, and W. Chen, "Efficient multidimensional dynamic programming-based energy management strategy for global composite operating cost minimization for fuel cell trams," *IEEE Transactions on Transportation Electrification,* vol. 8, no. 2, pp. 1807-1818, 2021.

[47] R. Ghaderi, M. Kandidayeni, L. Boulon, and J. P. Trovão, "Q-learning based energy management strategy for a hybrid multi-stack fuel cell system considering degradation," *Energy Conversion and Management,* vol. 293, p. 117524, 2023.

[48] M. Moghadari, M. Kandidayeni, L. Boulon, and H. Chaoui, "Operating Cost Comparison of a Single-Stack and a Multi-Stack Hybrid Fuel Cell Vehicle Through an Online Hierarchical Strategy," *IEEE Transactions on Vehicular Technology,* pp. 1-13, 2022, doi: 10.1109/tvt.2022.3205879.

[49] W. Shi, Y. Huangfu, L. Xu, and S. Pang, "Online energy management strategy considering fuel cell fault for multi-stack fuel cell hybrid vehicle based on multi-agent reinforcement learning," *Applied Energy,* vol. 328, p. 120234, 2022.

[50] A. Khalatbarisoltani, M. Kandidayeni, L. Boulon, and X. Hu, "A decentralized multi-agent energy management strategy based on a look-ahead reinforcement learning approach," *SAE International Journal of Electrified Vehicles,* vol. 11, no. 2, pp. 151-164, 2022.

[51] T. Paul, T. Mesbahi, S. Durand, D. Flieller, and W. Uhring, "Study and influence of standardized driving cycles on the sizing of li-ion battery/supercapacitor hybrid energy storage," in *2019 IEEE Vehicle Power and Propulsion Conference (VPPC)*, 2019: IEEE, pp. 1-6.

[52] A. N. Akpolat, Y. Yang, F. Blaabjerg, E. Dursun, and A. E. Kuzucuoğlu, "Li-ion-based battery pack designing and sizing for electric vehicles under different road conditions," in *2020 International Conference on Smart Energy Systems and Technologies (SEST)*, 2020: IEEE, pp. 1-6.

[53] K. Venkata KoteswaraRao, G. Naga Srinivasulu, J. Ramesh Rahul, and V. Velisala, "Optimal component sizing and performance of Fuel Cell – Battery powered vehicle over world harmonized and new european driving cycles," *Energy Conversion and Management,* vol. 300, 2024, doi: 10.1016/j.enconman.2023.117992.

[54] Y. Wang, S. J. Moura, S. G. Advani, and A. K. Prasad, "Optimization of powerplant component size on board a fuel cell/battery hybrid bus for fuel economy and system durability," *International Journal of Hydrogen Energy,* vol. 44, no. 33, pp. 18283-18292, 2019, doi: 10.1016/j.ijhydene.2019.05.160.

[55] R. Knibbe *et al.*, "Optimal battery and hydrogen fuel cell sizing in heavy-haul locomotives," *Journal of Energy Storage,* vol. 71, 2023, doi: 10.1016/j.est.2023.108090.

[56] P. G. Anselma and G. Belingardi, "Fuel cell electrified propulsion systems for long-haul heavy-duty trucks: present and future cost-oriented sizing," *Applied Energy,* vol. 321, p. 119354, 2022.

[57] T. Graf, R. Fonk, C. Bauer, J. Kallo, and C. Willich, "Optimal Sizing of Fuel Cell and Battery in a Direct-Hybrid for Electric Aircraft," *Aerospace,* vol. 11, no. 3, 2024, doi: 10.3390/aerospace11030176.

[58] J. Park, D. Lee, D. Lim, and K. Yee, "A refined sizing method of fuel cell-battery hybrid system for eVTOL aircraft," *Applied Energy,* vol. 328, 2022, doi: 10.1016/j.apenergy.2022.120160.

[59] M. Chiara Massaro, S. Pramotton, P. Marocco, A. H. A. Monteverde, and M. Santarelli, "Optimal design of a hydrogen-powered fuel cell system for aircraft applications," *Energy Conversion and Management,* vol. 306, 2024, doi: 10.1016/j.enconman.2024.118266.

[60] M. Sparano *et al.*, "The future technological potential of hydrogen fuel cell systems for aviation and preliminary co-design of a hybrid regional aircraft powertrain

through a mathematical tool," *Energy Conversion and Management,* vol. 281, 2023, doi: 10.1016/j.enconman.2023.116822.

[61] Z. Win Thu, M. Tyan, Y.-H. Choi, M. Irfan Alam, and J.-W. Lee, "Possibility-Based Sizing Method for Hybrid Electric Aircraft," *IEEE Access,* vol. 13, pp. 20945-20959, 2025, doi: 10.1109/access.2025.3531696.

[62] R. Novella, J. D. l. Morena, M. Lopez-Juarez, and I. Nidaguila, "Effect of differential control and sizing on multi-FCS architectures for heavy-duty fuel cell vehicles," *Energy Conversion and Management,* vol. 293, 2023, doi: 10.1016/j.enconman.2023.117498.

[63] S. Zhou, G. Zhang, L. Fan, J. Gao, and F. Pei, "Scenario-oriented stacks allocation optimization for multi-stack fuel cell systems," *Applied Energy,* vol. 308, 2022, doi: 10.1016/j.apenergy.2021.118328.

[64] G. Zhang, S. Zhou, J. Gao, L. Fan, and Y. Lu, "Stacks multi-objective allocation optimization for multi-stack fuel cell systems," *Applied Energy,* vol. 331, 2023, doi: 10.1016/j.apenergy.2022.120370.

[65] H. B. Yamchi, M. Kandidayeni, S. Kelouwani, and L. Boulon, "The impact of stack allocation on the performance of a hybrid multi-stack fuel cell system," in *2024 IEEE Vehicle Power and Propulsion Conference (VPPC)*, 2024: IEEE, pp. 1-5.

[66] L. Zhang, X. Ye, X. Xia, and F. Barzegar, "A real-time energy management and speed controller for an electric vehicle powered by a hybrid energy storage system," *IEEE Transactions on Industrial Informatics,* vol. 16, no. 10, pp. 6272-6280, 2020.

[67] H. Chen, Z. Zhang, C. Guan, and H. Gao, "Optimization of sizing and frequency control in battery/supercapacitor hybrid energy storage system for fuel cell ship," *Energy,* vol. 197, p. 117285, 2020.

[68] M. H. Madadi and I. Chitsaz, "Improving fuel efficiency and durability in fuel cell vehicles through component sizing and power distribution management," *International Journal of Hydrogen Energy,* vol. 71, pp. 661-673, 2024, doi: 10.1016/j.ijhydene.2024.05.276.

[69] H. Sadek, R. Chedid, and D. Fares, "Power sources sizing for a fuel cell hybrid vehicle," *Energy Storage,* vol. 2, no. 2, 2020, doi: 10.1002/est2.124.

[70] T. Fletcher and K. Ebrahimi, "The Effect of Fuel Cell and Battery Size on Efficiency and Cell Lifetime for an L7e Fuel Cell Hybrid Vehicle," *Energies,* vol. 13, no. 22, 2020, doi: 10.3390/en13225889.

[71] H.-S. Yi, J.-B. Jeong, S.-W. Cha, and C.-H. Zheng, "Optimal component sizing of fuel cell-battery excavator based on workload," *International Journal of Precision Engineering and Manufacturing-Green Technology,* vol. 5, no. 1, pp. 103-110, 2018, doi: 10.1007/s40684-018-0011-z.

[72] S. F. da Silva *et al.*, "Aging-aware optimal power management control and component sizing of a fuel cell hybrid electric vehicle powertrain," *Energy Conversion and Management,* vol. 292, 2023, doi: 10.1016/j.enconman.2023.117330.

[73] Q. Xun, N. Murgovski, and Y. Liu, "Joint Component Sizing and Energy Management for Fuel Cell Hybrid Electric Trucks," *IEEE Transactions on Vehicular Technology,* vol. 71, no. 5, pp. 4863-4878, 2022, doi: 10.1109/tvt.2022.3154146.

[74] H. B. Yamchi, A. Safari, and J. M. Guerrero, "A multi-objective mixed integer linear programming model for integrated electricity-gas network expansion planning considering the impact of photovoltaic generation," *Energy,* vol. 222, p. 119933, 2021.

[75] A. Makhsoos, M. Kandidayeni, L. Boulon, and B. G. Pollet, "A comparative analysis of single and modular proton exchange membrane water electrolyzers for green hydrogen production-a case study in Trois-Rivières," *Energy,* vol. 282, p. 128911, 2023.

[76] M. Kandidayeni, M. Soleymani, A. Macias, J. P. Trovão, and L. Boulon, "Online power and efficiency estimation of a fuel cell system for adaptive energy management designs," *Energy Conversion and Management,* vol. 255, p. 115324, 2022.

[77] X. Zhao *et al.*, "Energy management strategies for fuel cell hybrid electric vehicles: Classification, comparison, and outlook," *Energy Conversion and Management,* vol. 270, p. 116179, 2022/10/15/ 2022, doi: https://doi.org/10.1016/j.enconman.2022.116179.

[78] M. Kandidayeni, J. Trovão, M. Soleymani, and L. Boulon, "Towards health-aware energy management strategies in fuel cell hybrid electric vehicles: A review," *International Journal of Hydrogen Energy,* 2022.

[79] W. B. Powell, "Approximate Dynamic Programming - Solving the Curses of Dimensionality," in *Wiley Series in Probability and Statistics*, 2007.

[80] A. Macias Fernandez, M. Kandidayeni, L. Boulon, and H. Chaoui, "An Adaptive State Machine Based Energy Management Strategy for a Multi-Stack Fuel Cell Hybrid Electric Vehicle," *IEEE Transactions on Vehicular Technology,* vol. 69, no. 1, pp. 220-234, 2020, doi: 10.1109/tvt.2019.2950558.

[81] S. Zhou *et al.*, "A review on proton exchange membrane multi-stack fuel cell systems: architecture, performance, and power management," *Applied Energy,* vol. 310, 2022, doi: 10.1016/j.apenergy.2022.118555.

[82] A. L. Dicks and D. A. Rand, *Fuel cell systems explained*. John Wiley & Sons, 2018.

[83] M. Kandidayeni, J. P. F. Trovão, L. Boulon, and S. Kelouwani, "Health-wise energy management strategies in fuel cell hybrid electric vehicles: Tools to optimize performance and reduce operational costs," *IEEE Electrification Magazine,* vol. 12, no. 2, pp. 80-88, 2024.

[84] P. Pei, Q. Chang, and T. Tang, "A quick evaluating method for automotive fuel cell lifetime," *International Journal of Hydrogen Energy,* vol. 33, no. 14, pp. 3829-3836, 2008.

[85] S. Dirkes, J. Leidig, P. Fisch, and S. Pischinger, "Prescriptive Lifetime Management for PEM fuel cell systems in transportation applications, Part I: State of the art and conceptual design," *Energy Conversion and Management,* vol. 277, p. 116598, 2023.

[86] X. Hu, C. Zou, X. Tang, T. Liu, and L. Hu, "Cost-optimal energy management of hybrid electric vehicles using fuel cell/battery health-aware predictive control," *ieee transactions on power electronics,* vol. 35, no. 1, pp. 382-392, 2019.

[87] D. E. Kirk, *Optimal control theory: an introduction*. Courier Corporation, 2004.

[88] O. Sundstrom and L. Guzzella, "A generic dynamic programming Matlab function," in *2009 IEEE control applications,(CCA) & intelligent control,(ISIC)*, 2009: IEEE, pp. 1625-1630.

[89] W. Zhou, L. Yang, Y. Cai, and T. Ying, "Dynamic programming for new energy vehicles based on their work modes Part II: Fuel cell electric vehicles," *Journal of Power Sources,* vol. 407, pp. 92-104, 2018.

[90] S. Li *et al.*, "Hybrid Power System Topology and Energy Management Scheme Design for Hydrogen-Powered Aircraft," *IEEE Transactions on Smart Grid,* no. 99, pp. 1-1, 2023.

[91] "PEM fuel cell stack M240." https://advancedtech.airliquide.com/sites/alat/files/2024-02/axane_datasheet_m-stack240_en_09_23_sd.pdf (accessed December 18, 2024).

[92] P. Elbert, S. Ebbesen, and L. Guzzella, "Implementation of dynamic programming for $ n $-dimensional optimal control problems with final state constraints," *IEEE Transactions on Control Systems Technology,* vol. 21, no. 3, pp. 924-931, 2012.

[93] J. P. Torreglosa, F. Jurado, P. García, and L. M. Fernández, "Application of cascade and fuzzy logic based control in a model of a fuel-cell hybrid tramway," *Engineering Applications of Artificial Intelligence,* vol. 24, no. 1, pp. 1-11, 2011.

[94] "P Stack." https://powercellgroup.com/product/p-stack/ (accessed December 13, 2023).

[95] J. P. Torreglosa, F. Jurado, P. García, and L. M. Fernández, "Hybrid fuel cell and battery tramway control based on an equivalent consumption minimization strategy," *Control Engineering Practice,* vol. 19, no. 10, pp. 1182-1194, 2011.

[96] C. Li, "The optimization of hydrogen consumption based on the controlling of charging circuit in Nemo hybrid electric vehicle," Université du Québec à Trois-Rivières, 2015.

[97] Z. Wang, S. Zhang, W. Luo, and S. Xu, "Deep reinforcement learning with deep-Q-network based energy management for fuel cell hybrid electric truck," *Energy,* vol. 306, p. 132531, 2024/10/15/ 2024, doi: https://doi.org/10.1016/j.energy.2024.132531.

[98] A. Moslehi, M. Kandidayeni, M. Hébert, and S. Kelouwani, "Investigating the impact of a fuel cell system air supply control on the performance of an energy

management strategy," *Energy Conversion and Management,* vol. 325, p. 119374, 2025.

[99] C. Jia, H. He, J. Zhou, J. Li, Z. Wei, and K. Li, "Learning-based model predictive energy management for fuel cell hybrid electric bus with health-aware control," *Applied Energy,* vol. 355, 2024, doi: 10.1016/j.apenergy.2023.122228.

[100] M. Piras, V. De Bellis, E. Malfi, R. Novella, and M. Lopez-Juarez, "Hydrogen consumption and durability assessment of fuel cell vehicles in realistic driving," *Applied Energy,* vol. 358, 2024, doi: 10.1016/j.apenergy.2023.122559.

[101] Z. Nie, Y. Feng, and Y. Lian, "Deep reinforcement learning-based hierarchical control strategy for energy management of intelligent fuel cell hybrid electric vehicles," *Energy,* p. 136281, 2025.

[102] X. Guo and G. An, "A Hierarchical Optimization Energy Management Strategy Based on AECMS-MPC for Heavy-Duty Fuel Cell Hybrid Vehicles," *Energy,* p. 137591, 2025.

[103] D. Song, Q. Wu, Y. Huang, X. Zeng, and D. Yang, "Energy-thermal collaborative management considering powertrain thermal characteristics for fuel cell vehicles in low-temperature environment," *Energy,* vol. 320, p. 135102, 2025.

[104] H. B. Yamchi, M. Kandidayeni, S. Kelouwani, and L. Boulon, "Constrained exploration method for optimal energy management in hybrid multi-stack fuel cell vehicles," *Energy Conversion and Management,* vol. 316, p. 118841, 2024.

[105] M. Kandidayeni, H. B. Yamchi, and J. P. F. Trovao, "Advancing Hydrogen and Fuel Cell Technologies for Sustainable Aviation: Challenges and Future Directions," in *Hydrogen and Low-Carbon Fuels in Circular Bio-economy: Assessment Methodologies, Production Technologies and Sector-Specific Applications*, V. Paolini and F. Petracchini Eds. Cham: Springer Nature Switzerland, 2025, pp. 255-304.

[106] M. Moghadari, M. Kandidayeni, L. Boulon, and H. Chaoui, "Predictive Health-Conscious Energy Management Strategy of a Hybrid Multi-Stack Fuel Cell Vehicle," *IEEE Transactions on Vehicular Technology,* 2024.

[107] C. Jia, W. Liu, H. He, and K. Chau, "Deep reinforcement learning-based energy management strategy for fuel cell buses integrating future road information and cabin comfort control," *Energy Conversion and Management,* vol. 321, p. 119032, 2024.

[108] C. Jia, W. Liu, H. He, and K. Chau, "Health-conscious energy management for fuel cell vehicles: An integrated thermal management strategy for cabin and energy source systems," *Energy,* vol. 333, p. 137330, 2025.

[109] T. Tang *et al.*, "Energy management of fuel cell hybrid electric bus in mountainous regions: A deep reinforcement learning approach considering terrain characteristics," *Energy,* vol. 311, p. 133313, 2024/12/01/ 2024, doi: https://doi.org/10.1016/j.energy.2024.133313.

[110] Y. Zhao, S. Huang, X. Wang, J. Shi, and S. Yao, "Energy management with adaptive moving average filter and deep deterministic policy gradient reinforcement learning for fuel cell hybrid electric vehicles," *Energy,* vol. 312, p. 133395, 2024/12/15/ 2024, doi: https://doi.org/10.1016/j.energy.2024.133395.

[111] G. Squadrito, G. Maggio, E. Passalacqua, F. Lufrano, and A. Patti, "An empirical equation for polymer electrolyte fuel cell (PEFC) behaviour," *Journal of Applied Electrochemistry,* vol. 29, no. 12, pp. 1449-1455, 1999.

[112] X.-Z. Yuan, H. Li, S. Zhang, J. Martin, and H. Wang, "A review of polymer electrolyte membrane fuel cell durability test protocols," *Journal of Power Sources,* vol. 196, no. 22, pp. 9107-9116, 2011.

[113] Y. Zhou, A. Ravey, and M.-C. Péra, "Real-time cost-minimization power-allocating strategy via model predictive control for fuel cell hybrid electric vehicles," *Energy Conversion and Management,* vol. 229, p. 113721, 2021.

[114] V. Johnson, "Battery performance models in ADVISOR," *Journal of power sources,* vol. 110, no. 2, pp. 321-329, 2002.

[115] I. Bloom *et al.*, "An accelerated calendar and cycle life study of Li-ion cells," *Journal of power sources,* vol. 101, no. 2, pp. 238-247, 2001.

[116] J. Wang *et al.*, "Cycle-life model for graphite-LiFePO4 cells," *Journal of power sources,* vol. 196, no. 8, pp. 3942-3948, 2011.

[117] S. Ebbesen, P. Elbert, and L. Guzzella, "Battery state-of-health perceptive energy management for hybrid electric vehicles," *IEEE Transactions on Vehicular technology,* vol. 61, no. 7, pp. 2893-2900, 2012.

[118] A. Konak, D. W. Coit, and A. E. Smith, "Multi-objective optimization using genetic algorithms: A tutorial," *Reliability engineering & system safety,* vol. 91, no. 9, pp. 992-1007, 2006.

[119] A. Macias Fernandez, M. Kandidayeni, L. Boulon, and J. P. Trovão, "Effects of Price Range Variation on Optimal Sizing and Energy Management Performance of a Hybrid Fuel Cell Vehicle," *IEEE Transactions on Energy Conversion,* vol. 38, no. 3, pp. 1626-1638, 2023, doi: 10.1109/tec.2023.3240723.

[120] "PowerCellution, V Stack." https://powercellgroup.com/wp-content/uploads/2022/05/v-stack-v-221.pdf (accessed February 15, 2025).

[121] "PowerCellution, P Stack." https://powercellgroup.com/wp-content/uploads/2023/10/p-stack-v-222.pdf (accessed February 15, 2025).

[122] "High-power type cells." https://www.global.toshiba/ww/products-solutions/battery/scib/product-next/product/cell/high-power.html (accessed February 22, 2025).

[123] M. Kandidayeni, H. Chaoui, L. Boulon, and J. P. F. Trovão, "Adaptive parameter identification of a fuel cell system for health-conscious energy management applications," *IEEE Transactions on Intelligent Transportation Systems,* vol. 23, no. 7, pp. 7963-7973, 2021.

[124] M. Kandidayeni, H. Chaoui, L. Boulon, S. Kelouwani, and J. P. Trovão, "Online system identification of a fuel cell stack with guaranteed stability for energy management applications," *IEEE Transactions on Energy Conversion,* vol. 36, no. 4, pp. 2714-2723, 2021.

[125] A. L. C. Ferrer and A. M. T. Thome, "Carbon emissions in transportation: A synthesis framework," *Sustainability,* vol. 15, no. 11, p. 8475, 2023.

[126] D. Scholz, "Calculation of the emission characteristics of aircraft kerosene and hydrogen propulsion," *Harvard Data-Verse,* 2020.

[127] Y. Yan, B. Wang, C. Wang, C. Xiao, and D. Zhao, "Novel Synergistic Framework Design and Optimization for Hydrogen-Electric Hybrid Power System in Unmanned Aerial Vehicle Applications," *IEEE Transactions on Transportation Electrification,* vol. 11, no. 1, pp. 337-347, 2025, doi: 10.1109/tte.2024.3390175.

[128] G. D. Brewer, *Hydrogen aircraft technology*. Routledge, 2017.

[129] M. Aminudin, S. Kamarudin, B. Lim, E. Majilan, M. Masdar, and N. Shaari, "An overview: Current progress on hydrogen fuel cell vehicles," *International Journal of Hydrogen Energy,* vol. 48, no. 11, pp. 4371-4388, 2023.

[130] Y. Zhang, Y. Zhang, R. Ma, Y. Zhou, D. Zhao, and Y. Li, "An Online Energy Management Strategy Based on SOC Fluctuation Optimization for Fuel Cell UAV," *IEEE Transactions on Transportation Electrification,* vol. 10, no. 2, pp. 3105-3113, 2024, doi: 10.1109/tte.2023.3300150.

[131] Y. Wang, F. Xu, S. Mao, S. Yang, and Y. Shen, "Adaptive Online Power Management for More Electric Aircraft With Hybrid Energy Storage Systems," *IEEE Transactions on Transportation Electrification,* vol. 6, no. 4, pp. 1780-1790, 2020, doi: 10.1109/tte.2020.2988153.

[132] J. Zhang, I. Roumeliotis, and A. Zolotas, "Nonlinear Model Predictive Control-Based Optimal Energy Management for Hybrid Electric Aircraft Considering Aerodynamics-Propulsion Coupling Effects," *IEEE Transactions on Transportation Electrification,* vol. 8, no. 2, pp. 2640-2653, 2022, doi: 10.1109/tte.2021.3137260.

[133] W. Shi *et al.*, "Optimal Energy Management for Multistack Fuel Cell Vehicles Based on Hybrid Quantum Reinforcement Learning," *IEEE Transactions on Transportation Electrification,* vol. 11, no. 3, pp. 8500-8511, 2025, doi: 10.1109/tte.2025.3542021.

[134] R. Ma, J. Song, Y. Zhang, H. Zhang, and M. Yuan, "Lifetime-Optimized Energy Management Strategy for Fuel Cell Unmanned Aircraft Vehicle Hybrid Power System," *IEEE Transactions on Industrial Electronics,* vol. 70, no. 9, pp. 9046-9056, 2023, doi: 10.1109/tie.2022.3206687.

[135] P. Li, S. Zhuo, and Y. Huangfu, "Energy Management Strategy for Fuel Cell Unmanned Aerial Vehicles Considering Comprehensive System Operating Cost," *IEEE Transactions on Transportation Electrification,* pp. 1-1, 2025, doi: 10.1109/tte.2025.3590577.

[136] X. Guo *et al.*, "Noise-Adaptive Multimode Online Energy Management for PEMFC/Battery Hybrid UAVs," *IEEE Transactions on Transportation Electrification,* vol. 11, no. 1, pp. 2609-2618, 2025, doi: 10.1109/tte.2024.3422108.

[137] S. Li *et al.*, "Hybrid Power System Topology and Energy Management Scheme Design for Hydrogen-Powered Aircraft," *IEEE Transactions on Smart Grid,* vol. 15, no. 2, pp. 1201-1212, 2024, doi: 10.1109/tsg.2023.3292088.

[138] R. Quan, Z. Li, P. Liu, Y. Li, Y. Chang, and H. Yan, "Minimum hydrogen consumption-based energy management strategy for hybrid fuel cell unmanned aerial vehicles using direction prediction optimal foraging algorithm," *Fuel Cells,* vol. 23, no. 2, pp. 221-236, 2023, doi: 10.1002/fuce.202200121.

[139] W. Tian, L. liu, X. Zhang, and D. Yang, "Double-layer fuzzy adaptive NMPC coordinated control method of energy management and trajectory tracking for hybrid electric fixed wing UAVs," *International Journal of Hydrogen Energy,* 2022, doi: 10.1016/j.ijhydene.2022.09.083.

[140] R. Ma, J. Song, H. Zhang, X. Chai, and H. Sun, "A novel energy management strategy based on minimum internal loss for a Fuel Cell UAV," presented at the 2022 IEEE Transportation Electrification Conference & Expo (ITEC), 2022.

[141] F. Deng, X. Li, W. Yao, T. Lei, W. Li, and X. Zhang, "Distributed Power Management Strategy for Multistack Fuel Cell Systems in Electric Propulsion Aircraft With Efficiency Reinforcement," *IEEE Transactions on Aerospace and Electronic Systems,* vol. 61, no. 3, pp. 5659-5668, 2025, doi: 10.1109/taes.2024.3519487.

[142] T. Kadyk, R. Schenkendorf, S. Hawner, B. Yildiz, and U. Römer, "Design of fuel cell systems for aviation: representative mission profiles and sensitivity analyses," *Frontiers in Energy Research,* vol. 7, p. 35, 2019.

[143] R. Vazquez, D. Rivas, and A. Franco, "Stochastic analysis of fuel consumption in aircraft cruise subject to along-track wind uncertainty," *Aerospace Science and Technology,* vol. 66, pp. 304-314, 2017.

[144] Z. Wang, S. Bu, J. Wen, and C. Huang, "A comprehensive review on uncertainty modeling methods in modern power systems," *International Journal of Electrical Power & Energy Systems,* vol. 166, p. 110534, 2025/05/01/ 2025, doi: https://doi.org/10.1016/j.ijepes.2025.110534.

[145] M. Densing and Y. Wan, "Low-dimensional scenario generation method of solar and wind availability for representative days in energy modeling," *Applied Energy,* vol. 306, p. 118075, 2022/01/15/ 2022, doi: https://doi.org/10.1016/j.apenergy.2021.118075.

[146] K. Deb, A. Pratap, S. Agarwal, and T. Meyarivan, "A fast and elitist multiobjective genetic algorithm: NSGA-II," *IEEE transactions on evolutionary computation,* vol. 6, no. 2, pp. 182-197, 2002.

[147] D. Menzi, L. Imperiali, E. Bürgisser, M. Ulmer, J. Huber, and J. W. Kolar, "Ultralightweight High-Efficiency Buck-Boost DC-DC Converters for Future eVTOL Aircraft With Hybrid Power Supply," *IEEE Transactions on*

Transportation Electrification, vol. 10, no. 4, pp. 10297-10313, 2024, doi: 10.1109/TTE.2024.3375026.

[148] S. Pardhi, S. Chakraborty, D.-D. Tran, M. El Baghdadi, S. Wilkins, and O. Hegazy, "A Review of Fuel Cell Powertrains for Long-Haul Heavy-Duty Vehicles: Technology, Hydrogen, Energy and Thermal Management Solutions," *Energies,* vol. 15, no. 24, p. 9557, 2022. [Online]. Available: https://www.mdpi.com/1996-1073/15/24/9557.

[149] A. Thirkell, R. Chen, and I. Harrington, "A fuel cell system sizing tool based on current production aircraft," SAE Technical Paper, 0148-7191, 2017.

[150] S. C. A. de Almeida and R. Kruczan, "Effects of drivetrain hybridization on fuel economy, performance and costs of a fuel cell hybrid electric vehicle," *International Journal of Hydrogen Energy,* vol. 46, no. 79, pp. 39404-39414, 2021/11/16/ 2021, doi: https://doi.org/10.1016/j.ijhydene.2021.09.144.

[151] M. Huang *et al.*, "Research on hybrid ratio of fuel cell hybrid vehicle based on ADVISOR," *International Journal of Hydrogen Energy,* vol. 41, no. 36, pp. 16282-16286, 2016/09/28/ 2016, doi: https://doi.org/10.1016/j.ijhydene.2016.05.130.

[152] R. K. Ahluwalia, X. Wang, and A. Rousseau, "Fuel economy of hybrid fuel-cell vehicles," *Journal of Power Sources,* vol. 152, pp. 233-244, 2005/12/01/ 2005, doi: https://doi.org/10.1016/j.jpowsour.2005.01.052.

Publications

- **Journal Article**

1) **H. B. Yamchi,** M. Kandidayeni, S. Kelouwani, and L. Boulon, "Constrained exploration method for optimal energy management in hybrid multi-stack fuel cell vehicles," *Energy Conversion and Management,* vol. 316, p. 118841, 2024.

2) **H. B. Yamchi,** M. Moghadari, M. Kandidayeni, S. Kelouwani, and L. Boulon, "An Integrated Degradation-Aware Framework for Sizing and Energy Management in Hybrid Multi-Stack Fuel Cell Vehicles," *Energy,* p. 140188, 2026.

3) Integrated Sizing and Energy Management of Hybrid Multi-Stack Fuel Cell Systems in Aircraft under Power Demand Uncertainty (ready to submit)

- **Conference Article**

1) **H. B. Yamchi,** M. Kandidayeni, S. Kelouwani, and L. Boulon, "The impact of stack allocation on the performance of a hybrid multi-stack fuel cell system," in 2024 IEEE Vehicle Power and Propulsion Conference (VPPC), 2024: IEEE, pp. 1-5.

- **Book Chapter**

2) M. Kandidayeni, **H. B. Yamchi,** and J. P. F. Trovao, "Advancing Hydrogen and Fuel Cell Technologies for Sustainable Aviation: Challenges and Future Directions," in *Hydrogen and Low-Carbon Fuels in Circular Bio-economy: Assessment Methodologies, Production Technologies and Sector-Specific Applications*: Springer, 2025, pp. 255-304.

Appendix A - Résumé

A.1 Motivation

A.1.1 Rôle de l'hydrogène dans les transports futurs

Notre dépendance aux combustibles fossiles conventionnels a entraîné une dégradation environnementale importante, accéléré la crise climatique et épuisé rapidement les réserves naturelles limitées de la planète. Pour faire face à ces problèmes, les sources d'énergie respectueuses de l'environnement, connues sous le nom d'énergies renouvelables, suscitent une attention croissante [1].

Actuellement, le secteur des transports représente environ 25 % de la consommation mondiale d'énergie et dépend majoritairement des combustibles fossiles, ce qui accentue considérablement les problèmes environnementaux [2]. L'aviation joue un rôle crucial dans ce contexte, car elle constitue une source notable et en constante augmentation d'émissions. Selon l'Agence internationale de l'énergie (AIE), en 2022 ce secteur représentait environ 2% des émissions mondiales de CO_2 liées à l'énergie, avec une trajectoire de croissance dépassant celle des transports ferroviaire, routier et maritime au cours des dernières décennies. À cette date, les émissions de l'aviation avaient retrouvé près de 80 % de leur niveau d'avant la pandémie, et les prévisions indiquent qu'elles dépasseront les niveaux de 2019 vers 2025 et pourraient tripler d'ici 2050 si les tendances actuelles se maintiennent [3, 4].

Au-delà des émissions de CO_2, les opérations aériennes génèrent également d'autres polluants qui exercent des effets indirects significatifs sur le système climatique. La combustion du carburant d'aviation produit du monoxyde de carbone (CO), des oxydes d'azote (NOx), de la vapeur d'eau (H_2O), des composés organiques volatils (COV), des ions sulfate (SO_4^{2-}), des particules fines (PM) ainsi que de la suie [5]. L'influence combinée du CO_2, des NOx, de la vapeur d'eau et de la formation de traînées de condensation contribue de manière significative au forçage radiatif, renforçant ainsi le rôle de l'aviation dans le changement climatique [6].

Au cours des dernières décennies, une gamme croissante de véhicules hybrides électriques (VHE), qui combinent des moteurs électriques et des moteurs à combustion interne, ainsi que des véhicules entièrement électriques à batterie (VEB), a été développée. Ces avancées répondent à la demande croissante de solutions de transport durables et localement sans émissions [7].

Les VEB présentent toutefois certains défis, notamment une autonomie plus faible comparativement aux VHE et la nécessité d'infrastructures de recharge étendues. Les efforts visant à améliorer l'autonomie des VEB se concentrent sur l'augmentation de la densité énergétique gravimétrique et volumétrique. Cependant, pour les véhicules lourds (VL), la technologie actuelle des batteries peine à répondre aux exigences élevées de puissance et d'autonomie sur de longues distances. La recharge rapide afin de réduire le temps de trajet ainsi que la durabilité des composants constituent également des facteurs économiques essentiels pour les VL [8].

L'hydrogène devrait jouer un rôle clé dans les futurs systèmes énergétiques. D'ici 2050, son utilisation est estimée à 187 MMT dans un scénario de politiques faibles, couvrant 7 %

des besoins énergétiques dans un scénario de réchauffement de 1,5 °C. Des politiques plus ambitieuses pourraient porter l'utilisation de l'hydrogène à 696 MMT, couvrant 24 % de la demande finale d'énergie, ce qui nécessiterait plus de 11 billions de dollars d'investissements dans les infrastructures. Une adoption complète dans l'ensemble des secteurs pourrait porter la demande à 1 370 MMT. Ces projections et les informations associées sont illustrées à la Fig. A-1 [9]. Sur la base de cette figure, la part du secteur des transports est importante, représentant 33,1 % dans le scénario maximal (1584 MMT), 43,2 % dans le scénario de politiques fortes (301 MMT) et 65,8 % dans le scénario de politiques faibles (123 MMT).

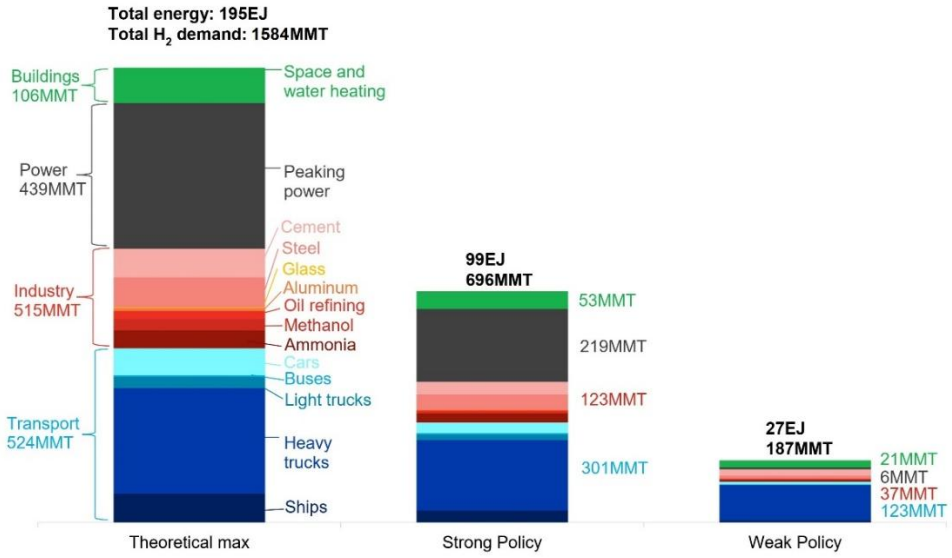

Fig. A-1. Demande projetée d'hydrogène selon différents scénarios à l'horizon 2050 [9].

La mise en œuvre de la technologie des systèmes à pile à combustible (PAC) comme source principale d'énergie pour les VL pourrait être avantageuse en raison de la densité énergétique gravimétrique élevée de l'hydrogène et de la possibilité de ravitaillement rapide. Malgré les défis persistants tels que la production d'hydrogène à grande échelle, sa distribution, les infrastructures de stockage et la manipulation sécuritaire dans les

infrastructures et les systèmes de carburant des véhicules [10], les véhicules à PAC représentent une solution prometteuse pour les applications nécessitant une énergie élevée [11].

A.1.2 Véhicules hybrides électriques à pile à combustible

Il existe plusieurs types de PAC disponibles commercialement, notamment les piles à membrane échangeuse de protons (PACMEP), les piles à oxyde solide, les piles alcalines et les piles à méthanol direct. Parmi celles-ci, la technologie PACMEP est largement utilisée, en particulier dans les applications de transport [12]. La popularité des systèmes PACMEP peut être attribuée à plusieurs avantages, notamment leur capacité à fonctionner à basse température, leur tolérance au CO_2 et l'utilisation de l'air atmosphérique comme oxydant. Ils présentent également une densité élevée de tension, de courant et de puissance, fonctionnent en toute sécurité à basse pression et tolèrent les différences de pression des réactifs. De plus, les PACMEP sont compacts, robustes, mécaniquement simples et fabriqués à partir de matériaux stables, ce qui améliore leur fiabilité [13].

Malgré les progrès significatifs réalisés dans le domaine des PAC, celles-ci présentent une réponse lente aux demandes de puissance, subissent des fluctuations de tension en fonction des variations de charge, rencontrent des difficultés de démarrage à froid dans les climats froids et ne peuvent pas absorber l'énergie de freinage. Par conséquent, un système PAC autonome ne peut pas répondre à toutes les exigences d'un véhicule à pile à combustible. Ainsi, l'intégration d'une source de puissance secondaire, telle qu'une batterie ou un supercondensateur (SC), est essentielle pour gérer les charges dynamiques rapides, réduire la dégradation des PACMEP en absorbant les pics de puissance, améliorer l'économie de carburant, alimenter le véhicule lors des démarrages à froid et permettre la

récupération d'énergie. Les structures d'hybridation courantes pour les véhicules hybrides électriques à pile à combustible (VHE-PAC) comprennent les configurations PAC-batterie, PAC-SC et PAC-batterie-SC. Chacune présente ses propres avantages et inconvénients [14].

La structure PAC-batterie est largement utilisée dans les VHE-PAC pratiques [15, 16]. Dans cette configuration, la PAC-MEP agit comme la source principale de puissance, connectée à la charge via un convertisseur unidirectionnel, tandis que la batterie, en tant que source secondaire, est directement connectée au bus continu (bus DC). Cette configuration offre des coûts de groupe motopropulseur plus faibles et une consommation de carburant réduite par rapport au système PAC-SC [14]. La configuration PAC-batterie-SC offre toutefois une consommation de carburant encore plus faible et peut prolonger la durée de vie de la batterie, mais elle entraîne des coûts, une masse et un volume plus élevés en raison de la nécessité d'un convertisseur supplémentaire. Parmi les différentes batteries rechargeables, les batteries lithium-ion (BLi) sont considérées comme une source secondaire prometteuse pour les VHE-PAC en raison de leur grande capacité, de leurs nombreux cycles de charge-décharge et de leur coût raisonnable [17].

A.1.3 Véhicules lourds

Bien que le développement des PAC pour les véhicules légers (VLég) s'étende sur plus de vingt ans, l'attention portée à leur application dans les VL est un phénomène plus récent. Cet intérêt renouvelé est motivé par la capacité intrinsèque des PAC à évoluer en termes de puissance et d'énergie, ce qui peut être amélioré en augmentant la taille du stack PAC ou du réservoir d'hydrogène, avec seulement une augmentation limitée du poids par rapport aux BLi. De plus, le déploiement commercial des VL nécessite moins d'investissements en

infrastructures, car un nombre plus restreint de stations de ravitaillement est requis en raison des itinéraires spécifiques et prévisibles généralement utilisés par ces véhicules [18].

Par ailleurs, le secteur des VL joue un rôle crucial dans les efforts visant à réduire la consommation d'énergie et les émissions. Actuellement, les camions moyens et lourds représentent 25 % de la consommation annuelle totale de carburant des véhicules et génèrent 23 % des émissions totales de dioxyde de carbone aux États-Unis [19, 20]. En outre, le kilométrage annuel des camions de transport de marchandises devrait augmenter de 54 % d'ici 2050 [18].

Les PAC peuvent être utilisées dans divers secteurs, notamment dans le transport lourd, où elles sont intégrées dans les VHE pour des applications tant pour les passagers que commerciales. Elles sont également évaluées pour les locomotives de fret, régionales et de manœuvre, offrant des améliorations d'efficacité par rapport aux moteurs conventionnels. Dans les applications maritimes, les PAC sont envisagées afin de satisfaire aux objectifs stricts de réduction des émissions, notamment pour diminuer les émissions de soufre et de CO_2 des carburants marins [21, 22]. La Fig. A-2 illustre la feuille de route pour la transition des applications des PAC des VLég vers les applications de moyenne et grande puissance, mettant en évidence le changement de paradigme en matière de kilométrage quotidien et de besoins en puissance.

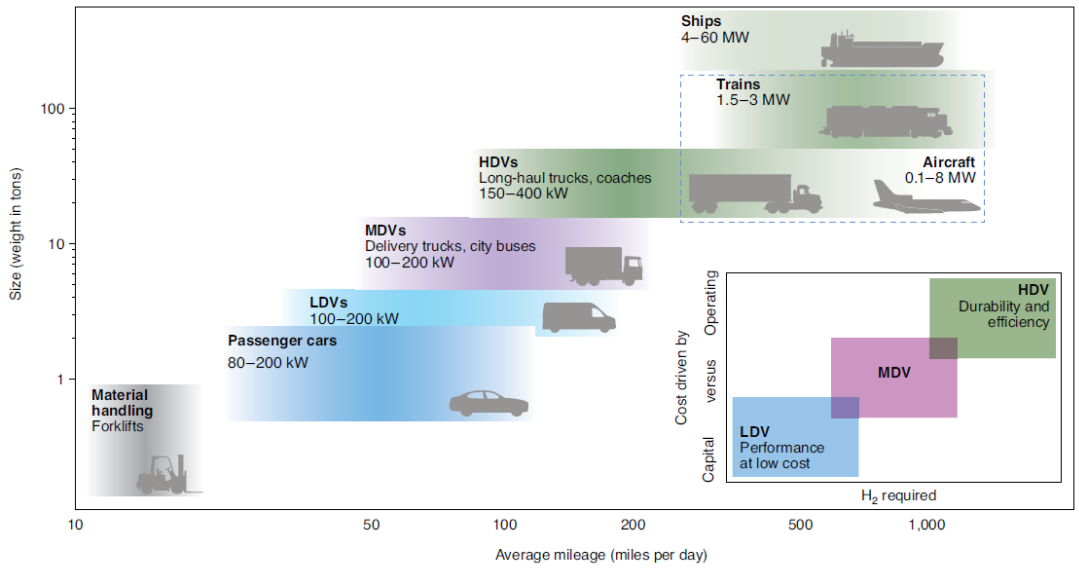

Fig. A-2. Diverses applications des PAC dans le transport [18].

A.1.4 Structure multi-stacks

La littérature aborde fréquemment l'utilisation de systèmes PAC à stack unique de forte puissance dans les groupes motopropulseurs des VHE [23-25]. Cependant, les VL nécessitent souvent des niveaux de puissance dépassant la capacité d'un système PAC à stack unique, ce qui rend l'utilisation de tels systèmes peu pratique. Par conséquent, les chercheurs se tournent de plus en plus vers des systèmes PAC multi-stacks (SPACM) qui utilisent plusieurs FC de faible puissance fonctionnant indépendamment. Les SPACM offrent également de meilleures performances en termes d'efficacité, de fiabilité (disponibilité et durabilité), d'architecture flexible et de réduction globale des coûts par rapport aux systèmes PAC à stack unique [26].

Un SPACM améliore l'efficacité globale du système, en particulier dans les applications à forte puissance où un système FC à stack unique ne peut pas fonctionner en permanence dans sa plage d'efficacité optimale. Contrairement à une PAC à stack unique,

qui ne possède qu'un seul point de fonctionnement idéal, un SPACM permet d'accéder à plusieurs points optimaux. La Fig. A-3 illustre l'impact de l'adoption d'une configuration multi-stacks sur l'efficacité des systèmes PAC. La courbe bleue montre la courbe d'efficacité d'un système FC à stack unique, qui possède un point extrême correspondant à l'efficacité maximale. La courbe rouge représente la courbe d'efficacité d'un système PAC à double stack, permettant un fonctionnement avec deux maxima locaux d'efficacité. Les SPACM offrent une plus grande flexibilité dans la gestion de la puissance, en fournissant plusieurs options de répartition de puissance afin d'atteindre une efficacité plus élevée sous des conditions de charge variables [27].

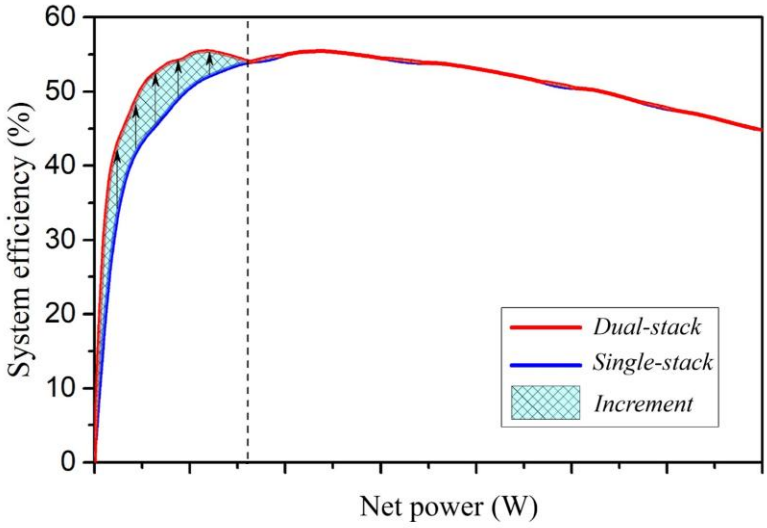

Fig. A-3. Comparaison des efficacités d'un système PAC à stack unique et d'un système PAC à double stack [28].

Un SPACM peut améliorer à la fois la disponibilité et la durabilité en intégrant une fonction de redondance dans le système, ce qui permet d'éviter la dégradation des performances grâce à une flexibilité opérationnelle accrue sans nécessiter d'intervention humaine. Cette redondance réduit le risque de baisse de performance en surveillant en permanence le fonctionnement des modules individuels. En cas de dysfonctionnement, le

MFCS peut fonctionner en mode dégradé, garantissant la continuité du fonctionnement, ce qui n'est pas possible dans les systèmes à source unique. En ce qui concerne la durabilité, un SPACM garantit que les composants tels que les PAC et les batteries fonctionnent dans leurs zones d'efficacité optimales pour répondre aux besoins de puissance. Dans des conditions de faible puissance, seuls quelques modules sont actifs tandis que les autres restent inactifs, ce qui réduit leur dégradation et prolonge la durée de vie globale du système. En cas de panne, le système peut être reconfiguré et les modules défectueux remplacés sans interrompre le fonctionnement. La modularité du système empêche les défaillances en cascade et favorise un fonctionnement continu.

Une architecture flexible constitue un autre avantage important des SPACM, car elle introduit un degré de liberté supplémentaire qui facilite la conception du véhicule. Cette configuration joue un rôle essentiel dans l'amélioration de la stabilité et de la maniabilité du véhicule, lesquelles sont fortement influencées par le centre de gravité du véhicule, lié à sa masse. La stabilité lors des opérations normales et des manœuvres est fortement affectée par la position du centre de gravité dans les directions longitudinale, latérale et verticale. En disposant stratégiquement les composants du groupe motopropulseur, la distribution de masse du véhicule peut être optimisée. Dans les SPACM, l'utilisation de plusieurs modules de faible puissance, plutôt qu'une source unique de forte puissance, permet une distribution plus efficace de la masse, conduisant à une meilleure stabilité du véhicule et à une conduite plus sûre.

Un autre avantage majeur des SPACM réside dans la réalisation d'économies d'échelle et dans la possibilité de production à grande échelle des systèmes de puissance. En ajustant le nombre de modules, les SPACM permettent d'utiliser le même module de base pour une

large gamme de besoins en puissance. Plusieurs modules similaires produits sur une même ligne peuvent être combinés afin de répondre à diverses exigences de puissance, ce qui réduit les coûts moyens à mesure que la production augmente. Bien que le coût initial de conception et de mise en œuvre d'un SPACM soit plus élevé que celui d'un système à source unique, la modularité permet de réduire les dépenses à long terme, car le remplacement d'un module de faible puissance est moins coûteux que celui d'un module de forte puissance.

A.1.5 Stratégie de gestion de l'énergie

Les avantages des SPACM proviennent de l'évolution matérielle du système, qui passe d'une configuration à stack unique à une configuration multi-stacks. Cette transformation introduit plusieurs sources de puissance, notamment des stacks PAC et une batterie, chacune possédant des caractéristiques énergétiques propres. Par conséquent, une stratégie de gestion de l'énergie (SGE) soigneusement conçue devient essentielle. La SGE, qui constitue la composante logicielle du système, joue un rôle crucial dans la gestion de ces sources de puissance. Son objectif principal est de répartir efficacement la puissance afin de satisfaire la demande, tout en minimisant la consommation d'hydrogène, en réduisant la dégradation des sources d'énergie et en optimisant les performances globales du système ou tout autre indicateur clé de performance. Dans la littérature, les SGE sont classées en trois catégories principales : les approches basées sur des règles, les approches basées sur l'optimisation et les approches intelligentes [29].

Les SGE basées sur des règles se distinguent par leur conception simple, leurs faibles exigences computationnelles et leur facilité de mise en œuvre. Cependant, ces stratégies reposent largement sur des règles dérivées de l'expérience, ce qui rend difficile la garantie

d’un contrôle optimal. Par conséquent, la recherche s’oriente de plus en plus vers les SGE basées sur l’optimisation, qui sont plus capables d’atteindre des performances optimales.

Les SGE basées sur l’optimisation consistent généralement à définir une fonction objectif associée à des contraintes, laquelle est ensuite minimisée afin d’améliorer les performances de contrôle [30]. Ces stratégies se divisent en deux grandes catégories: les méthodes en ligne et les méthodes hors ligne. De nombreuses recherches ont été consacrées aux EMS en temps réel et en ligne, explorant différentes approches mettant l’accent sur une optimisation instantanée. Toutefois, ces méthodes ont tendance à optimiser des intervalles de temps individuels, ce qui limite leur champ d’application à un domaine restreint. Cela soulève des questions quant à leur efficacité globale pour atteindre des solutions optimales. La programmation dynamique (PD) et le principe du minimum de Pontryagin constituent des méthodes hors ligne capables de trouver une solution optimale globale.

Les méthodes basées sur l’intelligence utilisent des techniques avancées d’analyse de données afin de dériver des politiques de contrôle optimales en apprenant à partir de données passées et actuelles. Contrairement aux approches traditionnelles, ces méthodes ne reposent pas sur des modèles exacts du système, mais nécessitent la création d’un ensemble de données complet et de taille appropriée, un processus souvent long et complexe. Les techniques appartenant à cette catégorie comprennent l’apprentissage par renforcement, l’entraînement de réseaux neuronaux et divers algorithmes de classification [31].

A.1.6 Dimensionnement des stacks FC et de la batterie, et allocation des stacks

L'obtention des avantages des VHE-PAC en termes de performances et d'efficacité optimales nécessite un dimensionnement précis à la fois de la PAC et de la batterie. La PAC doit être dimensionnée de manière appropriée pour répondre aux besoins de puissance du véhicule tout en minimisant la masse et le coût, tandis que le système de stockage d'énergie doit être dimensionné afin de fournir une capacité énergétique et des capacités de fourniture de puissance adéquates [32]. Un dimensionnement insuffisant peut ne pas satisfaire les exigences de conduite, tandis qu'un dimensionnement excessif peut entraîner une augmentation inutile du coût et de la masse [33]. Par conséquent, un dimensionnement inadéquat peut accroître les coûts du véhicule et rendre potentiellement le VHE-PAC moins attractif pour les consommateurs. Dans les VL, où les exigences de puissance et de durabilité sont particulièrement élevées, la nécessité d'un dimensionnement précis devient encore plus cruciale pour une estimation fiable des coûts. Une estimation efficace des coûts est essentielle pour évaluer la faisabilité économique de ces véhicules [34].

En plus du dimensionnement des composants, le nombre de stacks PAC constitue également un facteur de conception crucial dans les SPACM. Supposons qu'un système PAC doive fournir la puissance nécessaire à une charge. Ce système peut comporter 2, 3, 4 ou davantage de stacks FC. Il est évident que le nombre de stacks influencera à la fois le coût d'investissement initial et le coût d'exploitation du système. Par exemple, l'utilisation d'un plus grand nombre de stacks permet à l'SGE d'activer certaines PAC en fonction de la demande de puissance, ce qui peut potentiellement réduire les taux de dégradation et diminuer la consommation d'hydrogène.

Considérons maintenant que le nombre de stacks soit prédéterminé et égal à N pour fournir une charge P. Si tous les stacks sont identiques, la puissance nominale de chaque stack devrait être P/N. Cependant, si la puissance nominale des stacks PAC peut être différente, de nombreuses configurations permettant de fournir la charge apparaissent. Dans chacune de ces combinaisons, le coût d'investissement du système variera. De plus, étant donné que les caractéristiques des stacks diffèrent dans chaque combinaison, l'efficacité, la dégradation et le coût d'exploitation pour une charge constante varieront également entre les différentes configurations. Il est donc essentiel de reconnaître que le nombre de stacks ainsi que leur puissance nominale choisie jouent un rôle déterminant dans les performances clés lors de la conception d'un SPACM.

A.2 Énoncé du problème et cadre conceptuel

Le problème abordé dans cette thèse couvre deux enjeux principaux : premièrement, l'absence d'une SGE hors ligne de référence, fiable et spécifiquement conçue pour les SPACM, et deuxièmement, le manque de méthodologies intégrées et extensibles permettant d'optimiser simultanément le dimensionnement des composants et la SGE pour des groupes motopropulseurs SPACM couvrant des applications terrestres et aéronautiques, tout en prenant en compte le coût d'investissement, le coût d'exploitation, la durabilité et, dans les contextes aéronautiques, les contraintes de masse de propulsion. Cette recherche contribue à l'état de l'art au travers de trois développements : une SGE hors ligne de référence, extensible, pour SPACM ; une Méthode d'exploration contrainte (MEC) servant de standard de référence calculatoirement abordable ; un cadre intégré de dimensionnement et de gestion de l'énergie, centré sur les VL, appelé Stratégie intégrée de dimensionnement et

de gestion de l'énergie (SIDGE), qui unifie le dimensionnement des composants et le contrôle opérationnel ; et un cadre intégré multiobjectif de dimensionnement et de gestion de l'énergie spécifique aux aéronefs, désigné Stratégie intégrée multiobjectif de dimensionnement et de gestion de l'énergie (SIMDGE), qui optimise à la fois le coût et la masse tout en considérant l'incertitude sur la demande de puissance. La Fig. A-4 résume la portée de cette thèse en liant les applications ciblées au SPACM et aux trois contributions principales: MEC, SIDGE et SIMDGE.

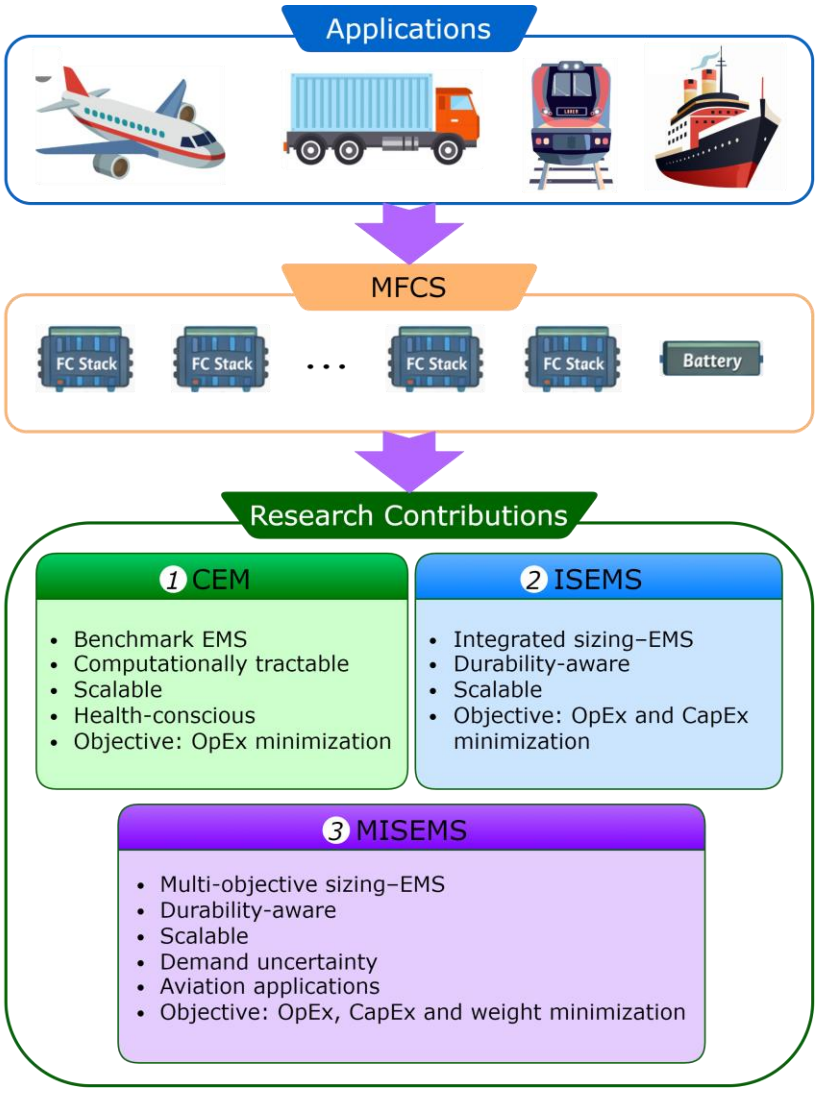

Fig. A-4. Aperçu des applications et des principales contributions de recherche.

A.3 Objectifs et buts

A.3.1 Méthode d'exploration contrainte

Il existe un manque évident de SGE hors ligne pratiques et générales pour les SPACM, qui puissent servir de référence commune pour les stratégies basées sur des règles, en ligne et basées sur l'apprentissage, à travers différents designs multi-stacks. Bien que la PD soit la référence hors ligne par défaut dans les systèmes à stack unique, son application directe aux SPACM devient calculatoirement intractable car la taille de la grille croît de manière exponentielle avec le nombre de stacks et de variables ajoutés, ce qui impose une discrétisation grossière et d'autres simplifications qui réduisent sa valeur comme véritable référence dans les contextes multi-stacks. En pratique, de tels tests PD pour SPACM répartissent souvent la puissance uniformément aux charges légères, déclenchant des commutations fréquentes des stacks PAC. De plus, ce type de PD dans la littérature n'a pas considéré l'état de santé (SOH) des stacks PAC, produisant des schémas d'activation qui surutilisent les stacks plus faibles et gonflent la consommation d'hydrogène et la dégradation.

Pour combler ce manque, il faut des références hors ligne scalables et conscientes de la santé qui conservent une gestion complète des contraintes et un pondération explicite du SOH tout en évitant la malédiction de la dimensionnalité ; la MEC est proposée pour y parvenir en élaguant les régions infaisables ou de faible valeur de l'espace de recherche, restant tractable et produisant encore des schémas d'activation cohérents avec une opération des SPACM consciente de la durabilité. La MEC proposée fournit une nouvelle

référence standard, consciente de la santé, pour les SPACM, réduisant significativement à la fois la charge de calcul et le temps requis pour l'analyse numérique. L'efficacité de la méthode proposée est validée par des tests sur trois VL comme études de cas : un avion, un tramway et un camion.

A.3.2 Stratégie intégrée de dimensionnement et de gestion de l'énergie

Les flux de conception conventionnels pour SPACM séparent le dimensionnement de la SGE ou prédéfinissent la capacité totale PAC avant allocation, ce qui obscurcit les compromis clés entre le nombre de stacks, les puissances nominales hétérogènes et la taille de la batterie, et comment ces choix façonnent le coût d'exploitation, le coût d'investissement et la durabilité en pratique ; la plupart des études intégrées dimensionnement-SGE se concentrent sur les systèmes à stack unique, laissant un manque pour des approches SPACM qui co-optimisent la sélection discrète des stacks, les puissances nominales inégales et la configuration de la batterie ensemble avec une évaluation couplée à la SGE. L'objectif de la SIDGE est de combler ce manque en établissant un cadre intégré, conscient de la dégradation, qui détermine conjointement la modularité des SPACM, les puissances nominales hétérogènes des stacks et le dimensionnement de la batterie tout en évaluant le coût total (incluant les coûts d'investissement et d'exploitation) et les implications en durabilité sous contraintes de mission réalistes, sans fixer à l'avance la capacité totale PAC. Spécifiquement, la SIDGE détermine les tailles des stacks PAC et de la batterie pour minimiser le coût total tout en équilibrant la dégradation ; quantifie comment le nombre de stacks et les puissances nominales inégales influencent le coût total des SPACM ; et clarifie le rôle des limites de SOC de la batterie dans la formation des différents coûts, de sorte que le choix de

modularité, la sélection des puissances nominales des stacks et le dimensionnement de la batterie deviennent des décisions de dimensionnement primaires plutôt que des étapes d'allocation en aval.

A.3.3 Stratégie intégrée multiobjectif de dimensionnement et de gestion de l'énergie

Les aéronefs introduisent des exigences distinctes: beaucoup de travaux antérieurs reposent sur des designs à stack unique, ne co-optimisent pas la masse de propulsion avec le coût et n'intègrent pas le dimensionnement SPACM avec la SGE, laissant les bénéfices potentiels multi-stacks sous-utilisés dans un secteur à haute puissance. De plus, la masse est souvent rapportée plutôt qu'optimisée, et ignorer l'incertitude de mission risque un surdimensionnement ou des manques latents, motivant un design robuste, multiobjectif, avec SGE en boucle pour les SPACM aéronautiques.

Les objectifs de la SIMDGE sont d'établir un cadre pour les SPACM qui cible conjointement les réductions du coût total et de la masse totale de propulsion dans le secteur aéronautique, de prendre explicitement en compte la durabilité via des considérations SOH dans les objectifs de dimensionnement et de SGE, et d'assurer la robustesse des décisions de dimensionnement en considérant l'incertitude sur la demande de puissance de mission. La SIMDGE vise en outre à traiter le nombre de stacks et leurs puissances nominales comme des choix de dimensionnement primaires plutôt que des entrées fixes, permettant d'évaluer comment la modularité et l'hétérogénéité façonnent les compromis coût-masse dans les contextes aéronautiques.

A.4 Méthodologie

La méthodologie utilise un modèle partagé des SPACM comme colonne vertébrale et applique des méthodes adaptées à chaque étude. L'architecture est un SPACM parallèle sur un bus DC commun avec des convertisseurs DC-DC unidirectionnels par stack et un convertisseur ESS bidirectionnel, permettant un contrôle indépendant des stacks, la redondance et la modularité. Le comportement des PACMEP suit un modèle de tension semi-empirique et une relation standard puissance-débit d'hydrogène, tandis que la dégradation est modélisée de manière orientée-contrôle en pénalisant les démarrages-arrêts, les transitoires rapides et les extrêmes soutenus. De plus, la batterie utilise un modèle de résistance interne avec dynamique SOC.

A.4.1 Méthode d'exploration contrainte

À la première étape du projet, une SGE optimale hors ligne pour un VHE-PAC multi-stacks visant à réduire à la fois la consommation de carburant et la dégradation des stacks PAC est introduite. Cette méthode est destinée à servir de référence pour évaluer la performance des SGE en ligne dans des études futures. Pour atteindre cet objectif, une MEC est proposée pour l'allocation de puissance parmi les différentes sources d'énergie/puissance. Les méthodes d'exploration souffrent souvent de processus chronophages et de la malédiction de la dimensionnalité, particulièrement quand le nombre de variables de contrôle et d'état augmente. La MEC aborde ce problème en définissant les commandes de puissance des stacks au temps k comme l'état au temps k+1, ce qui réduit la taille de discrétisation tout en préservant une recherche globale sans approximations grossières. Elle resserre davantage l'espace de recherche en utilisant trois filtres qui

agissent ensemble: un filtre de puissance batterie dérivé de l'équation de bilan de puissance, un filtre de plage SOC qui calcule les SOC atteignables en avant et en arrière sous une égalité de SOC terminal, et un filtre d'interpolation SOC qui remplace les valeurs SOC proches de la grille par un représentant unique pour prévenir les fuites d'interpolation et raccourcir le temps d'exécution. La méthode proposée utilise également une fonction de coût multiobjectif consciente de la santé visant à minimiser les coûts opérationnels, incluant la consommation d'hydrogène et la dégradation PAC, et applique toujours un poids SOH de sorte que les stacks à faible SOH sont pénalisés lors de l'optimisation.

Les tests à travers les cas avion, tram et camion montrent que la MEC supporte une opération fluide des stacks en laissant la batterie amortir les changements rapides, évite d'activer trop de stacks aux charges légères, et reste tractable même quand le nombre de stacks briserait la PD. Ensemble, ces résultats font de la MEC une référence hors ligne scalable pour tester des SGE avancées sur SPACM, comblant le besoin d'une référence viable au fur et à mesure que la modularité croît.

A.4.2 Stratégie intégrée de dimensionnement et de gestion de l'énergie

La SIDGE formule une optimisation mixte-entier intégrée dans laquelle les variables de dimensionnement discrètes sélectionnent les modèles de stacks PAC et la configuration batterie, tandis qu'une boucle interne MPC calcule les coûts opérationnels pour chaque candidat de dimensionnement sous limites SOC, puissance, rampe et conscientes du SOH. L'AG explore les configurations candidates SPACM-batterie en encodant les indices de type par stack et les nombres de cellules batterie en série/parallèle, et la MPC évalue la performance de mission de chaque candidat, fournissant consommation d'hydrogène, dégradation PAC et batterie, et faisabilité des contraintes. La fonction de fitness de l'AG est

un coût total conscient de la dégradation qui scale le coût d'investissement à une base par-mission en utilisant la durée de vie implicite du stack le plus dégradé et ajoute les coûts opérationnels basés sur l'hydrogène monétisé, la dégradation PAC, la dégradation batterie et un terme équivalent hydrogène pour la différence de SOC terminal.

La SIDGE recherche la modularité d'un à plusieurs stacks en utilisant des modèles commerciaux et caractérisés en laboratoire. Les variables de décision incluent les types discrets de stacks PAC, le nombre de cellules batterie en série et parallèle, et la séquence de contrôle SGE déterminée en ligne par la MPC sur un horizon glissant. Les contraintes imposent des bornes SOC, limites de puissance batterie, bornes de puissance stack et limites de taux de rampe stack, tandis que le SOH est utilisé pour pénaliser l'opération de stacks dégradés. La population AG évolue avec des évaluations MPC imbriquées jusqu'à convergence, produisant des designs rentables avec des trajectoires SOH équilibrées. La validation sur un camion longue distance et un banc d'essai laboratoire démontre des réductions significatives du coût total.

Dans la MPC, l'état est le SOC batterie, le contrôle est le vecteur d'ajustement de puissance PAC, et la perturbation est la puissance demandée. Le coût sur l'horizon de prédiction somme l'utilisation d'hydrogène, la dégradation PAC pondérée par SOH et la dégradation batterie, appliquant seulement le premier contrôle à chaque étape.

A.4.3 Stratégie intégrée multiobjectif de dimensionnement et de gestion de l'énergie

La SIMDGE étend le concept de dimensionnement-opération intégré aux aéronefs en considérant deux objectifs : minimiser le coût total du groupe motopropulseur et la masse

totale de propulsion. Le cadre utilise un NSGA-II entier externe pour le dimensionnement et la même SGE basée sur MPC pour l'évaluation opérationnelle. Le vecteur de décision contient les indices discrets de modèles de stacks PAC et les nombres série/parallèle batterie pour un nombre fixe de stacks, et la SGE interne évalue le coût opérationnel et la satisfaction des contraintes pour chaque candidat. Les objectifs combinent le coût total moyenné sur scénarios, qui utilise un scaling conscient de la dégradation de l'investissement plus coût opérationnel, et la masse totale du système, qui somme les masses des stacks, convertisseurs, compresseur, système de refroidissement, batterie et stockage d'hydrogène.

La SIMDGE modélise l'incertitude de demande de puissance avec un pipeline de scénarios : bruit multiplicatif borné segment par segment génère des scénarios, l'APC retient les composantes couvrant la plupart de la variance, et K-means sélectionne un petit ensemble de scénarios représentatifs pour une optimisation tractable. Pour chaque candidat et chaque scénario représentatif, la SGE basée sur MPC calcule le coût opérationnel sous limites SOC, puissance, rampe et SOH, et le NSGA-II agrège ces résultats pour construire des fronts de Pareto robustes. Le résultat est un ensemble de designs SPACM-batterie qui révèlent les compromis coût-masse et démontrent l'impact de la modularité et des sélections de stacks hétérogènes sous incertitude de charge, avec évaluation cohérente de la SGE à travers tous les scénarios.

A.5 Résultats et analyse

Le chapitre 2 a développé une méthode nommée MEC comme référence hors ligne de stratégie de gestion de l'énergie (EMS) pour les véhicules lourds équipés de systèmes à

piles à combustible multi-stacks (SPACM) et d'une batterie. Cette méthode permet d'atteindre l'évolutivité, la prise en compte de l'état de santé des composants et une efficacité temporelle élevée grâce à l'utilisation de filtres guidés par des contraintes sur la puissance de la batterie et les limites de SOC. En intégrant une fonction de coût combinant la consommation d'hydrogène et la dégradation des composants, la MEC a permis d'identifier des stratégies sélectives d'activation des stacks qui préservent leur état de santé tout en satisfaisant la demande de puissance. La méthode demeure également applicable lorsque la densité de discrétisation des variables de contrôle et le nombre de stacks augmentent. Les études de cas ont montré des gains constants. Dans le cas de l'avion NASA X-57, la MEC a réduit le coût d'exploitation de 2 % et le temps de calcul de 10,5 % par rapport à la programmation dynamique (PD) de type level-set avec 20 points de discrétisation, tout en surpassant la programmation quadratique séquentielle (PQS) avec une réduction de coût de 14,6 %. Dans le cas d'un tramway hybride à deux stacks avec 40 points de discrétisation, la MEC a réduit le coût d'exploitation de 1,7 % et le temps de simulation de 90,4 % par rapport à la PD, et a diminué le coût de 16,6 % par rapport à la PQS. Dans le cas d'un camion équipé de quatre stacks de piles à combustible de 75 kW, la MEC a coordonné le fonctionnement des stacks afin d'égaliser les coûts de dégradation et a permis une réduction de 17,1 % du coût d'exploitation par rapport à la PQS, tandis que la PD de type level-set n'a pas pu résoudre le problème de gestion de l'énergie pour un système comportant quatre stacks. Ainsi, le chapitre 2 établit la MEC comme une méthode de référence hors ligne fiable pour le développement des EMS appliqués aux SPACM et comme une base pour la validation future des stratégies de gestion de l'énergie.

Le chapitre 3 a présenté un SIDGE prenant en compte la dégradation pour les SPACM dans les véhicules lourds, étendant l'approche de dimensionnement simultané et de gestion de l'énergie au-delà des systèmes à stack unique grâce à un cadre GA–MPC. Ce cadre permet d'optimiser conjointement la taille des stacks de piles à combustible et la configuration de la batterie tout en évaluant différents nombres de stacks. Contrairement aux études qui prédéfinissent la puissance totale du système de piles à combustible puis en déduisent la taille des stacks individuels, la méthode proposée spécifie directement la puissance nominale de chaque stack et intègre un contrôle prenant en compte la dégradation dans un cadre d'optimisation unique, permettant ainsi d'évaluer simultanément l'architecture et l'exploitation du système. Dans l'étude de cas d'un camion long-courrier, la méthode a permis de réduire le coût total jusqu'à 68 % par rapport aux configurations rapportées dans la littérature, tout en identifiant une conception optimale pour chaque niveau de modularité allant de un à six stacks. La configuration à cinq stacks s'est révélée la plus économique avec un coût total de 79,65 $, comprenant 18,03 $ de coût d'exploitation et 61,62 $ de coût d'investissement normalisé, et a atteint la durée de vie la plus longue d'environ 2209 heures, contre 1514 heures pour un système à stack unique. Dans une deuxième étude de cas utilisant des stacks expérimentaux, la configuration à stack unique s'est révélée irréalisable sous les contraintes de mission. Parmi les configurations réalisables comportant de deux à cinq stacks, la solution avec deux stacks de 2 kW a permis d'obtenir le coût total minimal (3,55 $) ainsi que la durée de vie la plus longue (environ 2984 heures), tandis que la configuration à cinq stacks réduisait la durée de vie à environ 1687 heures en raison d'une dégradation accrue des piles à combustible. L'analyse de sensibilité a montré que l'élargissement de la plage de SOC de [0,50–0,70] à [0,20–1,00] permettait de réduire le coût total jusqu'à 67,4 %, grâce à une utilisation accrue de la

batterie, une dépendance réduite aux piles à combustible et une diminution des événements de commutation accélérant leur dégradation. Dans l'ensemble, la méthode proposée offre une approche évolutive et durable pour la conception et le contrôle rentables des SPACM dans les véhicules lourds.

Le chapitre 4 a étendu le paradigme de co-conception dimensionnement-exploitation aux SPACM orientés vers les applications aéronautiques en proposant une approche SIMDGE. Ce cadre multi-objectif vise à minimiser simultanément le coût total du système et la masse du système de propulsion sous incertitude sur la demande de puissance, tout en intégrant une stratégie de gestion de l'énergie. En utilisant un algorithme NSGA-II basé sur des variables entières couplé à un MPC prenant en compte la dégradation, la méthode optimise conjointement la modularité des piles à combustible, la puissance nominale des stacks et le dimensionnement de la batterie. Dans l'étude de cas de l'avion NASA X-57, la méthode SIMDGE a réduit le coût total de 157,12 $ à 138,64 $ (11,8 %) et la masse du système de propulsion de 855,63 kg à 705,11 kg (17,6 %) par rapport à une configuration de référence à stack unique, démontrant l'avantage quantitatif de l'approche proposée. Les fronts de Pareto obtenus pour des architectures comportant de un à quatre stacks montrent que l'augmentation de la modularité déplace les solutions vers des régions de coût et de masse plus faibles en améliorant le partage de charge et en réduisant la consommation d'hydrogène ainsi que les contraintes sur les composants. Toutefois, les gains de performance deviennent marginaux au-delà d'un niveau intermédiaire de modularité en raison de la masse supplémentaire des convertisseurs et des composants auxiliaires. Le dimensionnement de la batterie apparaît comme un facteur déterminant dans ce compromis: une réduction de la capacité de la batterie diminue la masse du système mais augmente les

sollicitations dynamiques des piles à combustible et les coûts liés à leur dégradation, en particulier pour les solutions minimisant la masse. Dans l'étude de cas expérimentale, les conceptions réalisables présentaient des masses totales comprises entre 38,80 kg et 87,03 kg et des coûts entre 5,81 $ et 28,15 $. La configuration à deux stacks a permis d'obtenir le coût le plus faible, tandis que l'augmentation du nombre de stacks n'apportait pas d'avantage significatif, confirmant l'existence d'un niveau optimal de modularité intermédiaire. Dans l'ensemble, le chapitre 4 démontre que l'identification d'architectures SPACM robustes, économiquement efficaces et légères pour les applications aéronautiques nécessite une co-conception multi-objectif du dimensionnement et de la gestion de l'énergie.